PROPAGATION OF PHOTONS THROUGH OPTICAL FIBER:

SPIN-ORBIT INTERACTION AND NONLINEAR

PHASE MODULATION

by

DASHIELL LAWRENCE PYLE VITULLO

A DISSERTATION

Presented to the Department of Physics
and the Graduate School of the University of Oregon
in partial fulfillment of the requirements
for the degree of
Doctor of Philosophy

September 2016

DISSERTATION APPROVAL PAGE

Student: Dashiell Lawrence Pyle Vitullo

Title: Propagation of Photons through Optical Fiber: Spin-Orbit Interaction and Nonlinear Phase Modulation

This dissertation has been accepted and approved in partial fulfillment of the requirements for the Doctor of Philosophy degree in the Department of Physics by:

Daniel A. Steck	Chair
Michael G. Raymer	Advisor
Steven J. van Enk	Core Member
Andrew H. Marcus	Institutional Representative

and

Scott L. Pratt	Dean of the Graduate School

Original approval signatures are on file with the University of Oregon Graduate School.

Degree awarded September 2016

DISSERTATION ABSTRACT

Dashiell Lawrence Pyle Vitullo

Doctor of Philosophy

Department of Physics

September 2016

Title: Propagation of Photons through Optical Fiber: Spin-Orbit Interaction and Nonlinear Phase Modulation

We investigate two medium-facilitated interactions between properties of light upon propagation through optical fiber. The first is interaction between the spin and intrinsic orbital angular momentum in a linear optical medium. This interaction gives rise to fine structure in the longitudinal momenta of fiber modes and manifests in rotational beating effects. We probe those beating effects experimentally in cutback experiments, where small segments are cut from the output of a fiber to probe the evolution of both output polarization and spatial orientation, and find agreement between theoretical predictions and measured behavior.

The second is nonlinear optical interaction due to cross- and self-phase modulation between the complex-valued temporal amplitude profile of pump pulses and the amplitude profiles of generated signal and idler pulses in optical fiber photon-pair sources utilizing the four-wave mixing process named modulation instability. We develop a model including the effects of these nonlinear phase modulations (NPM) describing the time-domain wave function of the output biphoton in the low-gain regime. Assuming Gaussian temporal amplitude profiles for the pump pulse, we numerically simulate the structure of the biphoton wave function, in symmetric and asymmetric group velocity matching configurations. Comparing the overlap of

the joint temporal amplitudes with and without NPM indicates how good of an approximation neglecting NPM is, and we investigate the effects of NPM on the Schmidt modes. We find that effects of NPM are small on temporally separable sources utilizing symmetric group velocity matching, but appreciably change the state of temporally entangled sources with the same group velocity matching scheme. For sources designed to produce entangled biphotons, our simulations suggest that NPM increases the Schmidt number, which may increase entanglement resource availability with utilization of a phase-sensitive detection scheme. We find that NPM effects on temporally separable sources designed with asymmetric group velocity matching produce non-negligible changes in the state structure. The purity is unaffected at perfect asymmetric group velocity matching, but if the pump is detuned from the correct wavelength, the purity degrades. The largest changes to the state due to NPM occur in long fibers with long pulse durations and low repetition rates.

CURRICULUM VITAE

NAME OF AUTHOR: Dashiell Lawrence Pyle Vitullo

GRADUATE AND UNDERGRADUATE SCHOOLS ATTENDED:

University of Oregon, Eugene, Oregon
Reed College, Portland, Oregon

DEGREES AWARDED:

Doctor of Philosophy (Physics), 2016, University of Oregon
Master of Science (Physics), 2008, University of Oregon
Bachelor of Arts (Physics), 2007, Reed College

AREAS OF SPECIAL INTEREST:

Waveguides, Entangled Light, Quantum Optics

PROFESSIONAL EXPERIENCE:

Science Literacy Program Fellow, University of Oregon, Winter 2016

Graduate Teaching Assistant, University of Oregon, 2014-2016

Graduate Research Assistant, University of Oregon, 2013-2014

GK-12 Teaching Fellow, University of Oregon, 2011-2013

Graduate Research Assistant, University of Oregon, 2008-2011

Graduate Teaching Fellow, University of Oregon, 2007-2008

Research and Development Intern, FEI Company, Summer 2007

Researcher, Qmedtrix Systems, Inc., Summer 2006

Student Researcher, Jisan Research Institute, 2001-2003

GRANTS, AWARDS AND HONORS:

Weiser Senior Teaching Assistant Award, University of Oregon, 2015

PUBLICATIONS:

Dashiell L. P. Vitullo, Cody C. Leary, Patrick Gregg, Roger A. Smith, Dileep V. Reddy, Siddharth Ramachandran, Michael G. Raymer, "Observation of Intrinsic Spin-Orbit Interaction of Light in Few-Mode Optical Fiber," in proceedings *Frontiers in Optics 2016*, paper FW2B.4, (Optical Society of America, Rochester, NY, 2016).

Roger A. Smith, Dileep V. Reddy, Dashiell L. P. Vitullo, and M. G. Raymer, "Double-heralded generation of two-photon-states by spontaneous four-wave-mixing in the presence of noise," Opt. Express **24**, 5809 (2016).

Roger A. Smith, Dileep V. Reddy, Dashiell L. Vitullo, Michael G. Raymer, "Verification of a Heralded, Two-Photon Fock State with a Gang of Detectors," in proceedings of *Frontiers in Optics* 2015, paper FTu3G.2 (Optical Society of America, San Jose, CA, 2015).

M. G. Raymer, Andrew H. Marcus, Julia R. Widom, and Dashiell L. P. Vitullo, "Entangled Photon-Pair Two-Dimensional Fluorescence Spectroscopy (EPP-2DFS)," J. Phys. Chem. B **117** 15559 (2013).

D. L. P. Vitullo, M. G. Raymer, C. C. Leary, and S. Ramachandran, "Photonic Spin-Orbit Interaction in Few-Mode Optical Fiber," in proceedings *Frontiers in Optics 2011/Laser Science XXVII*, paper LWI4, (American Physical Society, San Jose, CA, 2011).

Yoonshik Kang, Kiyoung Cho, Jaewoo Noh, Dashiell L. P. Vitullo, Cody Leary, and M. G. Raymer, "Remote preparation of complex spatial states of single photons and verification by two-photon coincidence experiment," Opt. Express **24**, 5809 (2010).

S. Kazadi, A. Grosz, A. Lim, J. Wigglesworth, and D. Vitullo, "Swarm-Mediated Cluster-Based Construction," Complex Systems **15**, 157 (2004).

ACKNOWLEDGEMENTS

Dedicated to those who work to improve and teach our model of the universe.

May we understand more tomorrow than we do today.

TABLE OF CONTENTS

CHAPTER I

INTRODUCTION

Propagation of light through a medium involves an intricate dance of electric and magnetic fields telling charged matter which way to go, and the motion of that matter makes a polarization response, altering the traveling light. Even in free space, light couples to virtual electron-positron pairs, giving rise to a polarization response from the vacuum. In this sense, the description of light energy going from one place to another is inseparable from matter, which imposes limits on how much power a light beam can contain before rapidly transforming that energy into a jet of particles [1].

The most thorough, quantum mechanical description of light propagation requires corpuscular packets of energy called photons, which are excitations of the electromagnetic field that have a discreteness to them in that they are created and annihilated in quantized units. Classical fields lack this corpuscularity. Furthermore, quantum systems exhibit behaviors that appear "uniquely quantum" and have motivated the development of quantum algorithms that efficiently perform computations which cannot be performed efficiently with any known classical algorithms [2, 3].

Light is an ideal messenger that: interacts weakly with other light, can transmit largely unchanged through transparent materials, travels at the fastest possible speed in free space, and then can be efficiently detected at its destination. Light traveling through a transparent material is absorbed and re-emitted with a different phase, and the superposition of the traveling light with the response light can be described by a refractive index. In these cases, the dipole polarization response of the medium is

proportional to the electric field, and the phenomena described fall into the category "linear optics" [4, 5].

Media can also facilitate light interacting with itself. In this case, the polarization response is approximated by a power series and terms with nonlinear dependence on the electric field make substantial contributions, so phenomena thus described fall into the category of "nonlinear optics." Nonlinear optical interactions can be thought of as multi-photon processes in which the sum of the number of excitations annihilated plus the number of excitations created is greater than two.

1.1 Spin-Orbit Interaction

Photons have four degrees of freedom (DoF): one spin and one for each spatial dimension in 3D space. A paraxial beam of light has a momentum distribution that does not deviate substantially from the beam axis, which we take to be the z-axis. For photons in a paraxial beam, these degrees of freedom are: spin angular momentum (SAM), frequency, radial transverse momentum, and orbital angular momentum (OAM). In classical mechanics, orbital angular momentum is the cross product of position and momentum $\vec{L} = \vec{r} \times \vec{p}$ while spin angular momentum is related to rotation of an object around its center of mass $\vec{S} = I\vec{\omega}$. In quantum mechanics, spin is best understood as a quantized intrinsic property that satisfies the commutation relations between operators $\left[\hat{S}_i, \hat{S}_j\right] = i\hbar\epsilon_{ijk}\hat{S}_k$,[1] and is deeply related to the bosonic or fermionic nature of a quantum particle [6]. Orbital angular momentum for a quantum particle shares the same definition as given for classical mechanics with position $\hat{r}$ and momentum $\hat{p}$ promoted to operators [7]. While it has long been known that light carries angular momentum [8], Leslie Allen's work in 1992 showing that

---

[1]Where ϵ_{ijk} is the Levi-Civita symbol and there is implied summation over repeated indices.

2

photons carry quantized orbital angular momentum ($\ell\hbar$ per photon, with integer ℓ) sparked substantial recent interest [9, 10].

While a light wave's spin is always intrinsic (origin-independent), its orbital angular momentum can be either extrinsic (EOAM), *i.e.* due to the path the light follows, or intrinsic (IOAM), *i.e.* independent of the path the light takes [11, 12]. Thus interaction between spin and orbital angular momentum can be divided into spin-IOAM interaction and spin-EOAM interaction, and both can occur in the same system. In 1972, Kapany and Burke pointed out that the so-called "hybrid" eigenmodes (referred to as EH and HE modes) of a cylindrically symmetric optical waveguide carry quantized orbital angular momentum and that the HE and EH modes are differentiated by the sign of their splitting due to interaction between spin and orbital angular momentum [13]. That is to say, HE modes have IOAM and SAM z-component vectors pointing in the same direction, which is called a parallel combination and results in a spin-IOAM splitting with a minus sign, and EH modes have IOAM and SAM z-component vectors pointing in opposite directions, which is called an anti-parallel combination and results in a spin-IOAM splitting with a plus sign. For electrons, coupling between spin and IOAM is widely known to give rise to atomic energy level splittings (Russell-Saunders coupling), and the same interaction creates a fine structure for modal propagation constants in waveguides [13, 14]. In the atomic case, the splitting can be thought of as due to an effective magnetic field that electrons experience from their motion relative to a nucleus. In the waveguide case, interaction between light's SAM and IOAM is facilitated by the inhomogeneity of the medium.

Tomita and Chiao explained the rotation of optical linear polarization they observed in a single-mode fiber wrapped around a cylinder in a helical path as being

due to a geometric (Berry's) phase [15]. Dooghin *et al.* demonstrated that the same effect can be explained with the spin-orbit interaction (SOI) investigated by Rytov and Vladimirskii [16], sparking interest in the connection between SOI and Berry's phase [17–19]. An excellent review by Bliokh *et al.* presents geometric phases as a unifying description underlying spin-orbit interactions [20], but does not include a construction of spin-orbit splitting for fiber modes.

Experimental investigation of optical SOI has focused on coupling EOAM to spin [15, 16, 21, 22]. The case of the highly multimode fiber investigated by Dooghin *et al.* with a rotating speckle pattern was described with both a ray and wave picture [23], and is analogous to the case of the large glass cylinder investigated by Bliokh *et al.* [22] but excited with a broader angular distribution. Abdulkareem *et al.* recently investigated the effects of EOAM coupling in highly multimode fiber with light traveling in a helical path in a fiber traveling in a helical path [24]. Our work utilizes few-mode fiber where the width of the waveguide is a small multiple of the wavelength of the guided light, and a wave picture is preferable to the ray trajectory approach used in larger waveguides. Investigation of the (IOAM=1)^2 case was undertaken in this regime by Butkovskaya *et al.* [25], though they only give data for a single length. The IOAM=1 case for light has uniquely complicated dynamics and is not representative for other IOAM values. A spectroscopic approach utilizing fiber Bragg gratings to characterize fiber modes spectroscopically does not reveal propagation dynamics, but is a complimentary method for measuring the magnitude of SOI splittings [26].

---

[2]IOAM can be positive or negative, *i.e.* aligned with or against the direction of propagation, but when we refer to specific values, *e.g.* IOAM=2, we are referring to the absolute value of the IOAM.

1.2 Quantum Light Generation

Quantum measurements are nondeterministic. For a particular measurement with multiple possible outcomes, even with perfect information about the initial conditions, outcome cannot be predicted with certainty. A quantum source is characterized by the statistics of the outcomes of measurements performed on the system. Assuming a pure state, the system is described by its quantum state with ket $|\psi\rangle$ (and dual bra $\langle\psi|$). A *quantum measurement* is described by a set of measurement operators $\{\Lambda_m\}$ indexed by possible outcomes m [2]. Let $\Lambda_m = |m\rangle\langle m|$ be a projective measurement. Probabilities of particular measurement outcomes are found using the Born rule $p(m) = \langle\psi|\Lambda_m|\psi\rangle = |\langle m|\psi\rangle|^2$. The interpretation of this mathematical statement, which translates it into a statement of physics, is that the complex-valued wave function, for example $\psi(p) = \langle p|\psi\rangle$ for the wave function in momentum (p) space, gives amplitudes that describe the chances of measuring outcomes and the relationships (phases) between those outcomes while the modulus square of the wave function describes real-valued probabilities of particular measurement outcomes. The sum of the probabilities of all possible outcomes must be one.

Experimental investigation of quantum mechanics requires sources that repeatably prepare quantum particles in appropriate states. Nonlinear optical interactions between a definite number of photons serve well in this capacity. The input photons provide energy and momentum that are conserved (or not) depending on the symmetry properties of the source system under translation in time (energy) and space (momentum). In systems with perfect energy conservation and "good" momentum conservation, *i.e.* the momentum kick to or from the nonlinear medium is small compared to the momentum of the photons, there can be many ways to divvy up the energy and momentum to satisfy conservation. *That* energy is conserved is

set, but *how* energy is conserved, *i.e.* the particular distribution of energy amongst the outputs from the process, is **not set**. This allows for creation of an *entangled* state. To properly define entanglement, we need to generalize to a description of the state in terms of the density operator ρ, which can describe mixed states, is Hermitian $\rho^\dagger = \rho$, has trace $\text{Tr}(\rho) = 1$, and is positive semidefinite $\rho \geq 0$. An entangled state cannot be written as a tensor product of two subsystems, labeled with A and B

$$\rho_{\text{entangled}} \neq \sum_j p_j \rho_j^A \otimes \rho_j^B. \tag{1.1}$$

States that can be written as products are called *separable* states.

Design and control of the properties of the nonlinear medium and the input light allows tailoring of the state describing the output. Nonlinear optics offers an avenue for generating light with a tailored wave function.

The three-wave mixing process of *spontaneous parametric down conversion* has served as the standard photon source process for decades [27]. It takes place in crystals with a non-centrosymmetric unit cell, and divides the energy and momentum of one pump photon into two product photons. Four-wave mixing sources tend to have lower material nonlinearity, and thus require more power to attain the same rate of creation events, but offer the advantages of more freedom in process design, *e.g.* frequency translation devices with a broader range of translation-distance settings [28], and can utilize convenient optical systems like optical fibers, which allow for long interaction lengths in a compact space [29, 30]. However, put colloquially, "having more knobs you *can* adjust means having more knobs you *must* control." Undesired processes that cannot be separated from the process of interest can cause complications in four-wave mixing devices, as we discuss in Chapter VI.

1.3 Questions Addressed

This dissertation addresses questions regarding how light changes while traveling through an optical fiber. Encoding information in spatial patterns transmitted through optical fibers is a frontier of fiber communications. Utilizing modes of higher order than the fundamental modes introduces challenges of coupling between modes intended for use and non-trivial propagation dynamics. These challenges apply to the transmission of both classical and quantum information.

We investigate the propagation of optical-fiber spatial modes carrying intrinsic orbital angular momentum, focusing on single-core fibers and targeting a single-input mapped to single-output scheme, (in contrast to multiple-input and multiple-output (MIMO) schemes). Cody Leary developed a theoretical description of expected effects due to interaction between spin and intrinsic orbital angular momentum for both photons in optical fiber and electrons traveling through analogous cylindrical waveguides [14, 31, 32]. We carry out experimental tests of that theoretical framework in optical fibers to address the following questions:

Does spin-orbit interaction alone determine the evolution of the shape and polarization of light traveling through a fiber, or do other effects play an important role? How well does a spin-orbit interaction model of evolution match observed behavior? How well can we achieve excitation of a desired combination of modes such that the same combination of modes (with phase shifts) exits the fiber output without exciting undesired modes? We find that interaction between spin and intrinsic orbital angular momentum well describes observed behavior in a short fiber (~ 1 m) following a straight path, even in the presence of weak undesired coupling between modes.

We also investigate the nonlinear optical effects of self-phase modulation and cross-phase modulation on photon-pair sources utilizing birefringent optical fibers, focusing on fibers designed for single spatial profile operation at the pump wavelength. Working in the low-gain regime, it is a good approximation to consider the vacuum (which does not lead to detection events) and single photon-pair creation events only. In this regime, we develop a theoretical model that includes the effects of the aforementioned nonlinear phase modulations on the output time-domain photon-pair wave function. Assuming pump pulses with Gaussian temporal distributions, we numerically investigate example systems designed to produce photon-pair wave functions that are: separable through asymmetric group-velocity matching, approximately separable through symmetric group-velocity matching, or entangled with symmetric group-velocity matching.

We find that effects of self- and cross-phase modulation are small on sources that are approximately separable due to symmetric group-velocity matching, but appreciably change the wave function of temporally entangled sources under the same group-velocity matching scheme. For sources designed to produce entangled photon pairs, our simulations suggest that NPM increases the Schmidt number, which may increase entanglement resource availability with utilization of a phase-sensitive detection scheme. We find that NPM effects on temporally separable sources designed with asymmetric group-velocity matching produce non-negligible changes in the state structure. The purity is unaffected at perfect asymmetric group-velocity matching, but if the pump is detuned from the correct wavelength, the purity degrades. The largest changes to the wave function due to NPM occur in long fibers with long pulse durations and low repetition rates.

1.4 Outline

This dissertation is organized as follows: Chapter II reviews background theory of spatial modes in free space, and both exact (vector) and approximate (scalar) bound mode solutions in optical fibers. Perturbative corrections to the propagation constants (phase velocities) of scalar modes, which account for interaction between spin and orbital angular momentum, are discussed. Theoretical predictions of the behavior expected for combinations of modes with different corrections suggest a method for measuring spin-orbit corrections.

Chapter III details a "toy" simulation of our experiments that explores basic examples to get a sense of the physics of spatial pattern and polarization evolution with propagation. Excitation of undesired modes at the fiber input and constant unitary defect-driven mode coupling are investigated numerically. Chapter IV discusses the design and operation of equipment used in Chapter V, where experimental procedures and results are discussed and compared to theory.

Chapter VI details simulation of the effects of nonlinear phase modulation on photon-pair creation via the modulation instability process in optical fibers, and discusses the effects on heralded state purity and Schmidt mode populations in the output signal photon state. We consider the circumstances in which nonlinear phase modulation degrades purity or effects the population and structure of signal Schmidt modes.

CHAPTER II

SPATIAL MODES

2.1 Spatial Modes in Free Space

Maxwell's equations in free space combine to give the 3D electromagnetic wave equations [33, 34]

$$\left(\nabla^2 - \frac{1}{c^2} \frac{\partial^2}{\partial t^2} \right) \vec{E}(\vec{r}, t) = 0 \qquad (2.1)$$

$$\left(\nabla^2 - \frac{1}{c^2} \frac{\partial^2}{\partial t^2} \right) \vec{H}(\vec{r}, t) = 0 \qquad (2.2)$$

where ∇^2 is the Laplacian, c is the speed of light in vacuum, $\vec{r}$ is position, t is time, $\vec{E}(\vec{r}, t)$ is the electric field, and $\vec{H}(\vec{r}, t)$ is the magnetic field. We use complex-valued field descriptions and linear optics from here through Chapter V, with the understanding that the physical field is the real part of the complex-valued field.

The starting point for thinking about the propagation of light through free space is a monochromatic plane wave

$$\vec{E}(\vec{r}, t) = A \exp \left[i \left(\vec{k} \cdot \vec{r} - \omega t \right) \right] \hat{e} \qquad (2.3)$$

where A is the amplitude, $\vec{k}$ is the propagation vector with magnitude k, ω is the angular frequency, and $\hat{e}$ is the polarization unit vector. Ideal plane waves have infinite extent, and though they cannot be produced in a laboratory setting they are the building blocks for all practically realizable beams through superposition.

Solutions to the wave equation constitute sets of *modes*, which are self-consistent field distributions that are orthonormal under the inner product

$$\int \mathrm{d}\vec{r}\, \vec{E}_i(\vec{r}) \cdot \vec{E}_j^*(\vec{r}) = \delta_{ij} \tag{2.4}$$

where δ_{ij} is a Kronecker delta and $*$ denotes complex conjugation. In free space, modes may scale (change size) as they proceed through space, but do not change shape. In media, symmetry and boundary conditions must be satisfied. In an optical fiber with invariant structure along the axis of propagation, modes do not scale with propagation through the fiber.

2.1.1 Gaussian Beams

Following Siegman, we separate the electric field parameterized in Cartesian coordinates $E(x, y, z) = u(x, y, z) \exp(-ikz)$ into the quickly varying propagation factor $\exp(-ikz)$ and the slowly varying envelope $u(x, y, z)$ [35]. A Gaussian beam is represented by

$$u(x, y, z) = \frac{1}{\tilde{q}(z)} \exp\left[-ik\frac{x^2 + y^2}{2\tilde{q}(z)}\right] \tag{2.5}$$

where $\tilde{q}$ is the complex Gaussian beam parameter with information about the curvature of the beam, $R(z)$, and the width of the beam, $w(z)$ as a function of z. Specifically,

$$\frac{1}{\tilde{q}(z)} = \frac{1}{R(z)} - i\frac{\lambda}{\pi w^2(z)}, \tag{2.6}$$

where λ is the wavelength in the medium in which the beam is propagating. The beam waist w_0 is the minimum beam radius in the plane $z = 0$. Propagation of a

11

beam through free space follows

$$\tilde{q}(z) = \tilde{q}_0 + z = z + iz_R \qquad (2.7)$$

where $z_R = \pi w_0^2 / \lambda$ is the Rayleigh range and $\tilde{q}_0 = \tilde{q}(0) = iz_R$. The Rayleigh range is the distance in z away from the waist at $z = 0$ where the beam width increases from w_0 to $\sqrt{2}w_0$, and approximately demarcates the near-field region from the far-field region. The confocal parameter, $b = 2z_R$ is the longitudinal range outside of which the beam diverges substantially.

The evolution along z of the beam's width, wavefront radius of curvature, and Gouy phase, $G(z)$ are, respectively,

$$w(z) = w_0 \sqrt{1 + \left(\frac{z}{z_R}\right)^2} \qquad (2.8)$$

$$R(z) = z + \frac{z_R^2}{z} \qquad (2.9)$$

$$G(z) = \tan^{-1}\left(\frac{z}{z_R}\right). \qquad (2.10)$$

The beam parameter is introduced for Gaussian beams, but also applies in describing the behavior of higher-order Hermite-Gauss and Laguerre-Gauss modes.

2.1.2 Hermite-Gauss Modes

The Hermite-Gaussian (HG) transverse mode basis described with coordinates (x,y,z) contains modes with Cartesian symmetry, *i.e.* they are even or odd under the inversions $x \to -x$ and $y \to -y$. One example system that creates HG modes is a laser cavity containing two crossed wires, one oriented along the horizontal direction

12

and the other oriented along the vertical direction. We use laser systems with crossed-wire configurations for this purpose in our experiments (described in Chapter V).

HG spatial modes are described by [36]

$$C_{n,m}^{\mathrm{HG}} = \left(\frac{2}{\pi n! m!} \right)^{1/2} 2^{-(n+m)/2} \tag{2.11}$$

$$\mathrm{HG}_{n,m}(x,y,z) = C_{n,m}^{\mathrm{HG}} \frac{1}{w(z)} H_n \left(\frac{\sqrt{2}x}{w(z)} \right) H_m \left(\frac{\sqrt{2}y}{w(z)} \right) \exp \left[-\frac{x^2 + y^2}{w^2(z)} \right]$$

$$\times \exp \left[-i \left(k \frac{r^2}{2R(z)} + (n+m+1)G(z) \right) \right] \tag{2.12}$$

where H_n and H_m are Hermite polynomials.

2.1.3 Laguerre-Gauss Modes

While light always has spin angular momentum (SAM), only some light beams carry orbital angular momentum (OAM). Allen *et al.* showed that Laguerre-Gaussian laser modes carry quantized units of $\ell\hbar$ per photon [9].

As explained by O'Neil *et al.* [11] (following up on the clear description by Berry [37]), orbital angular momentum can be separated into *extrinsic* (EOAM), which is dependent on the choice of rotation axis, and *intrinsic* (IOAM), which is independent of axis choice. Consider a light beam with average momentum $\langle \vec{p} \rangle = (p_x, p_y, p_z)$ and choose a rotation axis oriented in the z-direction. The average orbital angular momentum in the z direction is $\langle L_z \rangle = \langle (\vec{r} \times \vec{p}) \cdot \hat{z} \rangle$. Displacing the rotation axis laterally by some distance $\vec{r}_0 = (r_{0x}, r_{0y})$ changes L_z by $\Delta L_z = r_{0x} p_y - r_{0y} p_x$. If the transverse momentum is zero, *i.e.* $p_x = p_y = 0$, then $\Delta L_z = 0$ and the OAM is intrinsic. Or, as O'Neil *et al.* write

Any beam with a helical phase front apertured symmetrically about the beam axis has zero transverse momentum and, consequently, an orbital angular momentum of $\ell\hbar$ per photon, independent of the axis of calculation. The orbital angular momentum of the light beam may therefore be described as intrinsic.

Laguerre-Gaussian modes are eigenmodes of IOAM, and are described in cylindrical coordinates (r, ϕ, z) by

$$C_{n,m}^{\mathrm{LG}} = \left(\frac{2}{\pi n! m!} \right)^{1/2} \min(n, m)! \tag{2.13}$$

$$\mathrm{LG}_{n,m}(x, y, z) = C_{n,m}^{\mathrm{LG}}(1/w) L_{\min(n,m)}^{|n-m|}(2r^2/w^2) \exp\left[-\frac{r^2}{w^2(z)} \right]$$

$$\times \exp\left[-i \left(k \frac{x^2 + y^2}{2R(z)} + (n + m + 1)G(z) + (n - m)\phi \right) \right] \tag{2.14}$$

Relating the coordinate systems by the standard $r = \sqrt{x^2 + y^2}$ and $\phi = \tan^{-1}(y/x)$, LG and HG modes are related by

$$b(n, m, k) = \sqrt{\frac{(m + n - k)! k!}{2^{n+m} n! m!}} \frac{1}{k!} \frac{\mathrm{d}^k}{\mathrm{d}t^k} [(1 - t)^n (1 + t)^m]|_{t=0} \tag{2.15}$$

$$\mathrm{LG}_{n,m}(x, y, z) = \sum_{k=0}^{n+m} i^k b(n, m, k) \, \mathrm{HG}_{n+m-k,k}(x, y, z) \tag{2.16}$$

Thus, combinations of LG modes carrying IOAM can combine to make HG modes with no IOAM and vice versa. Control of the phase between these modes is important for these transformations, and Beijersbergen *et al.* designed an optical astigmatic mode converter device that utilizes the Gouy phase and astigmatic focusing to introduce the correct phase shifts to convert between HG and LG modes [36].

14

2.2 Guided Modes In Optical Fiber

Optical fibers guide light from their inputs to their outputs. Diffraction is counteracted by a confinement mechanism that reflects light rays and prevents them from exiting the fiber core [38]. Another picture is excitation of bound modes that propagate all the way to the fiber output, as they are ideally lossless and uncoupled to radiation modes that "leak" light out of the fiber [39, 40]. For an object to act as a waveguide, it must have an inhomogeneous refractive index structure.

The conceptually simplest design is a step-index fiber (see Fig. 2.1) with a core that has radius a, and refractive index n_{co}, which is greater than the refractive index of the surrounding cladding n_{cl}. A ray of light shone into the fiber such that it strikes the interface between the core and cladding at an angle to the surface normal, α that is greater than the critical angle, $\alpha_c = \sin^{-1}(n_{cl}/n_{co})$, will undergo total internal reflection at that intersection, and all subsequent intersections with the interface, provided the bend radius of the fiber path never brings α below α_c [41]. Many real fibers are coated with a jacket that protects the fiber and absorbs light lost from the core, but the jacket is at a radius much greater than modal extent, so the fiber cladding can be taken to have infinite cross-sectional extent in modal calculations. When a is comparable to the wavelength of the light λ, it is preferable to use a modal wave picture.

Fiber coupling is directional, in the sense that the angular distribution of light radiated from each point on a source limits the achievable coupling efficiency. A *diffuse source*, *e.g.* a lightbulb filament, emits light in all directions from each point on the source. Lenses cannot improve the coupling efficiency of a diffuse source above the coupling efficiency achieved by placing the source against the fiber input face [41, Section 4-14]. A *directional source*, *e.g.* a laser beam with a narrow angular

15

distribution at each point in its output plane, can be matched into the fiber mode area with a lens system for efficient coupling. Lasers with direction of emission sharply peaked about the beam axis are a natural choice of source for exciting optical fiber modes.

We assume that fibers are invariant in the longitudinal direction, z. Fiber modes experience a refractive index n_{eff} bounded by $n_{\text{co}} > n_{\text{eff}} > n_{\text{cl}}$. The phase velocity a mode experiences is $\nu = c/n_{\text{eff}}$ where c is the speed of light in vacuum.
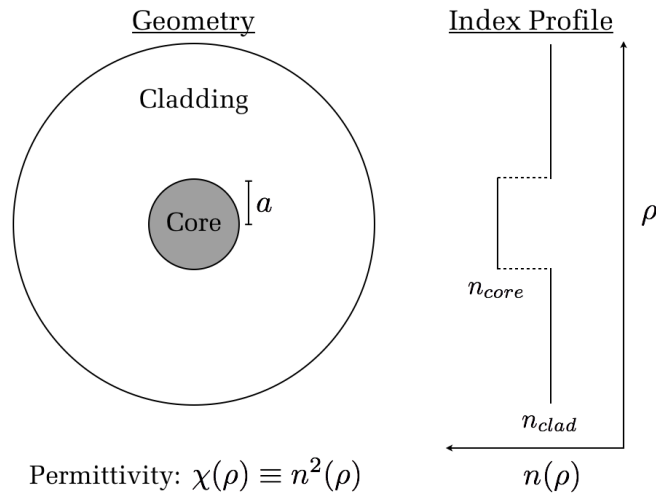
FIGURE 2.1. Geometry and index profile for a step-index fiber.

Bound fiber modes have characteristic wavenumber $n_{\text{co}}k = n_{\text{co}}2\pi/\lambda$, with longitudinal component, β, and transverse component of length κ, illustrated in Fig. 2.2 [38]. The effective index can be expressed as $n_{\text{eff}} = \beta/k$ and is also simply related to a characteristic angle $\theta_c = \cos^{-1}(n_{\text{eff}}) = \cos^{-1}\left(\frac{\beta}{n_{\text{co}}k}\right)$, which is **not to be confused** with the critical angle α_c, (often denoted θ_c in other work). It is helpful to

16
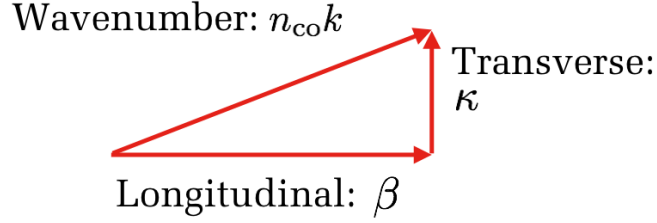
FIGURE 2.2. In-fiber wavevector decomposition into transverse and longitudinal parts and their associated lengths.

define positive and dimensionless modal parameters

$$U = \sqrt{a^2(k^2 n_{\text{co}}^2 - \beta^2)} = ka\sqrt{n_{\text{co}}^2 - n_{\text{eff}}^2} \qquad (2.17)$$

$$W = \sqrt{a^2(\beta^2 - k^2 n_{\text{cl}}^2)} = ka\sqrt{n_{\text{eff}}^2 - n_{\text{cl}}^2}. \qquad (2.18)$$

The modal parameters combine to make the *waveguide parameter* or normalized frequency

$$V = \sqrt{U^2 + W^2} = ka\sqrt{n_{\text{co}}^2 - n_{\text{cl}}^2}. \qquad (2.19)$$

For a particular wavelength and fiber parameters, V determines the number of bound fiber modes. When $V \approx 2.405$, or less, only the fundamental spatial distribution is guided and will propagate long distances. Fibers in this regime are often referred to as "single-mode fibers" even though the number of modes guided is wavelength dependent, and there are two polarization modes for the fundamental. There is only one spatial shape guided through a fiber in single-mode operation, so, in that sense, the name is justified.[1] Leaving the design wavelength range may result in multimode operation. When V is above this cutoff, multiple spatial modes are bound (guided)

---

[1]It is also common for the term "mode" to be used loosely when "spatial profile" or "approximate mode" is understood to be the intended meaning.

over long wavelengths. Fibers referred to as "multimode" are often well above this limit. Between single-mode and multimode operation, few-mode fibers will only guide a small number of shapes. For $V \gg 1$, the number of bound waveguide modes can be approximated by $N_{\mathrm{bm}} \approx V^2/2$ [41, Eqn. 36-41].

In the next sections, we explore exact (vector) and approximate (scalar) wave equation solutions for optical fiber modes. Parameters that approximate a Thorlabs SM2000 fiber excited by a HeNe laser, are shown in Table 2.1, and used to generate solutions in both sections.

TABLE 2.1 Fiber parameters reverse engineered for a Thorlabs SM2000 fiber and used to generate exact mode solutions Sec. 2.3 and scalar mode solutions in Sec. 2.4.

Description	Property	Value
Core Radius	a	$5.5\,\mu\mathrm{m}$
Wavelength	λ	$632.8\,\mathrm{nm}$
Cladding Index	n_{cl}	1.4570121246
Core Index	n_{co}	1.4527438681
V-Parameter	V	6.08597

To maximize the bandwidth available for fiber communication is to maximize the number of independent communication channels. Frequency and polarization control techniques are well developed for optical fibers. Wavelength division multiplexing is widely deployed technology[2] that, in part, owes its robust performance to linear optics where the frequency at the output is the same as the frequency at the input. The remaining two degrees of freedom for adding more independent channels are spatial, so there is great interest in mode-division multiplexing [42–46]. However, unavoidable perturbations to fiber index profiles drive energy coupling between fiber modes, compromising the independence of the modes. This coupling is depend on

---

[2]That probably played a part in you, dear reader, obtaining this dissertation.

how well the modes are separated in β [47]. In Sec. 2.4, we discuss what is commonly referred to as the weak guidance approximation, but is better known as the low contrast approximation (as the modes are still strongly guided), which neglects spin-orbit interactions with the assumption that $n_{\text{co}} \approx n_{\text{cl}}$. Since $n_{\text{co}} > n_{\text{eff}} > n_{\text{cl}}$ and $n_{\text{eff}} = \beta/k$, fiber systems well described in this approximation will have a small range of β values over which to separate their modes. Thus, it is desirable for mode-division multiplexing to utilize fiber systems with larger differences in $n_{\text{co}} - n_{\text{cl}}$ for a large available β space, and in this regime spin-orbit effects will be larger than in low contrast systems.

2.3 Exact Modes

Light guided in a fiber with a z-invariant index profile can be represented as superpositions of fields written in a separable form as *modes*

$$\vec{E} = \vec{e} \exp(i\beta z) \tag{2.20}$$

$$\vec{H} = \vec{h} \exp(i\beta z) \tag{2.21}$$

where the characteristic longitudinal ($\hat{z}$) propagation constant of a mode is β. Modes satisfy the modal vector wave equations for the complex electric ($\vec{E}$) and magnetic ($\vec{H}$) fields [48]:

$$\left(\nabla_{\text{t}}^{2} + k^{2}n^{2} - \beta^{2}\right)\vec{e} = -\left(\nabla_{\text{t}} + i\beta\hat{z}\right)\vec{e}_{\text{t}} \cdot \nabla_{\text{t}} \ln\left[n^{2}\right] \tag{2.22}$$

$$\left(\nabla_{\text{t}}^{2} + k^{2}n^{2} - \beta^{2}\right)\vec{h} = \left[\left(\nabla_{\text{t}} + i\beta\hat{z}\right) \times \vec{h}\right] \times \nabla_{\text{t}} \ln\left[n^{2}\right] \tag{2.23}$$

where ∇_{t} is the transverse gradient and the t subscript generally indicates the transverse components, k is the vacuum wavenumber, and n is the local refractive

19

index. In cylindrical symmetry, the solutions within regions of uniform index take the form of Bessel functions and modified Bessel functions of the first and second kind, all indexed by an integer $\nu \geq 0$.

Imposing proper boundary conditions on the fields at the interface results in a characteristic equation with a discrete set of solutions. For a cylindrically symmetric single-step-index fiber the characteristic equation is

$$(\nu n_{\text{eff}})^2 \left(\frac{V}{UW}\right)^4 = \left(\frac{n_{\text{co}}^2 J_\nu'(U)}{U J_\nu(U)} + \frac{n_{\text{cl}}^2 K_\nu'(W)}{W K_\nu(W)}\right) \left(\frac{J_\nu'(U)}{U J_\nu(U)} + \frac{K_\nu'(W)}{W K_\nu(W)}\right) \quad (2.24)$$

where J is a Bessel J function (Bessel function of the first kind), K is a Bessel K function (Bessel function of the second kind), and the prime indicates the derivative of the function with respect to its argument (U or W). Solving this transcendental characteristic equation for eigenvalue U, (or equivalently, n_{eff}, W, or β; as they are all related), can be accomplished numerically.

Exact mode solutions are organized into four classes, the transverse electric (TE), transverse magnetic (TM), and two so-called "hybrid" modes referred to as HE and EH modes. TE and TM modes are solutions for which the longitudinal component of either the electric, E_z, or magnetic, H_z field is zero. There are no solutions with both longitudinal components zero in fiber. TE and TM modes are solutions for $\nu = 0$. The EH and HE modes are solutions for $\nu \neq 0$, in which case we can use the definitions $x = \frac{J_\nu'(U)}{U J_\nu(U)}$, $C = (\nu n_{\text{eff}})^2 \left(\frac{V}{UW}\right)^4$, $b = \frac{K_\nu'(W)}{W K_\nu(W)}$, and $\frac{n_{\text{cl}}^2}{n_{\text{co}}^2} = 1 - 2\Delta$ and rewrite the characteristic equation as a second degree equation in x with real roots

$$x = -b(1 - \Delta) \pm \sqrt{b^2\Delta^2 + C/n_{\text{co}}^2} \quad (2.25)$$

The plus sign corresponds to EH modes while the minus sign corresponds to HE modes. The EH modes have anti-parallel combinations of OAM and SAM, while the HE modes have parallel combinations, as discussed further in section 2.6 [13].

The characteristic equations for the TE and TM modes with $\nu = 0$ simplify to

$$\text{(TE)} \qquad \frac{J_1(U)}{U J_0(U)} = -\frac{K_1(W)}{W K_0(W)} \qquad \qquad (2.26)$$

$$\text{(TM)} \qquad \frac{n_{co}^2 J_1(U)}{U J_0(U)} = -\frac{n_{cl}^2 K_1(W)}{W K_0(W)}, \qquad \qquad (2.27)$$

and the graphs of the dimensionless left-hand sides and right-hand sides for both equations are shown in Fig. 2.3. Solutions to the characteristic equations are indexed by $M_{\nu,m}$ where M is the mode class designation $M \in \{\text{TE}, \text{TM}, \text{HE}, \text{EH}\}$, and m is the radial mode index. The TE and TM mode solutions with the smallest U values correspond to $m = 1$, the solutions with the next largest U correspond to $m = 2$, and so on. Thus, Fig. 2.3 shows that there are two TE modes ($\text{TE}_{0,1}$ and $\text{TE}_{0,2}$) and two TM modes, ($\text{TM}_{0,1}$ and $\text{TM}_{0,2}$), bound in this fiber configuration, while higher-order radial modes are cut off. U values for all mode classes are given in Table 2.3.
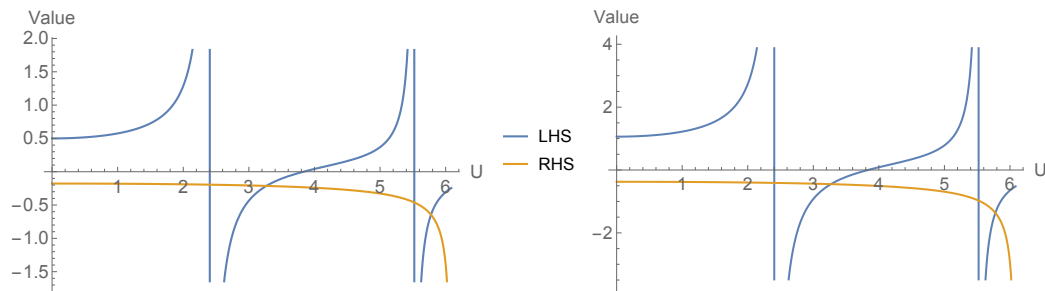
FIGURE 2.3. Graphical solutions to the characteristic equation with $\nu = 0$. LHS = left-hand side. RHS = right-hand side. Left: TE characteristic equation, 2.26. Right: TM characteristic equation, 2.27. The vertical blue lines do not produce solutions where they intersect with the gold curve.

Expressions for the field components of a step-index fiber from [48] are given in Table 2.2 with $a_1 = (F_2 - 1)/2$, $a_2 = (F_2 + 1)/2$, $a_3 = (F_1 - 1)/2$, $a_4 = (F_1 + 1)/2$, $a_5 = (F_1 - 1 + 2\Delta)/2$, $a_6 = (F_1 + 1 - 2\Delta)/2$, $F_1 = \left(\frac{UW}{V}\right)^2 \left(\frac{b_1 + (1 - 2\Delta)b_2}{\nu}\right)$, $F_2 = \left(\frac{V}{UW}\right)^2 \left(\frac{\nu}{b_1 + b_2}\right)$, $b_1 = \frac{J'_\nu(U)}{U J_\nu(U)}$, $b_2 = \frac{K'_\nu(W)}{W K_\nu(W)}$, $h_0 = \sqrt{\frac{\epsilon_0}{\mu_0}}$, and $\Delta = (1 - n_{cl}^2/n_{co}^2)/2$.

TABLE 2.2 Exact field distributions for a single-step-index fiber with expressions from [48]. F.C. abbreviates field component.

F. C.	Core	Cladding
E_ρ	$-\left(\frac{a_1 J_{\nu-1}(U\rho/a) + a_2 J_{\nu+1}(U\rho/a)}{J_\nu(U)}\right)$	$-\frac{U}{W}\left(\frac{a_1 K_{\nu-1}(W\rho/a) - a_2 K_{\nu+1}(W\rho/a)}{K_\nu(W)}\right)$
E_ϕ	$-\left(\frac{a_1 J_{\nu-1}(U\rho/a) - a_2 J_{\nu+1}(U\rho/a)}{J_\nu(U)}\right)$	$-\frac{U}{W}\left(\frac{a_1 K_{\nu-1}(W\rho/a) + a_2 K_{\nu+1}(W\rho/a)}{K_\nu(W)}\right)$
E_z	$-i\frac{U}{\beta a}\frac{J_\nu(U\rho/a)}{J_\nu(U)}$	$-i\frac{U}{\beta a}\frac{K_\nu(W\rho/a)}{K_\nu(W)}$
H_r	$h_0\frac{n_{co}^2}{n_{eff}}\left(\frac{a_3 J_{\nu-1}(U\rho/a) - a_4 J_{\nu+1}(U\rho/a)}{J_\nu(U)}\right)$	$h_0\frac{n_{co}^2}{n_{eff}}\frac{U}{W}\left(\frac{a_5 K_{\nu-1}(W\rho/a) + a_6 K_{\nu+1}(W\rho/a)}{K_\nu(W)}\right)$
H_ϕ	$-h_0\frac{n_{co}^2}{n_{eff}}\left(\frac{a_3 J_{\nu-1}(U\rho/a) + a_4 J_{\nu+1}(U\rho/a)}{J_\nu(U)}\right)$	$-h_0\frac{n_{co}^2}{n_{eff}}\frac{U}{W}\left(\frac{a_5 K_{\nu-1}(W\rho/a) - a_6 K_{\nu+1}(W\rho/a)}{K_\nu(W)}\right)$
H_z	$-ih_0\frac{UF_2}{ka}\frac{J_\nu(U\rho/a)}{J_\nu(U)}$	$-ih_0\frac{UF_2}{ka}\frac{K_\nu(W\rho/a)}{K_\nu(W)}$
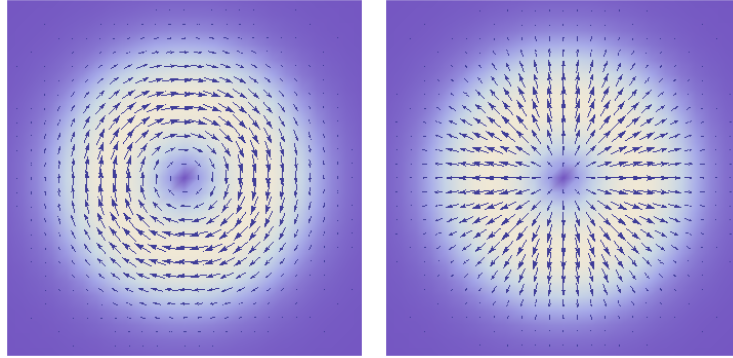
FIGURE 2.4. Electric field distributions for $TE_{0,1}$ and $TM_{0,1}$ modes.

Visualizations of the vector structure of $TE_{0,1}$ and $TM_{0,1}$ are shown in Fig. 2.4. For the EH and HE modes, solutions to the characteristic equation are found by iterating the graphical solution through values of ν. Unlike for the TE and TM modes, there are two parities of each EH and HE mode, denoted with superscripts e

TABLE 2.3 U values for the exact modes

Mode	U	Mode	U
$HE_{1,1}$	2.06018	$HE_{1,2}$	4.65069
$TE_{0,1}$	3.26685	$TE_{0,2}$	5.77635
$TM_{0,1}$	3.26889	$TE_{0,2}$	5.77729
$HE_{2,1}$	3.26830	$HE_{2,2}$	5.77743
$EH_{1,1}$	4.35442		
$HE_{3,1}$	4.35555		

for even or o for odd, which refer to parity under inversion about the horizontal- or x-axis [48, p. 67]. The modes visualized in this section are all even parity, and the odd parity mode distributions are the even modes rotated counterclockwise by 90°. The exact vector modes have locally linear polarization and a whole-beam[3] degree of polarization of zero due to the spatial inhomogeneity [41].

Graphical solutions to the hybrid field characteristic equations[4] for $\nu = 1$ are shown in Fig. 2.5. The $HE_{1,1}$ mode is the fundamental mode, and it and the next radial mode, $HE_{1,2}$, are shown in Fig. 2.6. The polarization in the outer lobe of the $HE_{1,2}$ points opposite to the inner lobe due to a π phase difference between the lobes. The $EH_{1,1}$ mode and $HE_{3,1}$ modes are both in the IOAM= 2 group, and have complicated polarization structure, as shown in Fig. 2.7. However, their superposition creates a uniformly polarized profile referred to as a "clover" mode, due to its resemblance to a four-leaf clover. These mode combinations will be discussed more in section 2.4.

The $\nabla_t \ln [n^2]$ term in Eqn. 2.22 prevents analytical solutions from being tractable in all but the simplest geometries, such as the step-index fiber case detailed

---

[3] "Whole-beam" polarization parameters are found by integration over the whole transverse extent of the beam in calculating the normalized Stokes parameters, which are then used to calculate the degree of polarization. For more information, see Sec. 4.2.

[4] Eqns. 2.25 with both sides multiplied by U to simplify curve behavior.
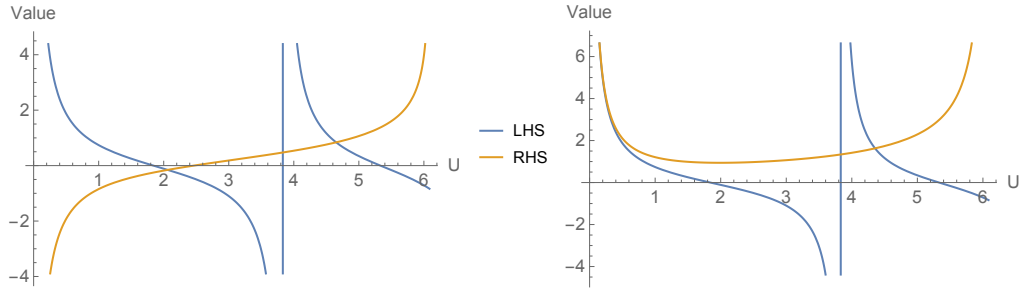
FIGURE 2.5. Graphical solutions to the characteristic equation for $\nu = 1$. LHS = left-hand side. RHS = right-hand side. Left: HE characteristic equation. The vertical blue lines do not represent solutions where they intersect with the gold curve. Right: EH Characteristic equation. The curves do not intersect below $U = 4$, and the lowest-order solution occurs at $U = 4.35442$.
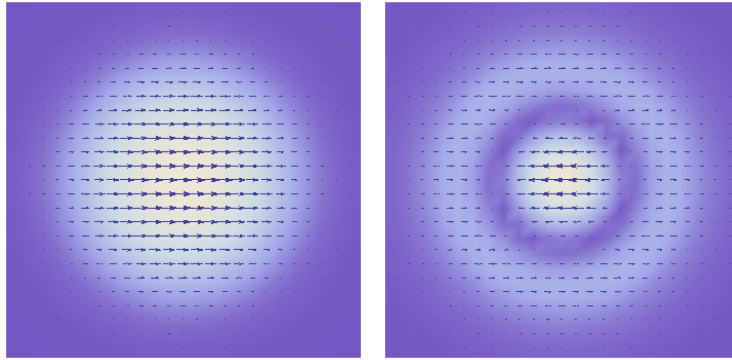
FIGURE 2.6. Electric fields of the $HE_{1,1}$ and $HE_{1,2}$ modes.

above. Neglecting this term simplifies the field distributions and generates uniformly polarized approximate solutions that are easier to work with and can be perturbatively corrected to well-approximate exact mode behavior.

2.4 Scalar Modes

In the regime where $n_{co} \approx n_{cl}$, the gradient $\nabla_t \ln [n^2] \approx 0$ and the wave equations simplify substantially. This "weakly guiding" approximation, as it is widely referred to in the literature, make for electric and magnetic field distributions with negligible

24
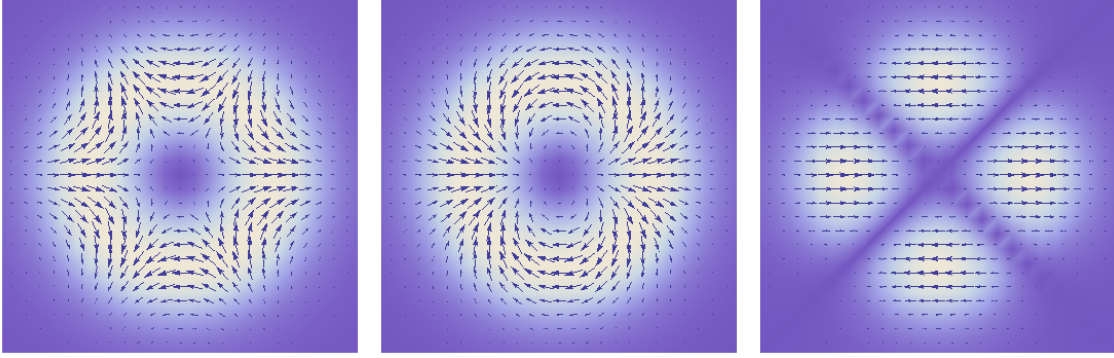
FIGURE 2.7. The $HE_{3,1}$ (left) and $EH_{1,1}$ (middle) mode electric field distributions, which combine to make a clover profile (right). The fringes along the anti-diagonal of the clover combination are numerical artifacts.

z-components, *i.e.* quasi-TEM behavior where $\vec{E} \approx \vec{E}_t$ and $\vec{H} = \vec{H}_t$ [48, p. 115]. As Snyder and Love note in Optical Waveguide Theory, one of the standard texts describing optical fibers, the name can be misleading in that light is still strongly confined and can be guided long distances [41, p. 281]. It might be better thought of as the "quasi-homogeneous," or "low-contrast" approximation. Just as in Fresnel reflection at a planar interface [48],

$$r_\perp = \frac{\cos(\theta_i) - (n_2/n_1)\cos(\theta_t)}{\cos(\theta_i) + (n_2/n_1)\cos(\theta_t)} \tag{2.28}$$

$$r_\parallel = \frac{\cos(\theta_i) - (n_1/n_2)\cos(\theta_t)}{\cos(\theta_i) + (n_1/n_2)\cos(\theta_t)}, \tag{2.29}$$

where θ_i is the angle of incidence and θ_t is the angle of refraction, similar refractive indices makes for reflection behavior that is similar for both polarizations because $n_2/n_1 \approx n_1/n_2$. Neglecting the $\nabla_t \ln [n^2]$ term in the vector wave equation ignores the effects of polarization on reflection, and to neglect the effect of polarization at the interface on the spatial distribution of the fields is to neglect spin-orbit interaction.

The simplified scalar wave equation is

$$\left(\nabla_t^2 + k^2 n^2 - \tilde{\beta}^2\right) F_{\ell,m}(\rho, \phi) = 0, \tag{2.30}$$

where $\tilde{\beta}$ is the approximate propagation constant, n is the local refractive index, ℓ is the OAM quantum number, m is the radial quantum number, and $F_{\ell,m}(\rho, \phi)$ is a scalar field representing the magnitude of the electric field. The common solutions to the scalar wave equation assume a linear-polarization basis ($\hat{e}_j$ where $j \in \{x, y\}$), and compose the so-called linearly polarized (LP) modes with

$$\vec{E}_t(\rho, \phi) = F_{\ell,m}(\rho, \phi)\hat{e}_j \tag{2.31}$$

$$\vec{H}_t = \sqrt{\frac{\epsilon_0}{\mu_0}} n_{\text{eff}} \left(\hat{z} \times \vec{E}_t\right), \tag{2.32}$$

where ϵ_0 and μ_0 are, respectively, the permittivity and permeability of free space, $F_{\ell,m}(\rho, \phi) = \psi_{|\ell|,m}(\rho) f(\ell\phi)$ is the transverse spatial distribution with radial distribution $\psi_{|\ell|,m}(\rho)$, and $f(x) = \cos(x)$ for even parity modes and $f(x) = \sin(x)$ for odd parity modes. LP modes are have degenerate $\tilde{\beta}$ for both parities and polarizations, which makes the fundamental doubly degenerate in polarization (there is only one spatial parity for the fundamental), and all higher-order modes fourfold degenerate.

Instead of using the LP basis, we are free to choose an OAM and SAM modal eigenbasis that is simply related to the LP modes through linear combinations, and we call this the circularly polarized (CP) basis with polarizations $\hat{e}_\sigma = \hat{e}_x + i\sigma\hat{e}_y$ where $\sigma = \pm 1$ is the helicity or handedness (+ = left-circular, - = right-circular) of the SAM, and $F_{\ell,m}(\rho, \phi) = \psi_{|\ell|,m}(\rho)[\cos(\ell\phi) + i\mu\sin(\ell\phi)] = \psi_{|\ell|,m}(\rho)e^{i\ell\phi}$ has characteristic orbital

angular momentum phase structure with integer-valued OAM quantum number, ℓ, and sign (handedness) $\mu = \ell/|\ell|$.

Instead of parity, CP modes are degenerate in μ. LP and CP modes are respectively denoted $\text{LP}_{|\ell|,m}$ and $\text{CP}_{\ell,m}$ where m is the radial quantum number, as with the exact mode solutions, but the first index is the IOAM quantum number associated with the mode. LP modes, as written here, are superpositions of IOAM eigenmodes that carry no net OAM, but $|\ell|$ denotes the number of nodal lines in the field profile. The $\tilde{\beta}$ values that solve 2.30 for LP and CP modes are identical. Scalar modes have a polarization separable from the spatial distribution, and π phase shifts between adjacent radial or azimuthal lobes cause field vectors to point in opposite directions in different lobes at a particular instant in time.

For a single-step-index fiber or radius a, imposing the continuity of $\psi_{|\ell|,m}$ at the interface leads to the scalar characteristic equation

$$U\frac{J_{|\ell|+1}(U)}{J_{|\ell|}(U)} = W\frac{K_{|\ell|+1}(W)}{K_{|\ell|}(W)}, \tag{2.33}$$

where J represents Bessel functions of the first kind, K represents Bessel functions of the second kind, and the radial distribution is

$$\psi_{|\ell|,m}(\rho) = \begin{cases} \frac{J_{|\ell|}(U\rho/a)}{J_{|\ell|}(U)} & \rho \le a \quad \text{(core)} \\[2mm] \frac{K_{|\ell|}(W\rho/a)}{K_{|\ell|}(W)} & \rho > a \quad \text{(cladding)} \end{cases} \tag{2.34}$$

Observant readers will note that the m index is not explicitly present on the right-hand side, but is hidden in the particular U and W values for a mode. So, the full

description for the electric field of a CP mode is

$$\vec{\mathrm{CP}}_{\ell,m}(\rho, \phi, z) = \psi_{|\ell|,m}(\rho)e^{i\ell\phi}e^{i(\tilde{\beta}z-\omega t)}\hat{e}_\sigma. \tag{2.35}$$

Graphical solutions to the scalar characteristic equation and corresponding modal intensity distributions for CP modes are shown in Fig. 2.8 with U value solutions presented in Table 2.4.
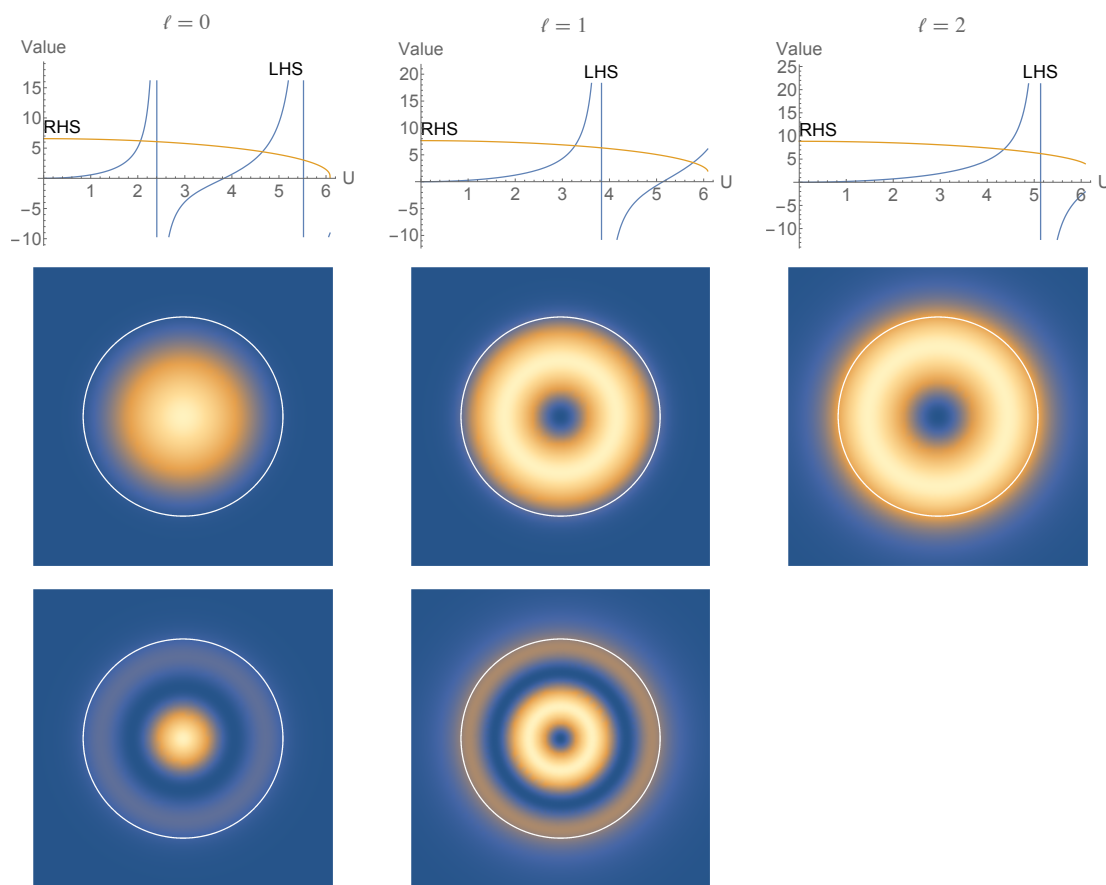
FIGURE 2.8. Scalar mode characteristic equations and transverse intensity $|\psi_{|\ell|,m}(\rho, \phi)|^2$. Columns have consistent OAM value, ℓ.

In the weakly guiding regime, the exact vector modes $\mathrm{HE}_{|\ell|+1,m}$ and $\mathrm{EH}_{|\ell|-1,m}$ tend towards the same β, and linear combinations of them create $\mathrm{LP}_{\ell,m}$ "modes"

TABLE 2.4 Scalar mode U values.

Mode	U	Mode	U
$CP_{0,1}$	2.05932	$CP_{0,2}$	4.64940
$CP_{1,1}$	3.26685	$CP_{1,2}$	5.77635
$CP_{2,1}$	4.35355		

and vice versa. The mathematics of this are explored in more depth in Appendix A. The physics underlying this is the spin-IOAM interaction giving rise to the fine structure of the modal β space. The index ν is the z-component of the total angular momentum $\hat{J}_z = \hat{L}_z + \hat{S}_z$, with hats indicating operators. The modes are quantized such that the eigenvalues of $\hat{L}_z$ are integers and the eigenvalues of $\hat{S}_z$ are $\sigma = \pm 1$ for the photon. These eigenvalues have the same sign for parallel combinations in $HE_{|\ell|+1,m}$ modes, and opposite signs for anti-parallel combinations in $EH_{\nu-1,m}$ modes. The TE and TM modes correspond to total angular momentum zero combinations. The IOAM=1 mode family of $CP_{1,m}$ scalar approximate modes (corresponding to exact modes $TE_m, TM_m,$ and $HE_{2,m}$), behaves uniquely. All other families with IOAM maintain the degeneracy within parallel and anti-parallel combination pairs, which correspond to the two degenerate parities of EH and HE modes in section 2.3. This degeneracy is broken in the IOAM=1 case for photons only. It is not broken in the analogous electron waveguide case, where the half-integer electron spin cannot combine with IOAM to produce total angular momentum (TAM) zero [14]. This suggests the existence of an interpretation where the photon modes "avoid" TAM=0 combinations, as solutions to Maxwell's equations cannot have TAM=0. This behavior gives rise to three possible beat frequencies when exciting IOAM=1 combinations, so we avoid this added complexity by investigating IOAM=2 modes.

As with Russell-Saunders coupling in atoms, the scalar modes can be perturbatively corrected to a $\beta = \tilde{\beta} + \delta\beta$ value that approximates the exact propagation constants.

2.5 Perturbative Correction

The propagation constants for scalar modes can be perturbatively corrected to well approximate the exact ones [14, 41, 48]. These corrections are widely known in fiber theory as the "polarization corrections," as they correct for the influence of polarization ignored by neglecting the $\nabla_t \ln [n^2]$ term in the vector wave equation. For clarity, we differentiate the vector-valued approximate transverse electric field, $\tilde{e}_t = F_{\ell,m}(\rho, \phi)\hat{e}$, from the solutions to the scalar wave equation from the transverse part of the electric field solution to the vector wave equation, $\vec{E}_t$. This approach is based off of taking the difference between the scalar wave 2.30 and vector wave 2.22 equations, assuming that the transverse field distributions are nearly the same $\tilde{e}_t \approx \vec{E}_t$, and finding the difference in propagation constants squared,

$$\delta\left[\beta^2\right] = \beta^2 - \tilde{\beta}^2 = -\frac{\int_A (\nabla_t \cdot \tilde{e}_t)\,(\tilde{e}_t \cdot \nabla_t \ln[n^2])\,\mathrm{d}A}{\int_A |\tilde{e}_t|^2\,\mathrm{d}A}, \qquad (2.36)$$

where A is the entire cross-sectional fiber area, and the correction integral is being taken over the scalar $\tilde{e}_t$. It is not necessary to know $\vec{E}_t$ to calculate the perturbation (as is standard for perturbation theory). The fully corrected propagation constant is

$$\beta = \sqrt{\tilde{\beta}^2 + \delta\beta^2}. \qquad (2.37)$$

However, a good approximation that makes the mode combination mathematics more straightforward [31, Eqn. 5.80] is to assume a linear correction $\beta = \tilde{\beta} + \delta\beta$, substitute

30

into the difference, and note $\beta^2 - \tilde{\beta}^2 \approx 2\tilde{\beta}\delta\beta$ after dropping small term $\delta\beta^2$, so

$$\delta\beta = \frac{\delta[\beta^2]}{2\tilde{\beta}}. \qquad (2.38)$$

The scalar product in the correction integral separates into two terms

$$\nabla_{\mathrm{t}} \cdot \tilde{e}_{\mathrm{t}} = \frac{1}{\rho}\left(\frac{\mathrm{d}(\rho\,\tilde{e}_r)}{\mathrm{d}\rho} + \frac{\mathrm{d}(\tilde{e}_\phi)}{\mathrm{d}\phi}\right), \qquad (2.39)$$

which yield two correction integrals. The corrections (using the linear correction approach), for the radial and azimuthal terms respectively, are

$$\delta\beta_1 = \frac{-1}{2\tilde{\beta}}\left[\int_0^\infty \psi_{|\ell|,m}(\rho)\left(\frac{\mathrm{d}\psi_{|\ell|,m}(\rho)}{\mathrm{d}\rho}\right)\left(\frac{1}{n^2(\rho)}\frac{\mathrm{d}n^2(\rho)}{\mathrm{d}\rho}\right)\rho\,\mathrm{d}\rho\right]\bigg/\int_0^\infty \psi_{|\ell|,m}^2\rho\,\mathrm{d}\rho$$

$$(2.40)$$

$$\delta\beta_2 = \frac{-1}{2\tilde{\beta}}\left[\sigma\ell\int_0^\infty \psi_{|\ell|,m}^2(\rho)\left(\frac{1}{n^2(\rho)}\frac{\mathrm{d}n^2(\rho)}{\mathrm{d}\rho}\right)\mathrm{d}\rho\right]\bigg/\int_0^\infty \psi_{|\ell|,m}^2\rho\,\mathrm{d}\rho. \qquad (2.41)$$

In the remainder of this section, we consider combinations of modes with the same $|\ell|$. In general, $\delta\beta = \delta\beta_1 + \delta\beta_2$, but $\delta\beta_1$ corrections are the same for modes with the same $|\ell|$, and we are interested in mode splitting, rather than mere shifting. Thus, we neglect $\delta\beta_1$ and the separable overall phase factor it contributes by taking $\delta\beta = \delta\beta_2$, in the following analysis. The linearized correction to the propagation constant takes

$$F_{\ell,m}(\rho,\phi)e^{-i\omega t}e^{i\tilde{\beta}z}\hat{e}_\sigma \rightarrow F_{\ell,m}(\rho,\phi)e^{-i\omega t}e^{i(\tilde{\beta}-\sigma\mu|\delta\beta|)z}\hat{e}_\sigma \qquad (2.42)$$

where $\sigma\mu = +1$ corresponds to parallel modes where the z-components of IOAM and SAM are co-oriented, and the spin-orbit propagation constant correction is negative, while $\sigma\mu = -1$ correspond to anti-parallel modes, where the z-components of IOAM

31

and SAM are oriented in opposite directions and the propagation constant correction is positive. Table 2.5 compares exact and scalar mode U values and shows corrections for the $|\ell| = 2$ modes.

TABLE 2.5 Comparison of exact, scalar, and corrected modal constants. Corrected U values for $|\ell| = 2$ modes are found by using $U = a\sqrt{k^2 n_{\text{co}}^2 - \beta^2}$ on the linear correction to β from Eq. 2.38 to get $\tilde{U}$, and the full correction of Eq. 2.37 to get $\bar{U}$.

Scalar Designation	Scalar U	Exact Designation	Exact U	$\tilde{U}$	$\bar{U}$
$CP_{0,1}$	2.05932	$HE_{1,1}$	2.06018		
$CP_{1,1}$	3.26685	$TE_{0,1}$	3.26685		
$CP_{1,1}$	3.26685	$TM_{0,1}$	3.26889		
$CP_{1,1}$	3.26685	$HE_{2,1}$	3.26830		
$CP_{2,1}$	4.35355	$EH_{1,1}$	4.35442	4.35242	4.35299
$CP_{2,1}$	4.35355	$HE_{3,1}$	4.35555	4.35468	4.35412
$CP_{0,2}$	4.64940	$HE_{1,2}$	4.65069		
$CP_{1,2}$	5.77635	$TE_{0,2}$	5.77635		
$CP_{1,2}$	5.77635	$TE_{0,2}$	5.77729		
$CP_{1,2}$	5.77635	$HE_{2,2}$	5.77743		

2.6 Measuring Spin-IOAM Interaction

The spin-orbit interaction manifests as a splitting of parallel and anti-parallel modes. In abstract terms, combining one parallel and one anti-parallel mode produces light with a property that rotates with propagation along the fiber, as the difference in phase velocities makes for a beating effect. There are two ways to combine parallel and anti-parallel modes, *spin-controlled orbital rotation* and *orbit-controlled spin rotation*. In each case, the property that we call the "control property" is common to both modes and its sign controls the direction of rotation while the property associated with the other angular momentum has opposite sign for the parallel and anti-parallel modes, and the combination of the two signs creates a linear feature that rotates with

32

propagation. Description of these effects in terms of the exact fiber modes is given in Appendix A, while combinations in terms of the uniformly polarized CP modes, which give the same results more simply, are given here.

In *spin-controlled orbital rotation*, combinations of CP modes with the same polarization, but opposite IOAM values produce light with constant circular polarization and a clover spatial profile with two nodal lines that rotate with propagation as

$$F_{+|\ell|,m}\hat{e}_\sigma + F_{-|\ell|,m}\hat{e}_\sigma = \psi_{|\ell|,m}(\rho)\left(e^{(i(|\ell|\phi-\sigma|\delta\beta|z))} + e^{-i(|\ell|\phi-\sigma|\delta\beta|z)}\right)\hat{e}_\sigma \qquad (2.43)$$

$$= 2\psi_{|\ell|,m}(\rho)\cos\left[|\ell|\left(\phi - \sigma\left|\frac{\delta\beta}{\ell}\right|z\right)\right]\hat{e}_\sigma. \qquad (2.44)$$

The spatial distribution rotates in the direction set by σ, by an angle $\xi = \sigma\left|\frac{\delta\beta}{\ell}\right|z$.

Orbit-controlled spin rotation is the other combination of parallel and anti-parallel modes. Representing the polarization with a Jones vector in a Cartesian basis, $\hat{e}_\sigma = [1, \sigma i]^T$,

$$F_{\mu|\ell|,m}\hat{e}_+ + F_{\mu|\ell|,m}\hat{e}_- = \psi_{|\ell|,m}(\rho)e^{i\ell\phi}\left(e^{-i\mu|\delta\beta|z}\hat{e}_+ + e^{i\mu|\delta\beta|z}\hat{e}_-\right) \qquad (2.45)$$

$$= 2\psi_{|\ell|,m}(\rho)e^{i\ell\phi}\begin{bmatrix} \cos(|\delta\beta|z) \\ \mu\sin(|\delta\beta|z) \end{bmatrix}, \qquad (2.46)$$

where the spatial distribution is unchanged and the linear polarization rotates with z, in a direction controlled by the OAM handedness μ, by an angle $\tilde{\phi} = \mu|\delta\beta|z$. The orientation of the linear polarization corresponds to the angle $\tilde{\phi}$ on the Poincaré sphere[5], as described in section 4.2.

---

[5]A note on notation: to reconcile conflicting conventions, in this section, we refer to the azimuthal angle in cylindrical coordinates as ϕ and use $\tilde{\phi}$ to refer to the Poincaré sphere coordinate. However,

Thus, the rotation *vs.* distance for the spatial rotation has slope $\frac{d\xi}{dz} \equiv R_s = \sigma \left| \frac{\delta\beta}{\ell} \right|$, and for the polarization rotation is $\frac{d\phi}{dz} \equiv R_p = \sigma |\delta\beta|$. The rotation rates for the two effects differ by a factor of $|\ell|$. If the fiber contains optical activity or other structure that shifts modal propagation constants based on IOAM or SAM value *only*, then the result is a modification of the observed splitting by a constant shift $\pm\delta\beta \to \pm\delta\beta + B$, where B has the same sign for *both* values of the control property (signs of $\delta\beta$). This can be shown by adding a phase factor of the form $\exp(i\sigma B_\sigma)$ or $\exp(i\mu B_\mu)$ to shift each mode, and only effects observed rotation when the added phase factors are not factorable. Thus, cutback experiments also measure birefringence in IOAM and SAM. Spin-orbit interaction does not occur in homogeneous media, such as free space, so excitation of the appropriate modes in a straight fiber iteratively cut to shorter lengths (L) is expected give straight lines for $\tilde{\phi}$ *vs.* L and ξ *vs.* L with slopes R_p and R_s that reveal $\delta\beta$ and birefringence in SAM or IOAM.

---

in all other chapters, ϕ refers to the Poincaré sphere coordinate, and spatial orientations are denoted by ξ. In all cases, it should be clear from context which quantity is intended.

CHAPTER III

TOY SIMULATION

A "toy" simulation uses a simplified model of the system to explore the underlying physics. The goal to get a sense of the elementary mechanisms absent obfuscatory complications. Combinations of two eigenmodes for spin-controlled orbital rotation and orbit-controlled spin rotation have simple behaviors, but evolution of combinations of many modes quickly becomes unwieldy. To investigate these combinations, we made a simulation in Mathematica that combines spatial modes, including phase and polarization information.

The most developed iteration of the code uses LP modes for an arbitrary step-index fiber with parameters described in Table 3.1. The excitation is assumed to be monochromatic.

TABLE 3.1 Fiber parameters used in the toy model simulation.

Description	Property	Value
Core Radius	a	$5.5\,\mu\text{m}$
Wavelength	λ	800 nm
Cladding Index	n_{cl}	1.455
Core Index	n_{co}	1.465
V-Parameter	V	7.381

A combination of two fiber modes indexed by 1 and 2 takes the form

$$\vec{\mathscr{F}}_1 \exp\left[i(\tilde{\beta}_{\ell_1,m_1} - \sigma_1\mu_1\delta\beta_{\ell_1,m_1})z\right] + \vec{\mathscr{F}}_2 \exp\left[i(\tilde{\beta}_{\ell_2,m_2} - \sigma_2\mu_2\delta\beta_{\ell_2,m_2})z\right] \qquad (3.1)$$

where $\vec{\mathscr{F}}_i$ is the transverse spatial distribution, including polarization information, for the mode indexed by i. For CP modes (discussed in Chapter 2.4), the polarization

35

is spatially uniform and can be separated into $\vec{\mathscr{F}}_i = F_{\ell,m}\hat{e}_i$. The distance over which the phase difference reaches 2π is called the beatlength

$$L_B = \frac{2\pi}{\beta_1 - \beta_2} = \frac{\lambda}{n_{\text{eff}}^{(1)} - n_{\text{eff}}^{(2)}}. \qquad (3.2)$$

Beating effects for combinations of modes with common ℓ and m values are independent of the unperturbed propagation constant, $\tilde{\beta}_{\ell,m}$, which factors out as an overall phase factor, leaving a beatlength determined by spin-IOAM interaction, $L_B = \pi/\delta\beta$. Combinations of modes with different ℓ and m values exhibit much faster beating effects dominated by the difference between the unperturbed propagation constants $\tilde{\beta}_{\ell_1,m_1} - \tilde{\beta}_{\ell_2,m_2}$, which make for beatlengths that are too small to resolve experimentally $\left[2\pi/(\tilde{\beta}_{0,1} - \tilde{\beta}_{2,1}) = 47\,\mu\text{m} \text{ and } 2\pi/(\tilde{\beta}_{1,1} - \tilde{\beta}_{2,1}) = 89\,\mu\text{m} \right]$.

To model the beating behavior in a way that approximates what we see in our experiments using a disperson-tailored fiber with a complicated index profile, I used the spatial distributions from solving the scalar characteristic equation, but used a longitudinal propagation constant β_0 from the best simulation effective indices provided by Patrick Gregg of the Ramachandran group at Boston University. Using $m = 1$ for all modes of interest, $\tilde{\beta}_{\ell,1} = n_{\text{eff}}^{(\ell)}k$ and the effective indices at $\lambda = 800$ nm used in the simulation are given in Table 3.2.

TABLE 3.2 Unperturbed effective indices used in simulation.

$n_{\text{eff}}^{(0)}$	1.475
$n_{\text{eff}}^{(1)}$	1.467
$n_{\text{eff}}^{(2)}$	1.458

Input vectorial modes, including overall amplitude and phase, are combined at multiple lengths to simulate the evolution of the polarization properties, *i.e.*

normalized Stokes Q, U, and V parameters, as well as (θ, ϕ, DOP), and both the spatial amplitude distribution and an interferogram from its combination with a horizontally polarized reference beam,

$$
\mathrm{CP}_{0,1} = \psi_{0,1}(\rho)\, \exp[ik_y y] \begin{bmatrix} 1 \\ 0 \end{bmatrix}, \tag{3.3}
$$

with tilt $k_y = 5 \times 10^6\,\mathrm{m}^{-1}$.

In runs reported here, angles θ and ϕ are in Poincaré degrees (recall 2 Poincaré degrees = 1 degree in real space for ϕ), ξ is in real space degrees, and z is in m. In this chapter, modes are abbreviated $\mathrm{CP}^{\sigma}_{\ell,m}$ where $\sigma \in \{+, -\}$ for left- and right-handed circular polarization, so both the modal SAM and IOAM are readily apparent.

3.1 Multimode Propagation

This investigation uses $\delta\beta = 61.08652$ rad/m, set to match the $\sim 35°/$cm rotation rate from the crossed-wire Ti:sapphire experiment detailed in section 5.5, and corresponds to a beatlength of 5.14286 cm. The input modal excitation is summarized in Table 3.3, for convenience.

TABLE 3.3 Index of multimode excitation (MM) runs with input modal excitation.

Run Designation	Input Excitation
RunMM1	$\mathrm{CP}^{+}_{+2,1} + \mathrm{CP}^{-}_{+2,1}$
RunMM2	$\mathrm{CP}^{+}_{+2,1} + \mathrm{CP}^{+}_{-2,1}$
RunMM3	$\mathrm{CP}^{+}_{+2,1} + 0.8\,\mathrm{CP}^{-}_{+2,1}$
RunMM4	$\left(\mathrm{CP}^{+}_{+2,1} + \mathrm{CP}^{-}_{+2,1}\right) + 0.5\left(\mathrm{CP}^{+}_{-2,1} + \mathrm{CP}^{-}_{-2,1}\right)$
RunMM5	$\left(\mathrm{CP}^{+}_{+2,1} + 0.95\,\mathrm{CP}^{-}_{+2,1}\right) + 0.3\left(\mathrm{CP}^{+}_{-2,1} + 1.1\,\mathrm{CP}^{-}_{-2,1}\right)$
RunMM6	$\left(\mathrm{CP}^{+}_{+2,1} + \mathrm{CP}^{-}_{+2,1}\right) + 0.5\left(\mathrm{CP}^{+}_{0,1} + \mathrm{CP}^{-}_{0,1}\right)$
RunMM7	$\mathrm{CP}^{+}_{+2,1} + \mathrm{CP}^{-}_{+2,1}) + 0.3\left(\mathrm{CP}^{+}_{0,1} + \mathrm{CP}^{-}_{0,1}\right)$
RunMM8	$\left(\mathrm{CP}^{+}_{+2,1} + \mathrm{CP}^{-}_{+2,1}\right) + 0.5\left(\mathrm{CP}^{+}_{1,1} + \mathrm{CP}^{-}_{1,1}\right)$

RunMM1: Use input $CP^+_{+2,1}+CP^-_{+2,1}$ to test orbit-controlled spin rotation, with polarization properties shown in Fig. 3.1 and intensity profiles and interferograms shown in Fig. 3.2. The simple analytical description of Eq. 2.46 is correctly reproduced, which is a check that the code is working properly. The interferogram reference beam has constant horizontal linear polarization, so the interference visibility changes as ϕ changes, as expected.
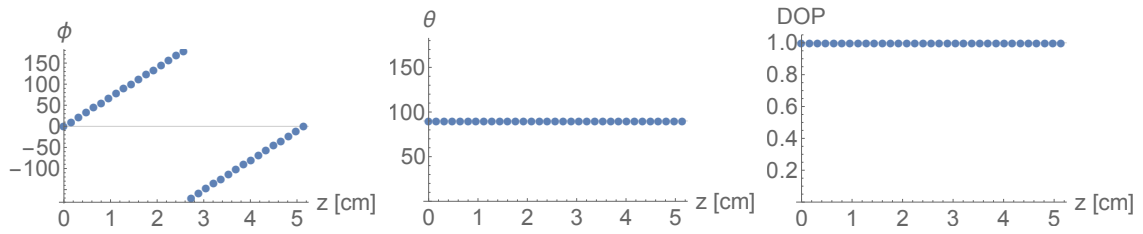
FIGURE 3.1. RunMM1: Polarization information. ϕ rotates at $+70$ Poincaré degrees/cm.

RunMM2: Use input $CP^+_{+2,1} + CP^+_{-2,1}$ to test spin-controlled orbital rotation. Polarization and spatial mode information is shown in Fig. 3.3, and spatial profiles and interferograms are shown in Fig. 3.4.

z [cm]	Intensity	Interferogram
0		
1.28571		
2.57143		
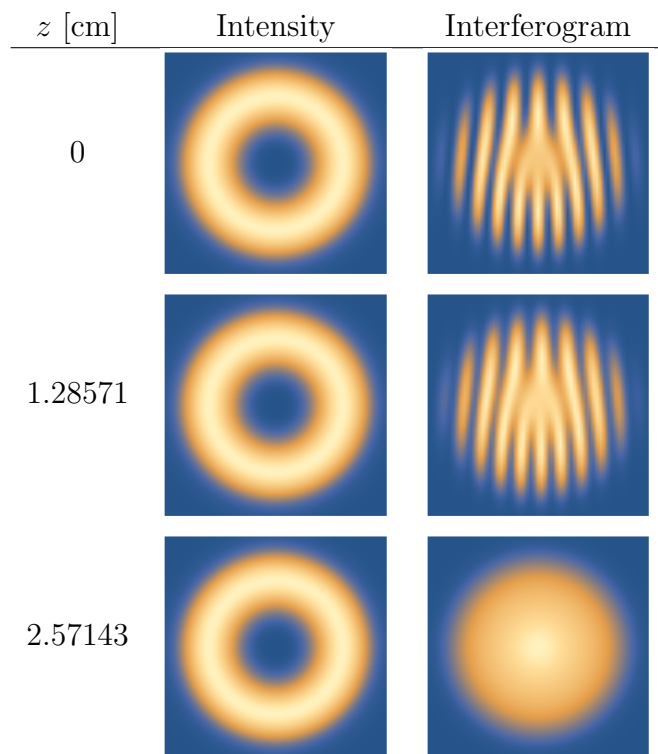
FIGURE 3.2. RunMM1: Intensities and interferograms at various distances. The interference visibility decreases because the linear polarization of the output fiber mode combination ϕ changes as z changes, while the reference has constant horizontal linear polarization. The spatial profile does not change with propagation.
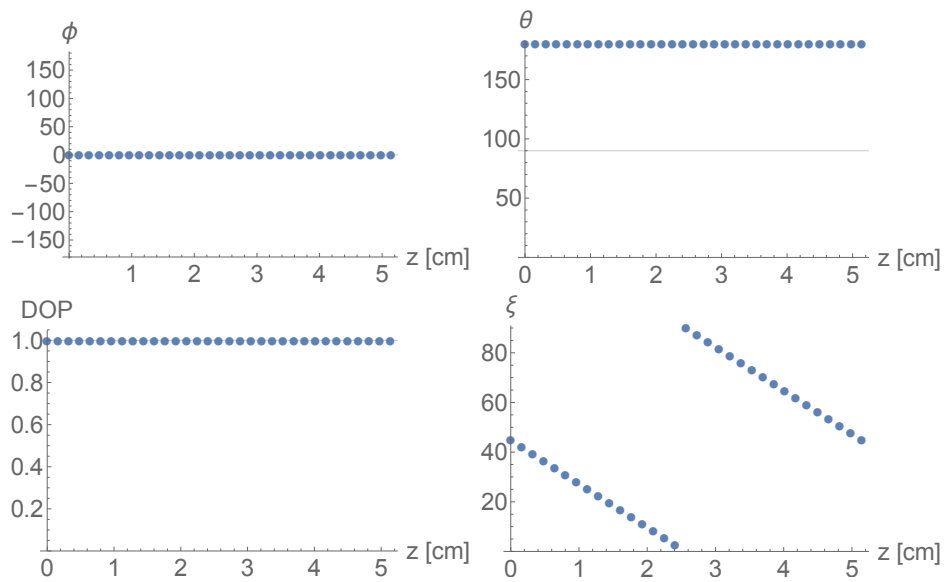
FIGURE 3.3. RunMM2: Propagation of input horizontally polarized $\ell = +2$ profile. Polarization properties, $(\phi, \theta, \text{DOP})$, as well as nodal line orientation ξ for RunMM2. The polarization is invariant while ξ rotates at a rate of $-17.5°/\text{cm}$.

z [cm]	Intensity	Interferogram
0		
1.28571		
2.57143		
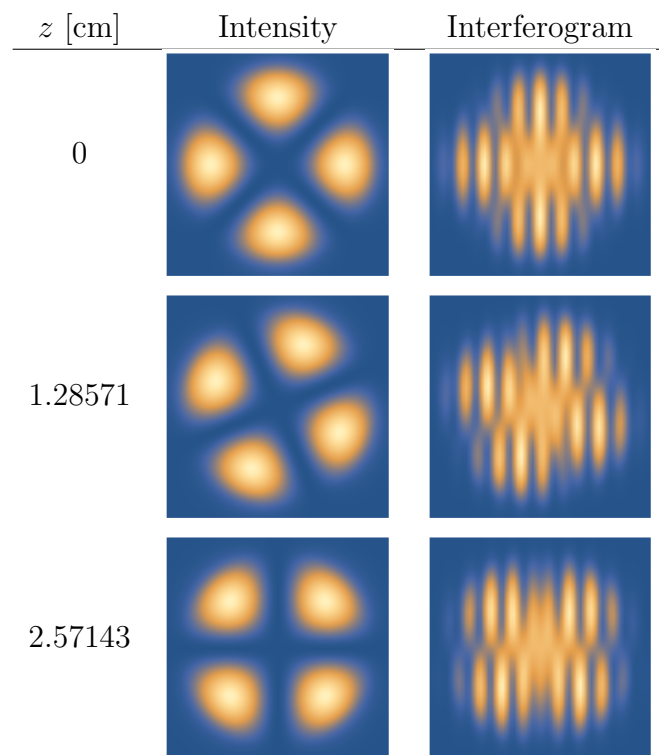
FIGURE 3.4. RunMM2: Intensities and interferograms rotating at a rate of $-17.5°/$cm at three fiber lengths.

RunMM3: Changing the relative amplitude of the modes to $\mathrm{CP}^+_{+2,1}+0.8\mathrm{CP}^-_{+2,1}$ changes the visibility of the interferogram 3.6 and shifts θ to a new value, but does not change the slope of ϕ *vs.* z or the DOP (Fig. 3.5). This illustrates that spin-IOAM causes ϕ to precess around the circular axis of the Poincaré sphere.
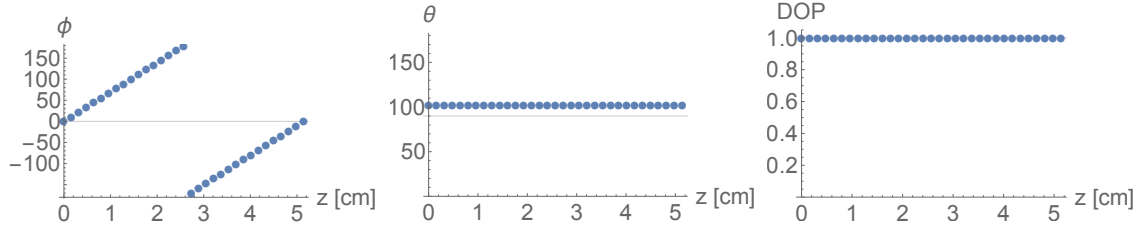
FIGURE 3.5. RunMM3: Polarization information shows the expected rotation in ϕ. Unequal modal excitation amplitudes result in θ being offset from the equator at 90°.

z [cm]	Intensity	Interferogram
0		
1.28571		
2.57143		
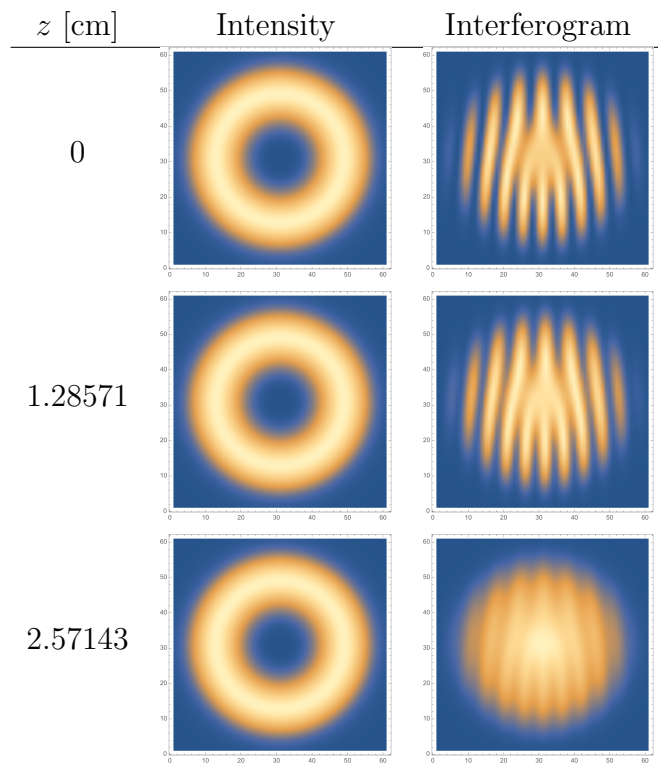
FIGURE 3.6. RunMM3: Intensities and interferograms. The donut intensity profile does not vary with propagation.

RunMM4: Combination of $\left(\mathrm{CP}^+_{+2,1} + \mathrm{CP}^-_{+2,1}\right) + 0.5\left(\mathrm{CP}^+_{-2,1} + \mathrm{CP}^-_{-2,1}\right)$. There is obvious distortion in ϕ *vs.* z, shown in Fig. 3.7. θ is unchanged as long as the linearly polarized combinations in both the first pair of parentheses and second pair of parentheses both are balanced. There are two DOP oscillations over one beatlength, the numerical derivative $\Delta\phi/\Delta z$ shows oscillatory structure, and the spatial profile oscillates between a sine-like clover, a donut, and a cosine-like clover, without continuous rotation of the nodal lines. Spatial profiles and interferograms are shown in Fig. 3.8.
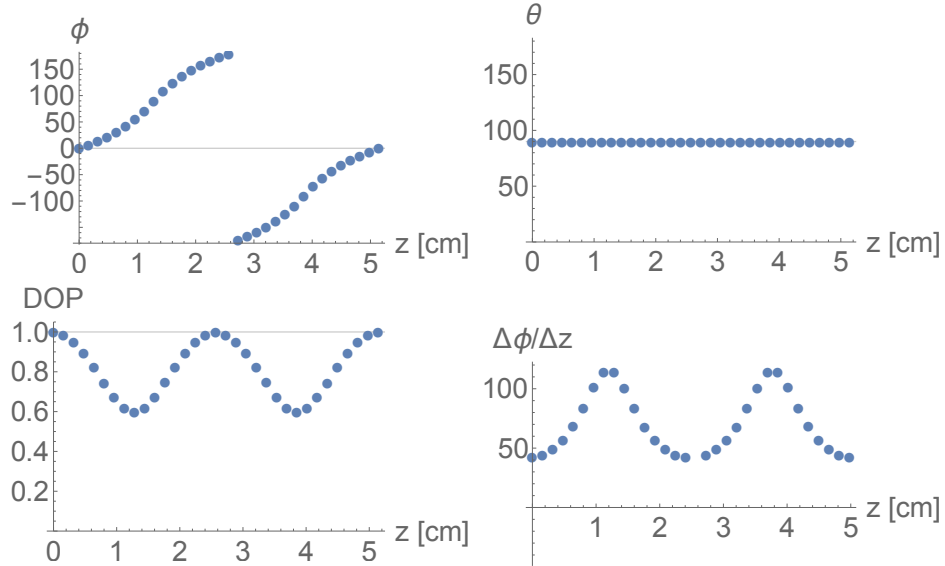
FIGURE 3.7. RunMM4: Polarization information. $\Delta\phi/\Delta z$ is the numerical derivative of ϕ.

RunMM5: Imbalance in the circular polarization "pairs" leads to θ oscillation, as shown in Fig. 3.9. The input excitation is $\left(\mathrm{CP}^+_{+2,1} + 0.95\mathrm{CP}^-_{+2,1}\right) + 0.3\left(\mathrm{CP}^+_{-2,1} + 1.1\mathrm{CP}^-_{-2,1}\right)$. Spatial profiles and interferograms are shown in Fig. 3.10. RunMM4 and runMM5 have very similar spatial profiles, but different visibilities.

44

z [cm]	Intensity	Interferogram	z [cm]	Intensity	Interferogram
0			2.57143		
0.428571			3.42857		
0.857146			3.42857		
1.28571			3.85714		
1.71429			4.2571		
2.14286			4.71429		
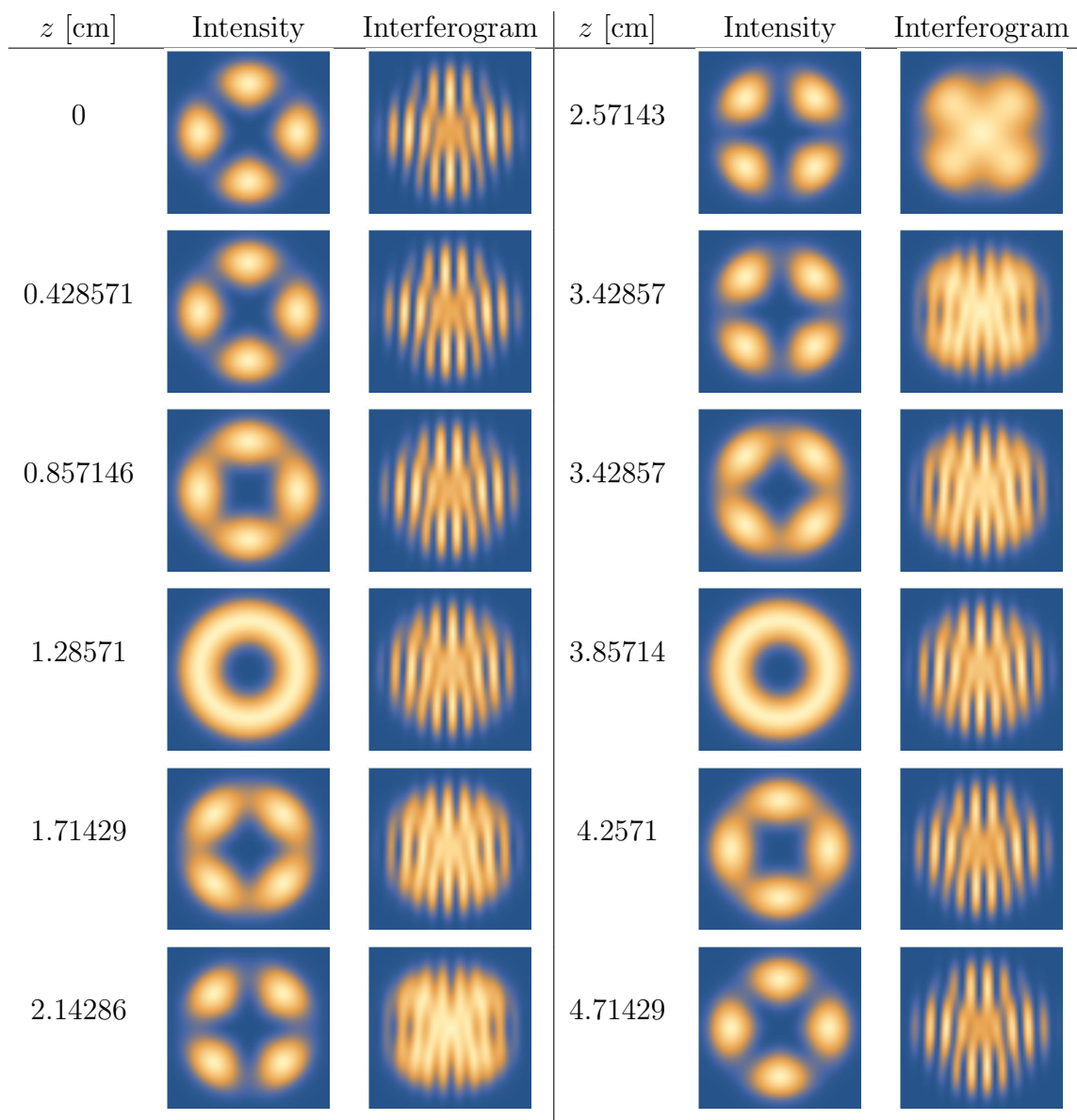
FIGURE 3.8. RunMM4: Intensities and interferograms over one beatlength.
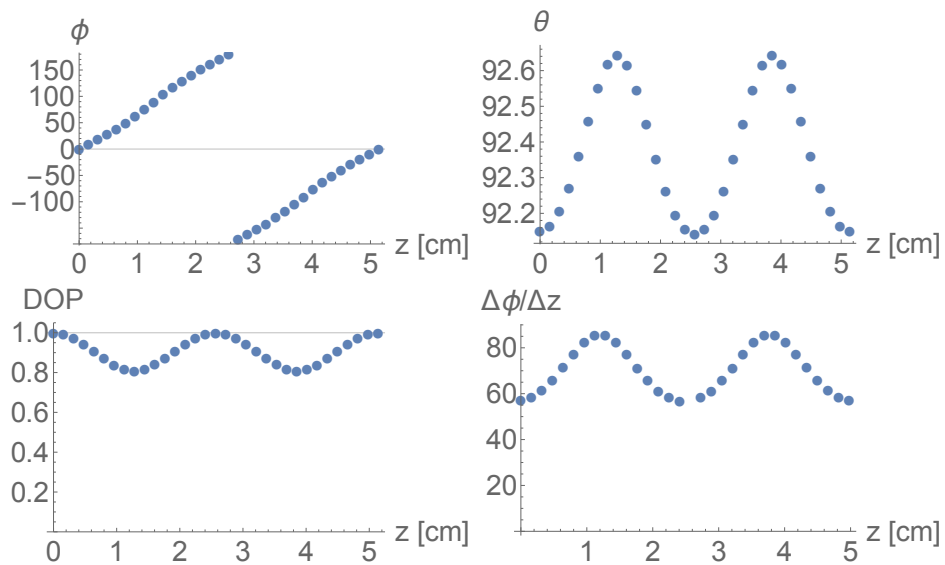
FIGURE 3.9. RunMM5: Polarization. The θ *vs.* z plot is zoomed in to show small variation. $\Delta\phi/\Delta z$ is the numerical derivative of ϕ.

z [cm]	Intensity	Interferogram	z [cm]	Intensity	Interferogram
0			2.57143		
0.428571			3.42857		
0.857146			3.42857		
1.28571			3.85714		
1.71429			4.2571		
2.14286			4.71429		
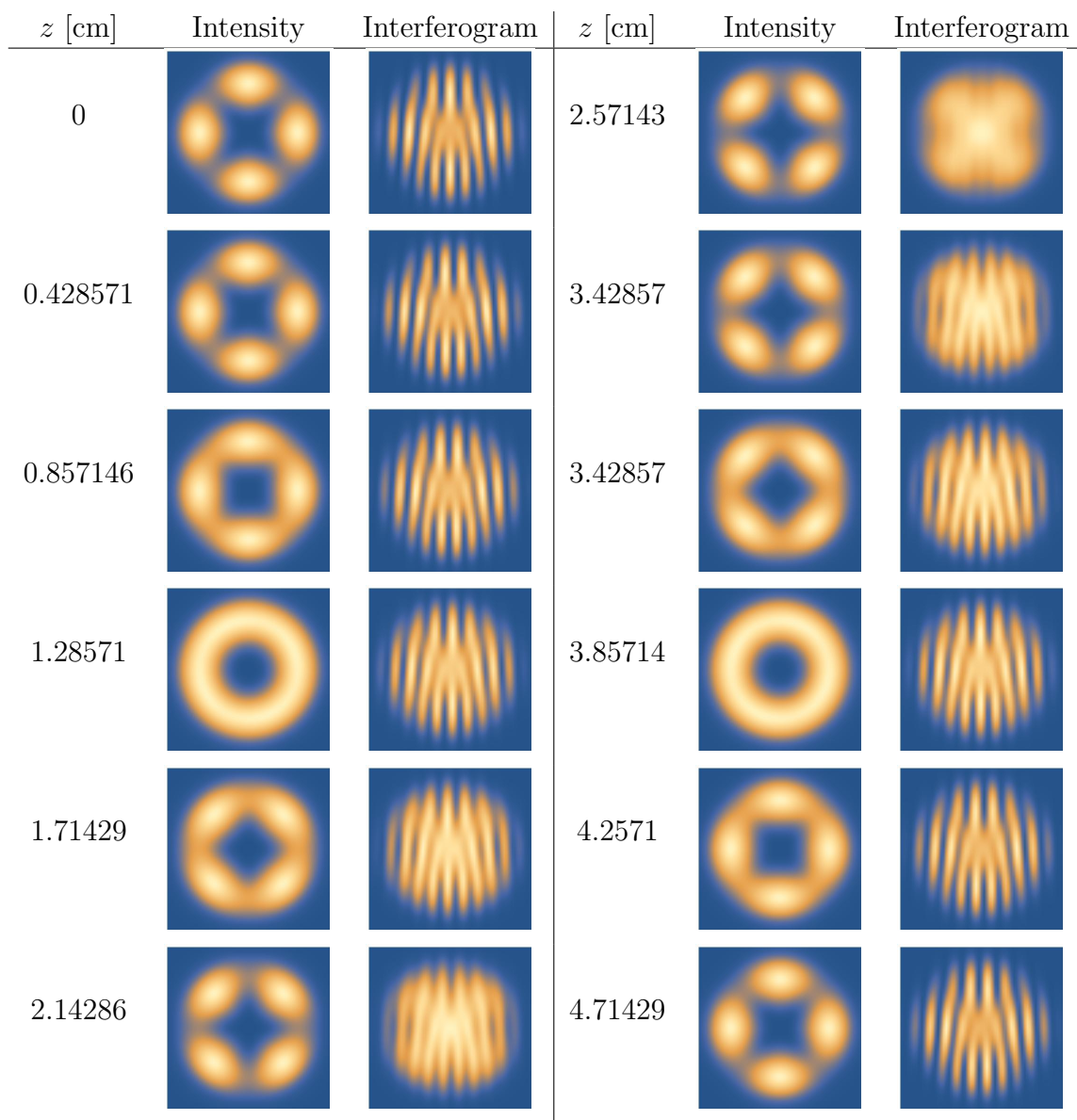
FIGURE 3.10. RunMM5: Intensities and interferograms over one beatlength.

What beating effects occur if the excitation is not limited to parallel and anti-parallel modes with the same IOAM? Combinations of different orders of IOAM gives rise to "clocking" where singularities move around angular positions, as shown in Figs. 3.12, 3.14, and 3.16. An important caveat is that the rotation of the singularities in those figures looks to be periodic over the beatlength shown, but this appearance is due to aliasing and they are actually performing many full rotations between the lengths shown. The visibility changes due to changing polarization do happen on the length scale investigated. We observe singularity clocking in our experiments, but the orientation looks random, which is what we expect since we are far from having the precision length control necessary to resolve the beating between different IOAM orders. It is noteworthy (and expected) that orientations of the singularities are stable at a particular length, showing that the optical path length is stable not just on the scale of the slow SOI rotations, but also on the scale of the more sensitive clocking.

RunMM6: IOAM=2 and IOAM=0: singularity splitting with the input excitation: $\left(\text{CP}_{+2,1}^{+} + \text{CP}_{+2,1}^{-}\right) + 0.5\left(\text{CP}_{0,1}^{+} + \text{CP}_{0,1}^{-}\right)$ is shown in Fig. 3.12. Polarization evolution is shown in Fig. 3.11. The IOAM=0 (fundamental) modes have no spin-IOAM splitting. Addition of the fundamental splits the IOAM=2 singularity into two IOAM=1 singularities separated symmetrically from the center.

RunMM7: IOAM=2 and IOAM=0: singularity splitting with the input excitation: $\left(\text{CP}_{+2,1}^{+} + \text{CP}_{+2,1}^{-}\right) + 0.3\left(\text{CP}_{0,1}^{+} + \text{CP}_{0,1}^{-}\right)$ shown in Fig. 3.14. Polarization information in shown in Fig. 3.13. Reduced amplitude in the IOAM=0 mode compared to runMM6 results in the singularities being closer to the center.

48
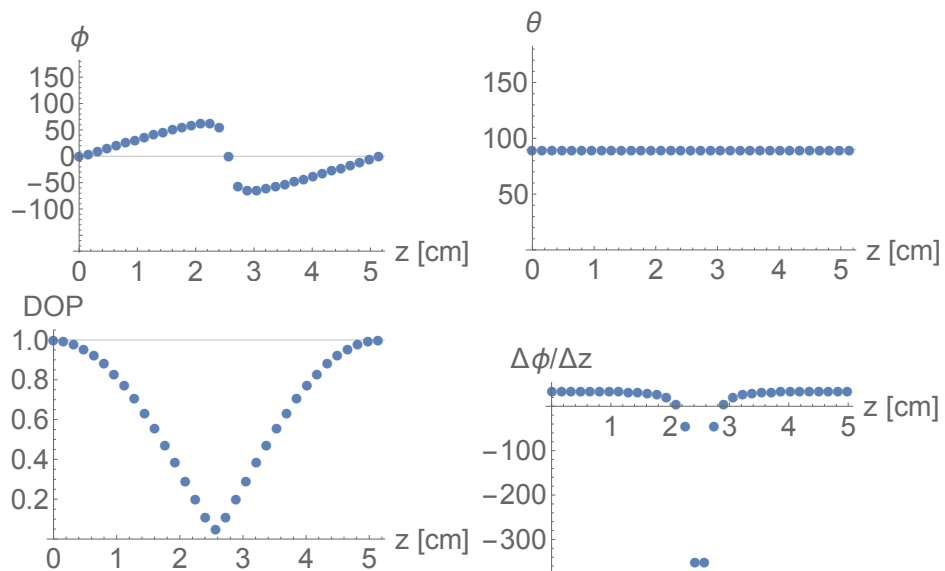
FIGURE 3.11. RunMM6: Polarization information. $\Delta\phi/\Delta z$ is the numerical derivative of ϕ.

z [cm]	Intensity	Interferogram	z [cm]	Intensity	Interferogram
0			2.57143		
0.428571			3.42857		
0.857146			3.42857		
1.28571			3.85714		
1.71429			4.2571		
2.14286			4.71429		

FIGURE 3.12. RunMM6: Intensities and interferograms. The singularity clocking shown here is aliased and performs more than a full rotation between lengths shown here. $\Delta\phi/\Delta z$ asymptotes to about 33.2°/cm.
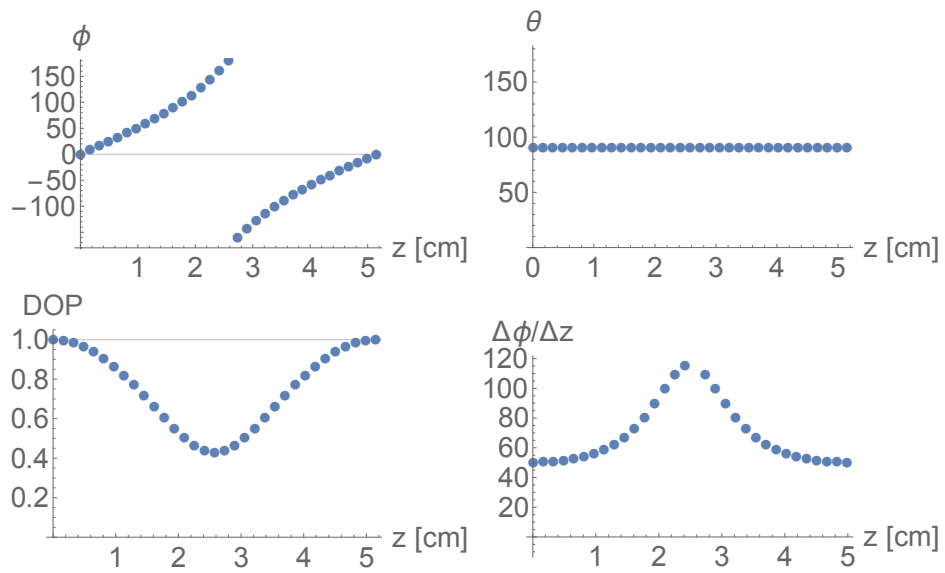
FIGURE 3.13. RunMM7: Polarization information. $\Delta\phi/\Delta z$ is the numerical derivative of ϕ.

z [cm]	Intensity	Interferogram	z [cm]	Intensity	Interferogram
0			2.57143		
0.428571			3.42857		
0.857146			3.42857		
1.28571			3.85714		
1.71429			4.2571		
2.14286			4.71429		
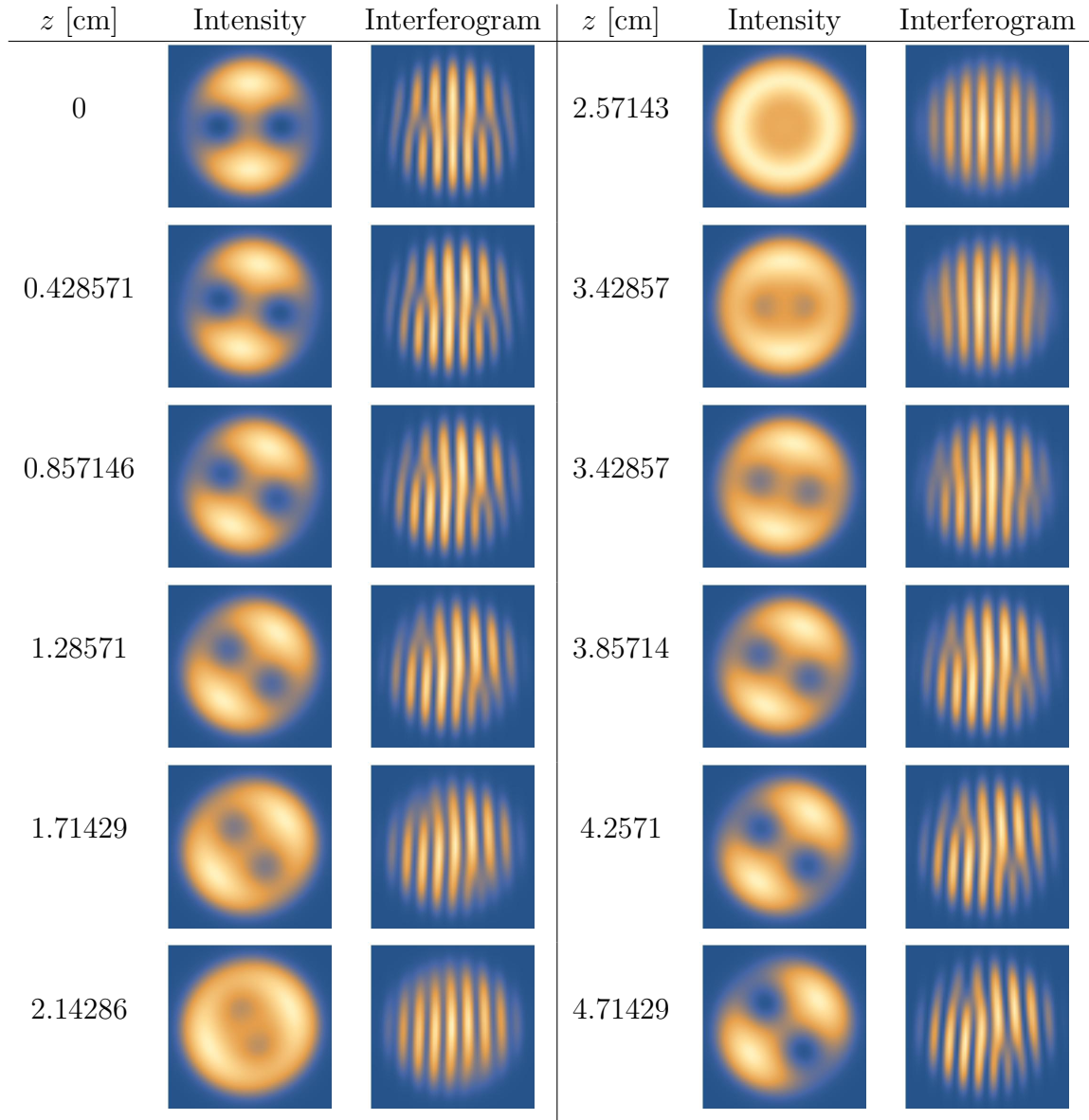
FIGURE 3.14. RunMM7: Intensities and interferograms. The singularity clocking shown here is aliased and performs more than a full rotation between lengths shown here. $\Delta\phi/\Delta z$ asymptotes to about 33.2°/cm.

RunMM8: IOAM=2 and IOAM=1: singularity splitting with input excitation $\left(\mathrm{CP}^+_{+2,1} + \mathrm{CP}^-_{+2,1}\right) + 0.5\left(\mathrm{CP}^+_{1,1} + \mathrm{CP}^-_{1,1}\right)$ shown in Fig. 3.16. Polarization information is shown in Fig. 3.15. Twice as much distance is shown shown in Fig. 3.15 as in previous runs due to a longer beatlength from a smaller assumed splitting, specifically $\delta\beta' = \delta\beta/2$ for IOAM=1.
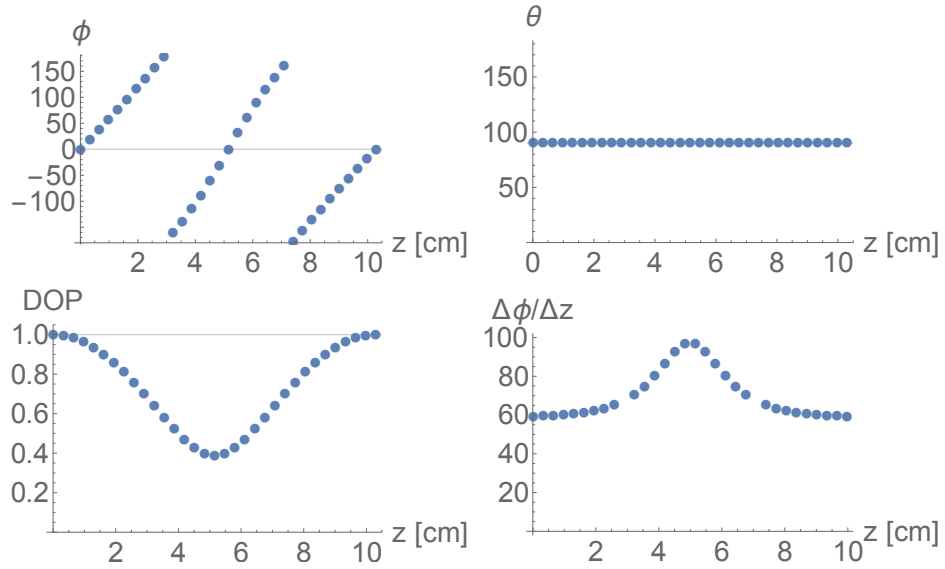
FIGURE 3.15. RunMM8: Polarization information. $\Delta\phi/\Delta z$ is the numerical derivative of ϕ.

In summary, oscillating DOP and deformations to the linearity of ξ or ϕ rotations can result if undesired modes are excited with desired modes. The magnitude of those oscillations indicates the excitation amplitude of the undesired modes.

z [cm]	Intensity	Interferogram	z [cm]	Intensity	Interferogram
0			2.57143		
0.428571			3.42857		
0.857146			3.42857		
1.28571			3.85714		
1.71429			4.2571		
2.14286			4.71429		
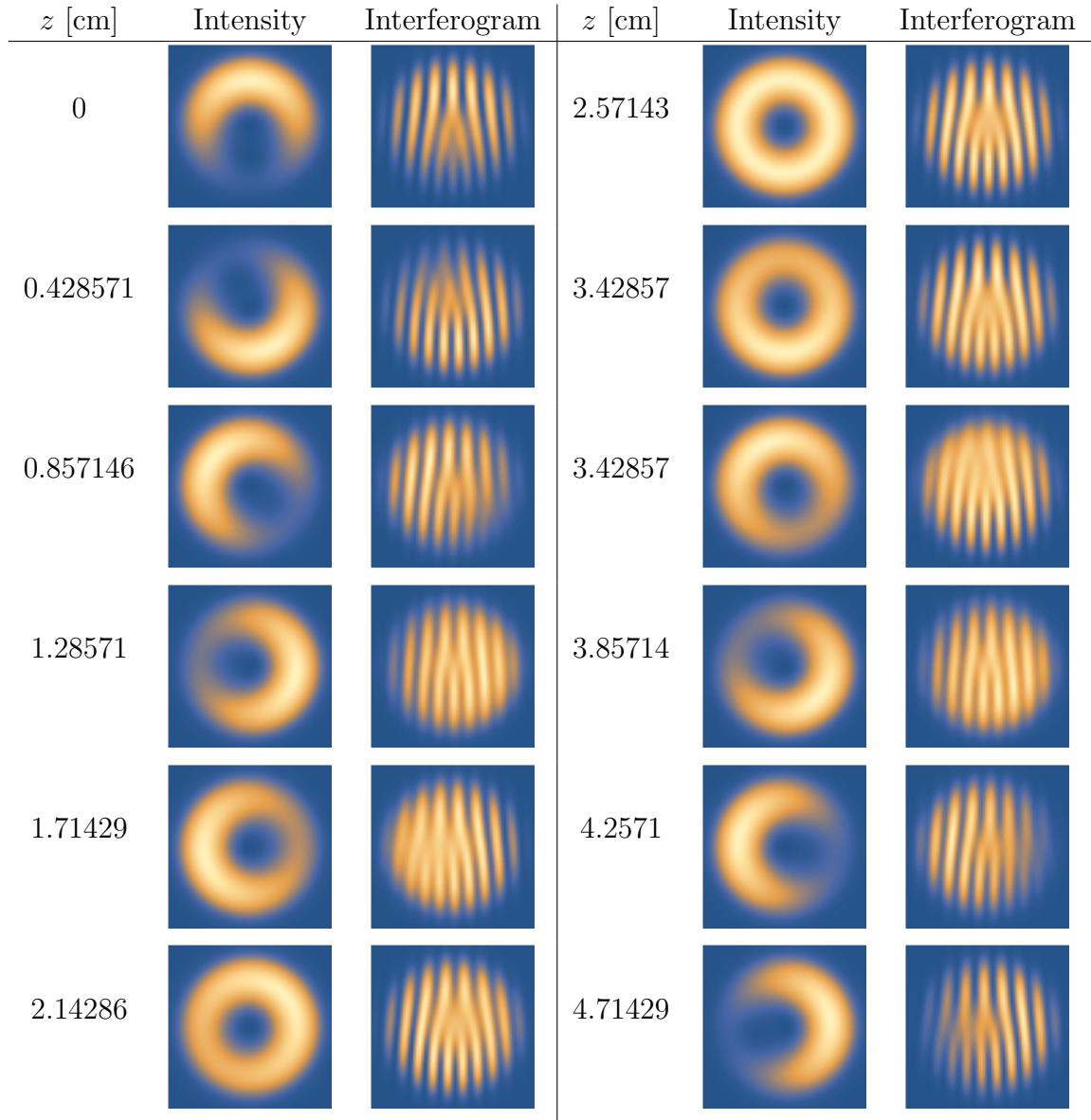
FIGURE 3.16. RunMM8: Intensities and interferograms.The singularity clocking shown here is aliased and performs more than a full rotation between lengths shown here. $\Delta\phi/\Delta z$ asymptotes to about 33.2°/cm.

3.2 Mode Coupling

Ideally, fiber modes are orthogonal, *i.e.* excitation of a single mode at the input will result in emission of the corresponding mode at the output. The output mode may differ from the input mode due to propagation effects, but energy should not be coupled to other fiber modes. Real fibers contain unavoidable imperfections that couple excitation probability between modes. If modes are expected to act as independent channels, then that coupling between channels is referred to as crosstalk. Using a spatial light modulator on the output profiles from a fiber, a crosstalk matrix between modes for a particular configuration can be measured [49].

We model the effects of mode coupling with a constant coupling rate, in a basis of CP modes with IOAM=2 only. In this section, we assume that all modes are lowest order radial modes with $m = 1$, and use a shorthand notation denoting the IOAM and SAM as either '+' or '-' such that CP_{+-} refers to CP mode $F_{+2,1}\hat{e}_{-}$. The same fiber parameters are used in this section as were used in the last section, and are shown in Table 3.1.
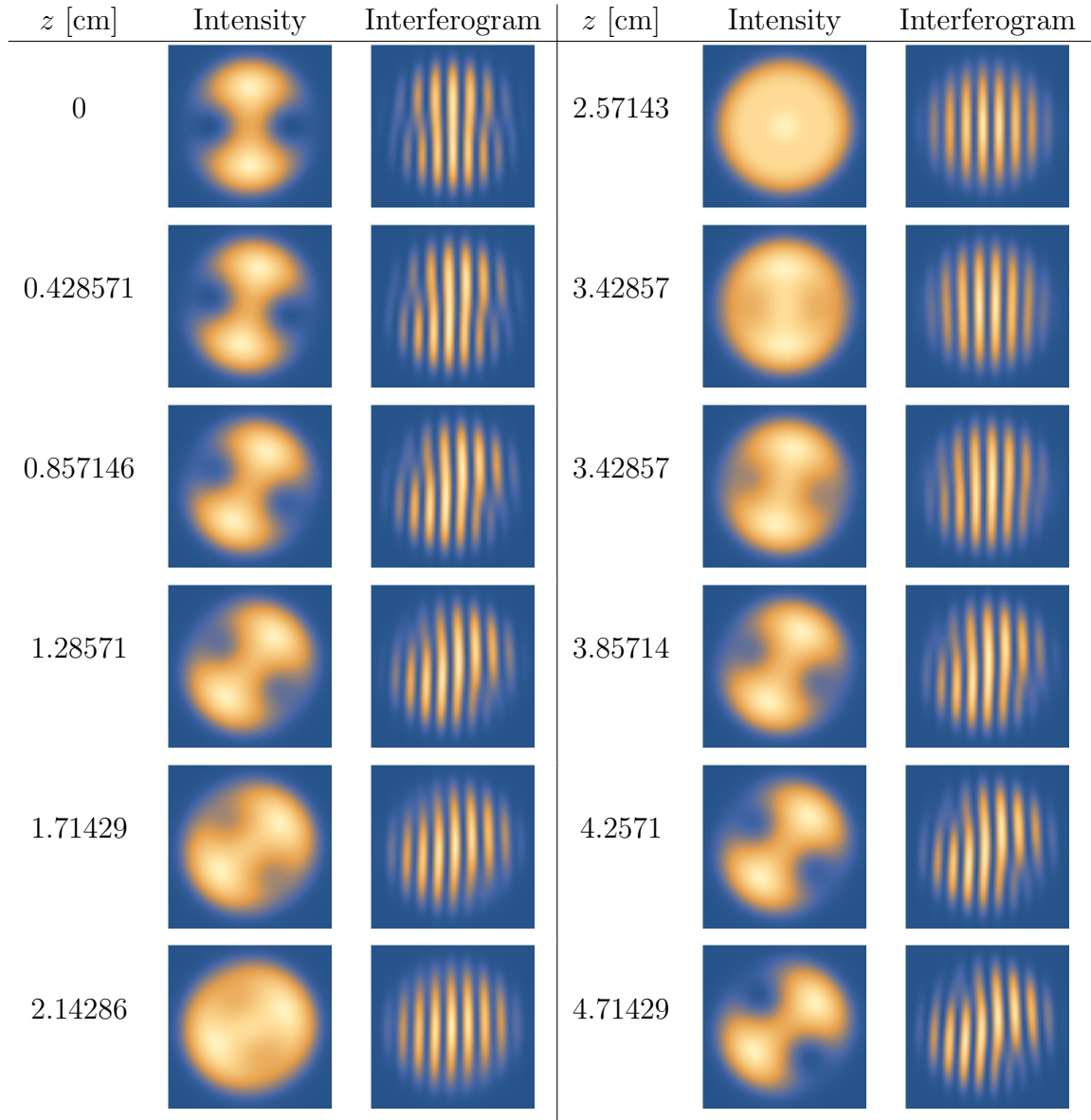
Let the vector of modes be

$$\mathbf{S} = \begin{bmatrix} CP_{++} & CP_{+-} & CP_{--} & CP_{--} \end{bmatrix} \tag{3.4}$$

and the complex excitation amplitudes A of the modes be

$$\mathbf{\Psi} = \begin{bmatrix} A_{++} \\ A_{+-} \\ A_{--} \\ A_{--} \end{bmatrix} \tag{3.5}$$

thus, the matrix product

$$\mathbf{S\Psi} = A_{++}\mathrm{CP}_{++} + A_{+-}\mathrm{CP}_{+-} + A_{-+}\mathrm{CP}_{-+} + A_{--}\mathrm{CP}_{--} \tag{3.6}$$

is the superposition of the modes and their respective amplitudes, which include relative phases.

The coupling matrix

$$\mathbf{M} = \begin{bmatrix} -\delta\beta & -i\epsilon_p & -i\epsilon_s & -i\epsilon_c \\ i\epsilon_p & \delta\beta & -i\epsilon_c & -i\epsilon_s \\ i\epsilon_s & i\epsilon_c & \delta\beta & -i\epsilon_p \\ i\epsilon_c & i\epsilon_s & i\epsilon_p & -\delta\beta \end{bmatrix} \tag{3.7}$$

where ϵ_p is the constant that couples modes with opposite SAM and the same IOAM, ϵ_s is the constant that couples modes with the same SAM and opposite IOAM, and ϵ_c is the constant that couples modes with both IOAM and SAM opposite.

Mode coupling due to anisotropic, but z-independent perturbations to the fiber index profile can be expanded as

$$\Delta n^2(\rho, \phi) = \sum_{p=-\infty}^{\infty} a_p(\rho)e^{ip\phi}, \tag{3.8}$$

where a_p is a coefficient, and p is an IOAM [47, 50]. Coupling between modes 1 and 2 with IOAM ℓ_1 and ℓ_2 depends on the overlap between the transverse fields of the modes and the perturbation

$$\langle F_{\ell_1,m}(\rho)| \Delta n^2(\rho, \phi) |F_{\ell_2,m}\rangle = \sum_{p=-\infty}^{\infty} \langle \psi_{\ell_1}(\rho)| a_p(\rho) |\psi_{\ell_2}(\rho)\rangle \langle e^{i\ell_2\phi}| e^{ip\phi} |e^{i\ell_2\phi}\rangle, \tag{3.9}$$

leading to the selection rule

$$p - (\ell_1 - \ell_2) = 0. \tag{3.10}$$

The coefficients a_p are expected to decrease with increasing p, and trend as $a_p \propto 1/p$ in the fiber used in [47]. Coupling a mode with a particular IOAM to a mode with the opposite sign requires $p = 2|\ell|$. In addition to satisfying $p = 2|\ell|$, ϵ_c must flip SAM, so we expect the coupling constant magnitudes to satisfy the ordering $|\epsilon_p| > |\epsilon_s| > |\epsilon_c|$.

Let $\mathbf{U} = \exp[i\mathbf{M}z]$ be a unitary matrix. We assume unitary mode coupling of the form

$$\mathbf{\Psi}_{\text{out}} = \exp[i\mathbf{M}z] \, \mathbf{\Psi}_{\text{in}}, \tag{3.11}$$

where "exp" here is a matrix exponential. This form of coupling neglects losses to radiation modes and coupling to any modes outside of the IOAM=2 mode family. The coupling rate with distance

$$\frac{d\mathbf{\Psi}_{\text{out}}}{dz} = i\mathbf{M}\mathbf{\Psi}_{\text{out}} \tag{3.12}$$

represents z-independent mixing, set by the elements of $\mathbf{M}$ (from whence the name "coupling matrix"). Constant mode coupling with distance does not include stochastic or localized perturbations from defects, which would cause the same behaviors in the output field, but with more complicated spatial variation. Our approach also neglects coupling to backward-propagating modes that reflect energy back out of the input, which we expect to be a good approximation.

$\mathbf{M}$ is Hermitian, so it has real eigenvalues and orthogonal eigenvectors. The eigen-decomposition $\mathbf{M} = \mathbf{N}\mathbf{D}\mathbf{N}^{-1}$ relates $\mathbf{M}$ to a diagonal matrix $\mathbf{D}$ (with entries that are the eigenvalues of $\mathbf{M}$) through a unitary matrix $\mathbf{N}$. $\mathbf{N}$ changes the basis from that of the CP fiber modes to the eigen-basis of the coupling process. Its

columns are eigenvectors composed of the linear combinations of CP fiber modes. These eigenvector combinations are orthogonal to each other, *i.e.* do not mix with propagation. The decomposition of $\mathbf{M}$ also yields the decomposition of $\mathbf{U}$,

$$\mathbf{U} = \exp[i\mathbf{M}z] = \mathbf{N}\exp[i\mathbf{D}z]\mathbf{N}^{-1}. \tag{3.13}$$

Mode coupling behavior can involve intricate combinations of many terms, even within the restricted subspace of modes considered here. Mathematica's abilities to do both symbolic and numeric evaluation are well-suited to investigation of the resulting effects.

3.2.1 Analytic Example: Two-Mode Coupling

Let's illustrate the mode coupling with a simple, analytically tractable example. Taking $\epsilon_s = \epsilon_c = 0$ and $\epsilon_p = \epsilon$ in Eq. 3.7 yields

$$\mathbf{M} = \begin{bmatrix} -\delta\beta & -i\epsilon & 0 & 0 \\ i\epsilon & \delta\beta & 0 & 0 \\ 0 & 0 & \delta\beta & -i\epsilon \\ 0 & 0 & i\epsilon & -\delta\beta \end{bmatrix} \tag{3.14}$$

which models two isolated pairs of coupled modes. We'll focus on one of those pairs in a 2×2 subspace by assuming that the other pair have zero excitation amplitude at the fiber input. Making use of the identities

$$\cosh(ix) = \cos x \tag{3.15}$$

$$\sinh(ix) = i\sin x \tag{3.16}$$

and taking $\gamma = \sqrt{\delta\beta^2 + \epsilon^2}$, the unitary coupling matrix for the subspace (denoted with a tilde) is

$$\tilde{\mathbf{U}} = \begin{bmatrix} \cos(\gamma z) - i\frac{\delta\beta}{\gamma}\sin(\gamma z) & \frac{\epsilon}{\gamma}\sin(\gamma z) \\ -\frac{\epsilon}{\gamma}\sin(\gamma z) & \cos(\gamma z) + i\frac{\delta\beta}{\gamma}\sin(\gamma z) \end{bmatrix}. \tag{3.17}$$

The modal excitation as a function of z is $\tilde{\mathbf{\Psi}}_{\text{out}} = \tilde{\mathbf{U}}\tilde{\mathbf{\Psi}}_{\text{in}}$, and examples are given with equal excitation of the two modes in Fig. 3.17, and for excitation of only one of the two modes in Fig. 3.18. For $\epsilon = 0$, $\gamma = \delta\beta$, as expected, and there is no mode coupling. The undesired coupling population $|A|^2$ goes like $\frac{\epsilon^2}{\delta\beta^2+\epsilon^2}$, so if a single mode is excited at the input, the population for that mode will not go to zero unless $\delta\beta = 0$. In this case of isolated pairs, if ϵ is small compared to $\delta\beta$, then $\mathbf{\Psi}_{\text{in}}$ will be similar to $\mathbf{\Psi}_{\text{out}}$, and the modes are well isolated.
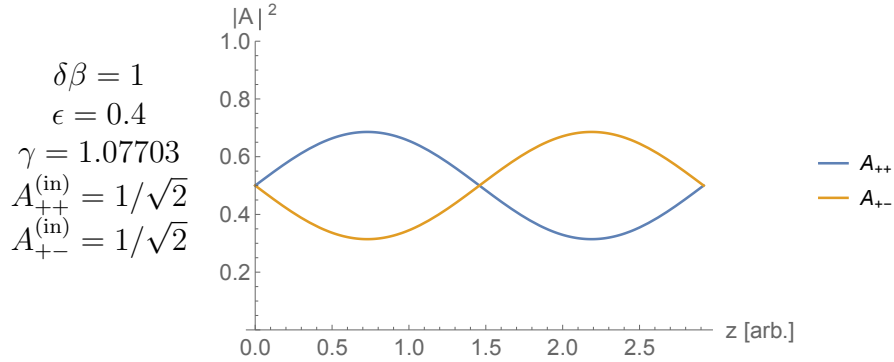
FIGURE 3.17. Evolution of modal population *vs.* z for equal input amplitude of the two coupled modes. Parameters listed on the left.

3.2.2 Numerical Investigation

We now investigate coupling general coupling between the IOAM=2 modes. To visualize the excitation of the fiber modes in $\mathbf{\Psi}$, a 3D plot is preferable, as the
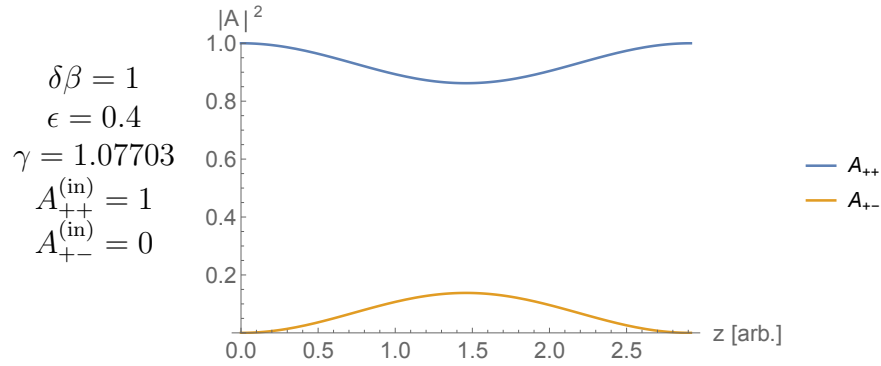
FIGURE 3.18. Evolution of modal population *vs.* z for single-mode input amplitude. Parameters listed on the left.

population of multiple fiber modes tend to coincide in a way that makes it difficult to display them both in 2D. **RunMC1** is an example with $\epsilon_s = \epsilon_p = 0.5$ and is shown in Fig. 3.19.
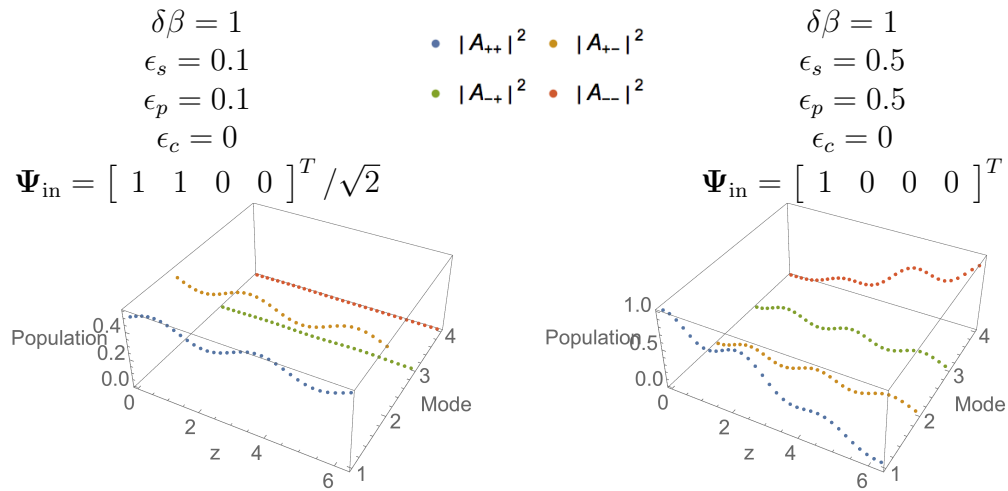
FIGURE 3.19. RunMC1: Example populations $|\mathbf{\Psi}|^2$ *vs.* z.

The goal of this series of simulations is to get a sense of the effects of mode coupling in our experimental runs. To that end, this section uses the experimental value $\delta\beta_e = 22.1°/\text{cm} = 38.5718 \text{ rad/m}$, in agreement with our measurements from the dual-rotation experiment of Sec. 5.6.

Coupling through the ϵ_c term, shown in **RunMC2**, directly couples energy in clover or donut modes with one value of the control property into the mode combination with the opposite value of the control property, as shown in Fig 3.20. This would cause the rotation rate of the rotating quantity to oscillate sinusoidally instead of exhibiting linear behavior. Luckily, perturbations that induce ϵ_c coupling must flip both IOAM and SAM, without flipping direction of propagation, so we expect the magnitude of ϵ_c to be small.
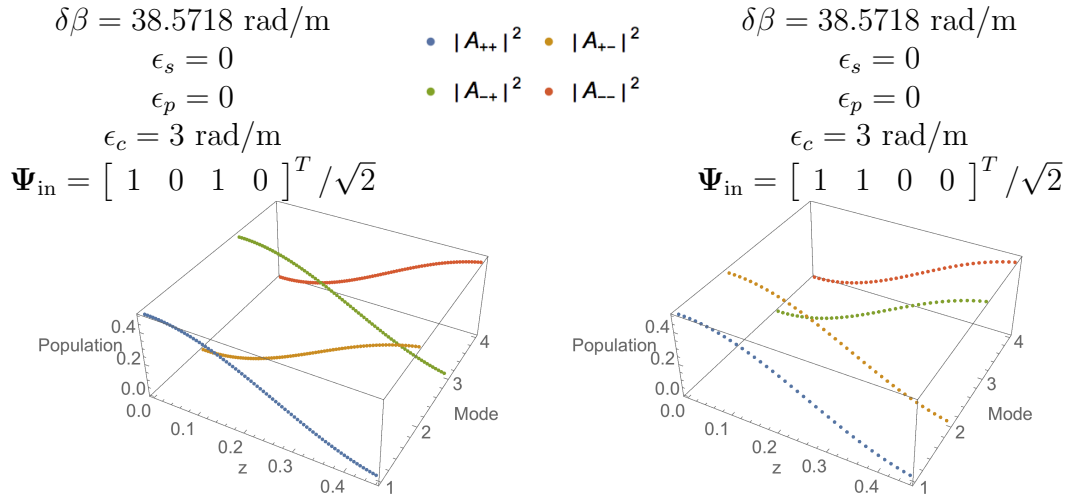
FIGURE 3.20. RunMC2: Populations $|\mathbf{\Psi}|^2$ *vs.* z under ϵ_c coupling. z is in m.

Simulating the effects of the couplings on all desired IOAM=2 inputs for experimental parameters shown in Table 3.4. We now investigate the effects of having just one non-zero ϵ value on all input SOI mode combinations. The effect of $\epsilon_p = 10$ rad/m is investigated in **RunMC3**, with population *vs.* z shown in Fig. 3.21 and both polarization and nodal line orientation shown in Fig. 3.22. Coupling between circular polarizations at a ratio of $\frac{\epsilon_p^2}{\delta\beta^2 + \epsilon_p^2} = 6.3\%$ causes: a minor undesired population imbalance in the input clover mode combinations, a greater population imbalance for the input donut mode combinations, minor oscillation in θ for all mode combinations,

oscillations of the clover DOP but not the donut DOP, and results in minor variation in the slope $\frac{\mathrm{d}\phi}{\mathrm{d}z}$.

TABLE 3.4 Fiber parameters used in the toy model mode coupling simulation.

Description	Property	Value
Shortest (Ending) Fiber Length	L_f	0.34 m
Longest (Starting) Fiber Length	L_0	0.46 m
SOI Splitting	$\delta\beta_e$	22.1°/cm
LCP Clover	$\boldsymbol{\Psi}_{\mathrm{in}}^{\mathrm{c}+}$	$\begin{bmatrix} 1 & 0 & 1 & 0 \end{bmatrix}^T/\sqrt{2}$
RCP Clover	$\boldsymbol{\Psi}_{\mathrm{in}}^{\mathrm{c}-}$	$\begin{bmatrix} 0 & 1 & 0 & 1 \end{bmatrix}^T/\sqrt{2}$
($\ell = +2$) Donut	$\boldsymbol{\Psi}_{\mathrm{in}}^{\mathrm{d}+}$	$\begin{bmatrix} 1 & 1 & 0 & 0 \end{bmatrix}^T/\sqrt{2}$
($\ell = -2$) Donut	$\boldsymbol{\Psi}_{\mathrm{in}}^{\mathrm{d}-}$	$\begin{bmatrix} 0 & 0 & 1 & 1 \end{bmatrix}^T/\sqrt{2}$

The effects of $\epsilon_s = 10$ rad/m are investigated in **RunMC4**, with population *vs.* z shown in Fig. 3.23 and both polarization and nodal line orientation shown in Fig. 3.24. Coupling between IOAM=+2 and IOAM=-2 at a ratio of $\frac{\epsilon_s^2}{\delta\beta^2+\epsilon_s^2} = 6.3\%$ causes: a minor undesired population imbalance in the input donut mode combinations, a greater population imbalance for the input clover mode combinations, no effects on θ for any mode combination, oscillations of the donut DOP but not the clover DOP, and results in minor variation in the slope $\frac{\mathrm{d}\phi}{\mathrm{d}z}$.

The effects of $\epsilon_c = 10$ rad/m is investigated in **RunMC5**, with population *vs.* z shown in Fig. 3.25 and both polarization and nodal line orientation shown in Fig. 3.26. Coupling between modes with the signs of both IOAM and SAM flipped at a ratio of $\frac{\epsilon_s^2}{\delta\beta^2+\epsilon_s^2} = 6.3\%$ causes more disruption than the couplings considered above. Specifically, it causes: gradual reversal of the sign of the control property (*e.g.* an input LCP clover becomes an RCP clover) for all SOI mode combinations, large deviation in θ for clovers but no effect on donut DOP, substantial deviation in both

Legend:
- $|A_{++}|^2$
- $|A_{+-}|^2$
- $|A_{-+}|^2$
- $|A_{--}|^2$

(a) $\boldsymbol{\Psi}_{in}^{c+}$

(b) $\boldsymbol{\Psi}_{in}^{c-}$

(c) $\boldsymbol{\Psi}_{in}^{d+}$

(d) $\boldsymbol{\Psi}_{in}^{d-}$

FIGURE 3.21. RunMC3: Effect of ϵ_p coupling on all IOAM=2 SOI combinations. Number of run points = 21. $\epsilon_p = 10$ rad/m. $\epsilon_s = \epsilon_c = 0$.
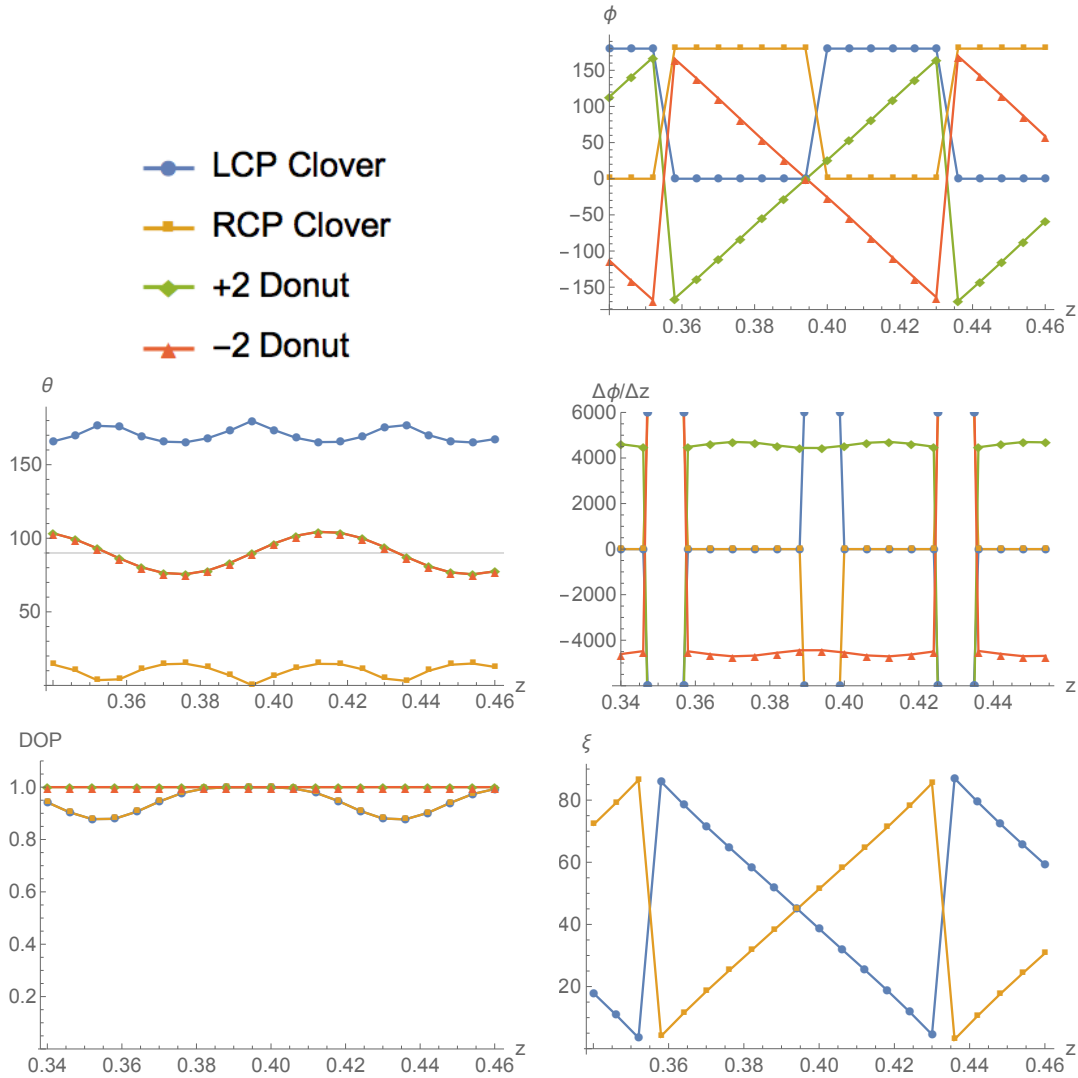
FIGURE 3.22. RunMC3: Polarization and nodal line orientation. Number of run points = 21. $\epsilon_p = 10$ rad/m. $\epsilon_s = \epsilon_c = 0$. In the plot of ξ *vs.* z, the orientation-finding algorithm fails for donut modes, so only clover orientation is shown. Discontinuities in $\frac{d\phi}{dz}$ for donut modes are due to the polarization value looping from one end of the range to the other.
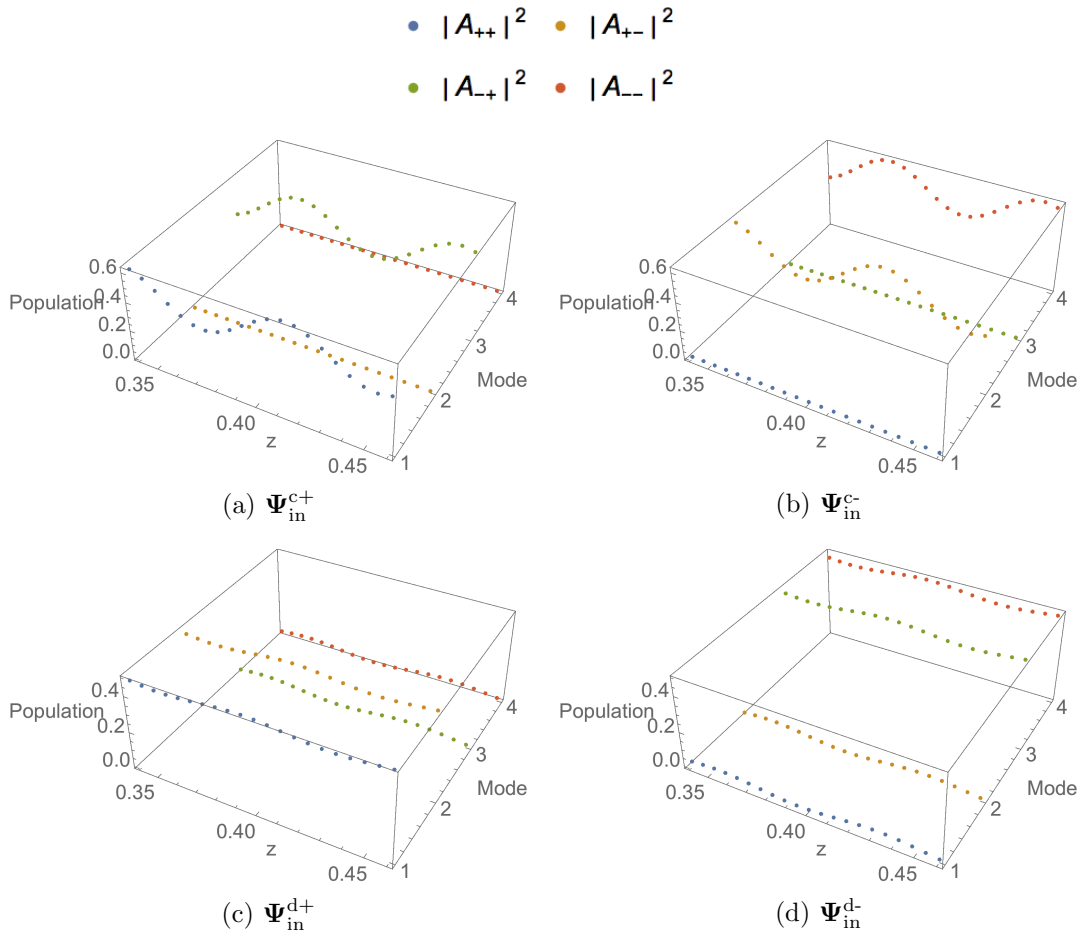
FIGURE 3.23. RunMC4: Effect of ϵ_s coupling on all IOAM=2 SOI combinations. Number of run points = 21. $\epsilon_s = 10$ rad/m. $\epsilon_p = \epsilon_c = 0$.
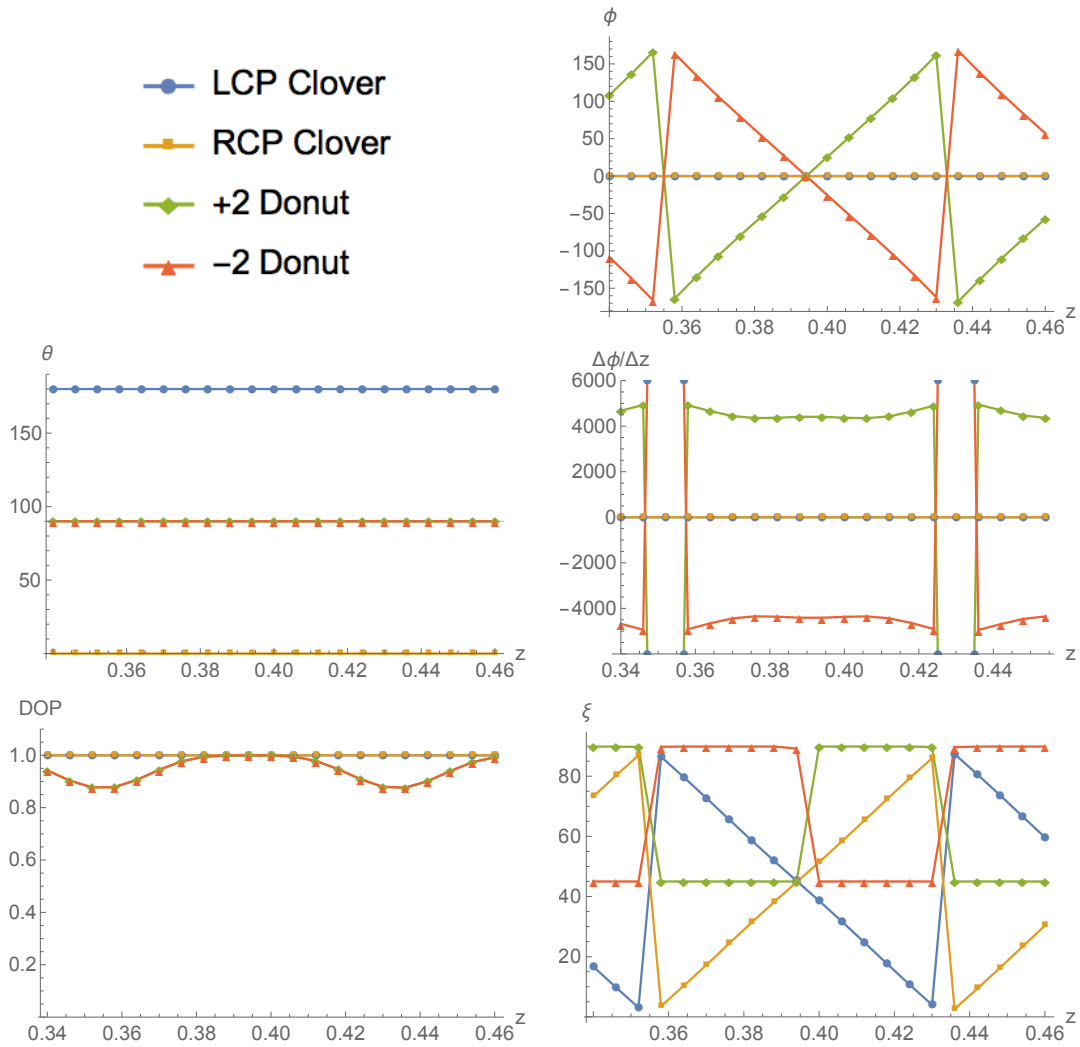
FIGURE 3.24. RunMC4: Polarization and nodal line orientation. Number of run points = 21. $\epsilon_s = 10$ rad/m. $\epsilon_p = \epsilon_c = 0$. In the plot of ξ *vs.* z, the coupling between donut modes causes azimuthal minima to appear, and their orientation are shown for the donut modes. Discontinuities in $\frac{d\phi}{dz}$ for donut modes are due to the polarization looping from one end of the range to the other.

ϕ and ξ *vs. z* for donut modes, large deviations in DOP for both clovers and donuts, and nonuniform slope $\frac{\mathrm{d}\phi}{\mathrm{d}z}$.
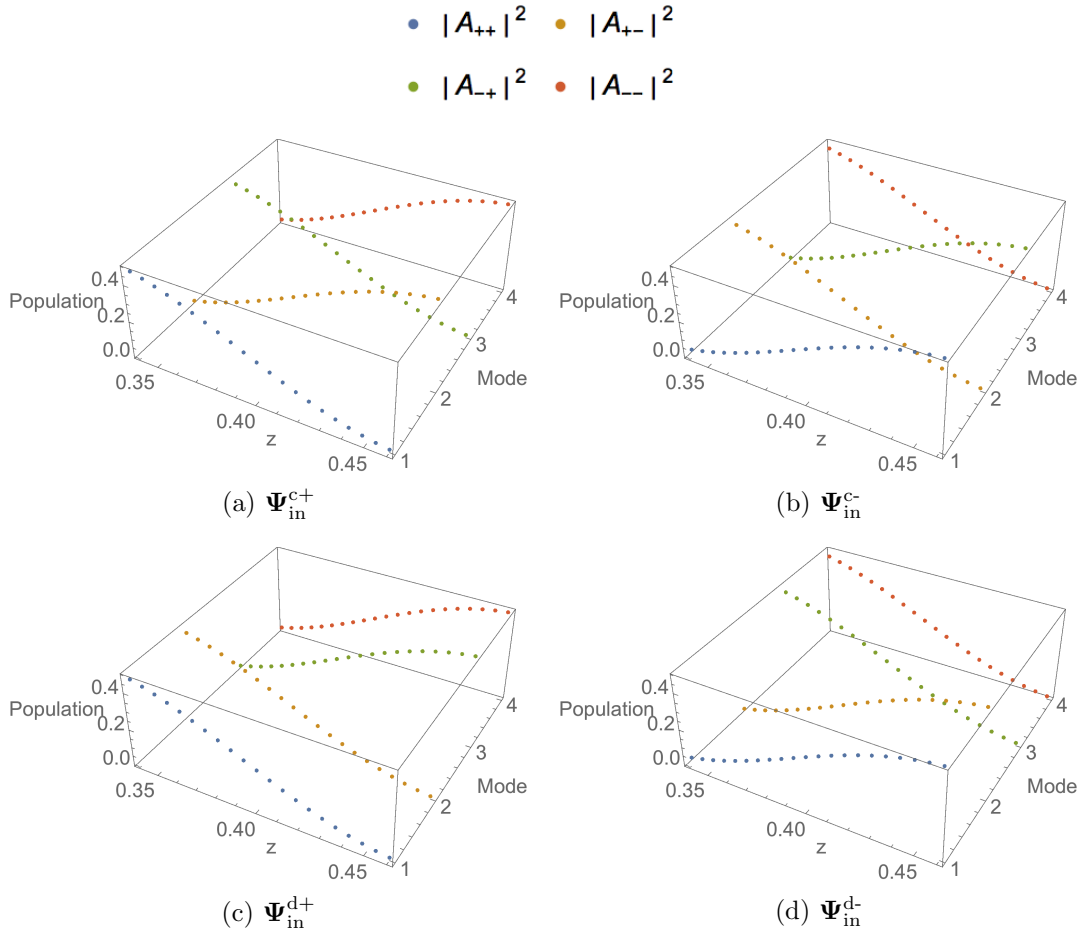
FIGURE 3.25. RunMC5: Effect of ϵ_p coupling on all IOAM=2 SOI combinations. Number of run points = 21. $\epsilon_p = 10$ rad/m. $\epsilon_s = \epsilon_c = 0$.

In order to roughly estimate the magnitude of the couplings that would cause the effects shown in our dual-rotation experimental run (discussed in Sec. 5.6), I varied the parameters and looked to see how well the oscillation amplitudes matched our data. **RunMC6** has the parameter set $\{\epsilon_p, \epsilon_s, \epsilon_c\} = \{8, 5, 0\}$ rad/m with modal excitation *vs. z* shown in Fig. 3.27 and polarization and orientation information shown in Fig. 3.28). The θ and DOP variation in this run have magnitude similar to that observed
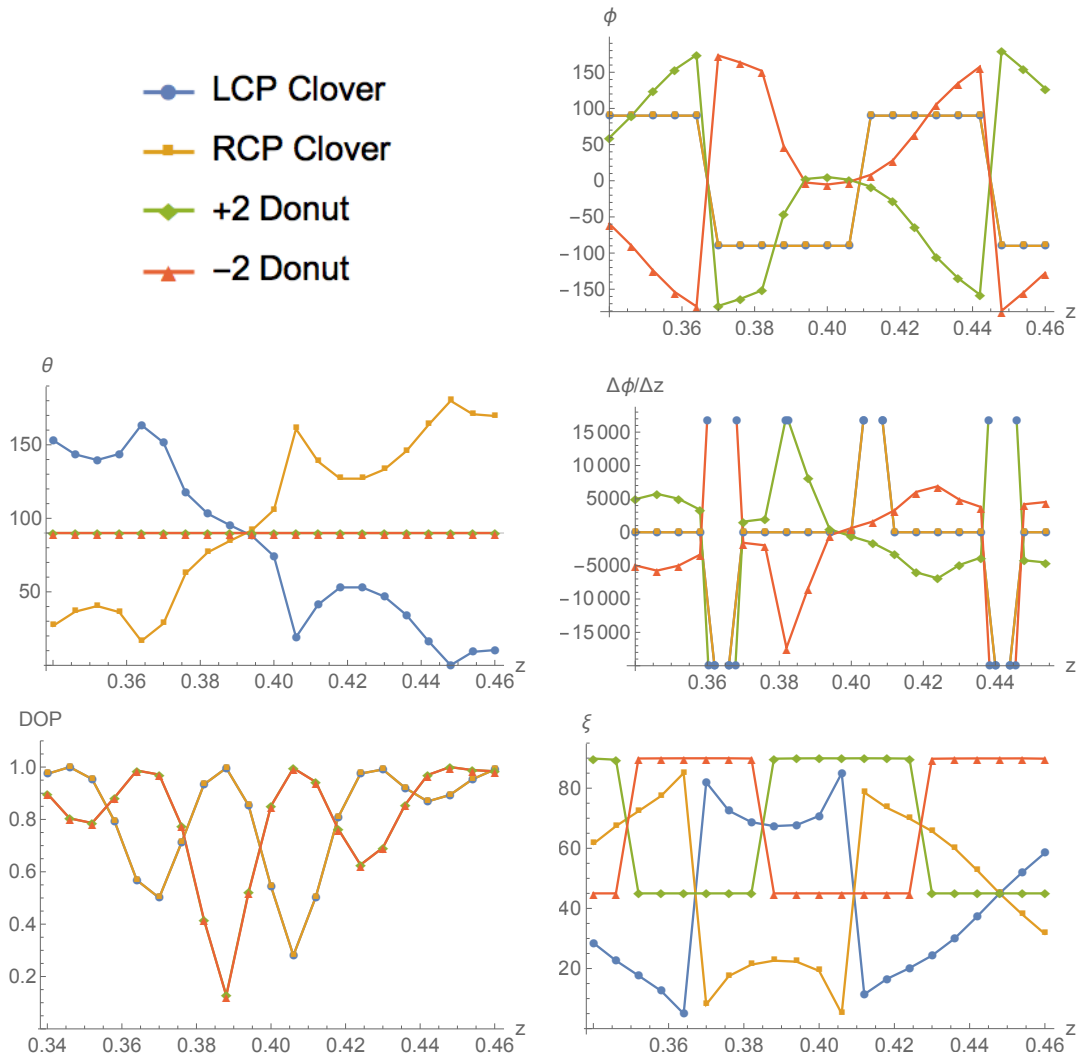
FIGURE 3.26. RunMC5: Polarization and nodal line orientation. Number of run points = 21. $\epsilon_s = 10$ rad/m. $\epsilon_p = \epsilon_c = 0$. In the plot of ξ *vs.* z, the coupling between donut modes causes azimuthal minima to appear, and their orientation are shown for the donut modes. Discontinuities in $\frac{\mathrm{d}\phi}{\mathrm{d}z}$ for donut modes are due to the polarization looping from one end of the range to the other.

68

in the dual-rotation experimental data. Compared to the experimental rotation rate of $\delta\beta = 38.5718$ rad/m, these coupling parameters are small.

(a) $\mathbf{\Psi}_{in}^{c+}$

(b) $\mathbf{\Psi}_{in}^{c-}$

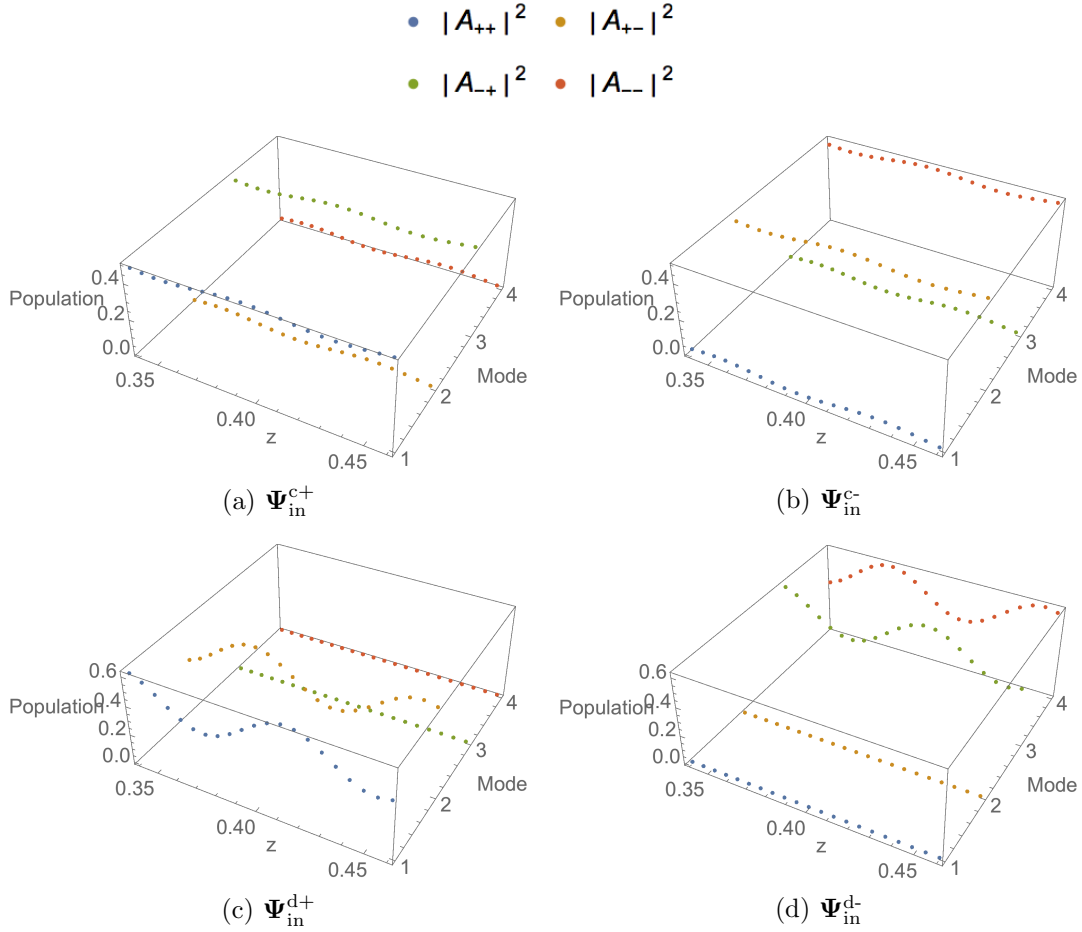(c) $\mathbf{\Psi}_{in}^{d+}$

(d) $\mathbf{\Psi}_{in}^{d-}$
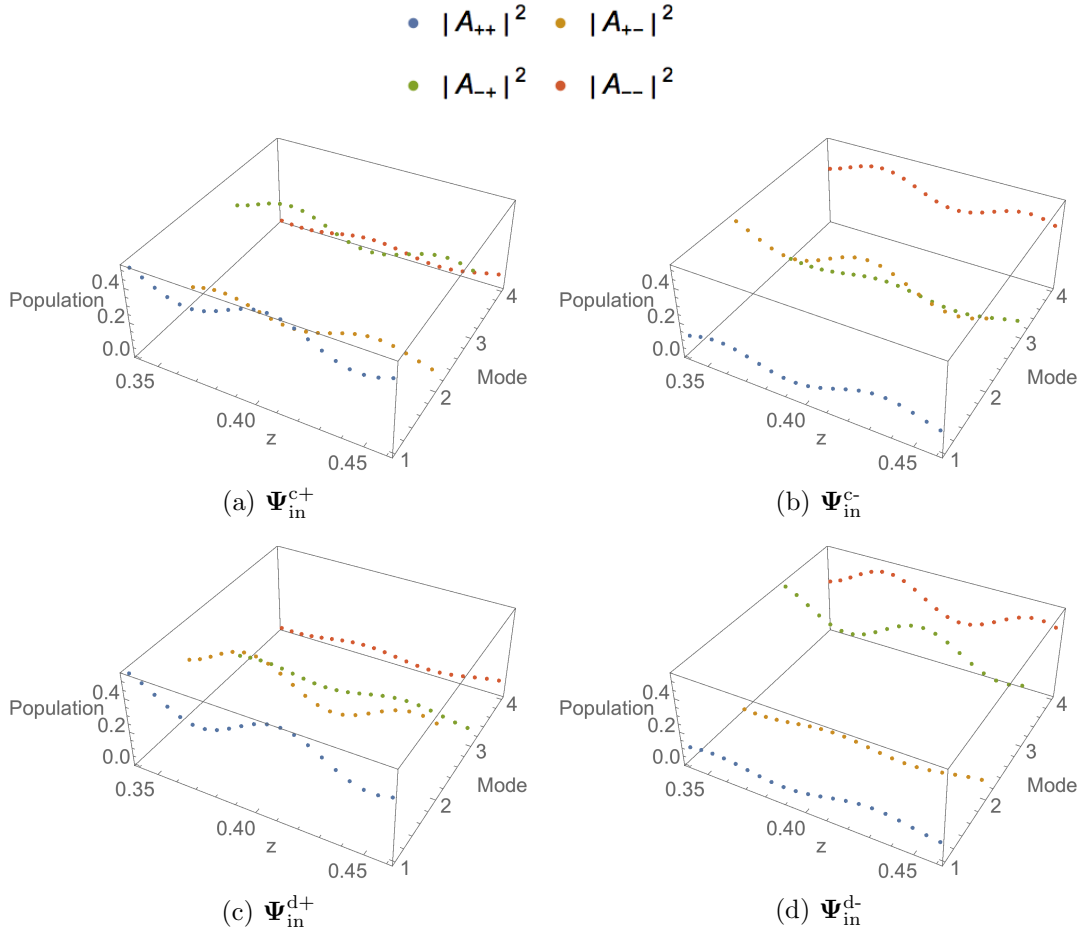
FIGURE 3.27. RunMC6: Effect of ϵ_p coupling on all IOAM=2 SOI combinations. Number of run points = 21. $\epsilon_p = 8$ rad/m. $\epsilon_p = 5$ rad/m. $\epsilon_c = 0$.
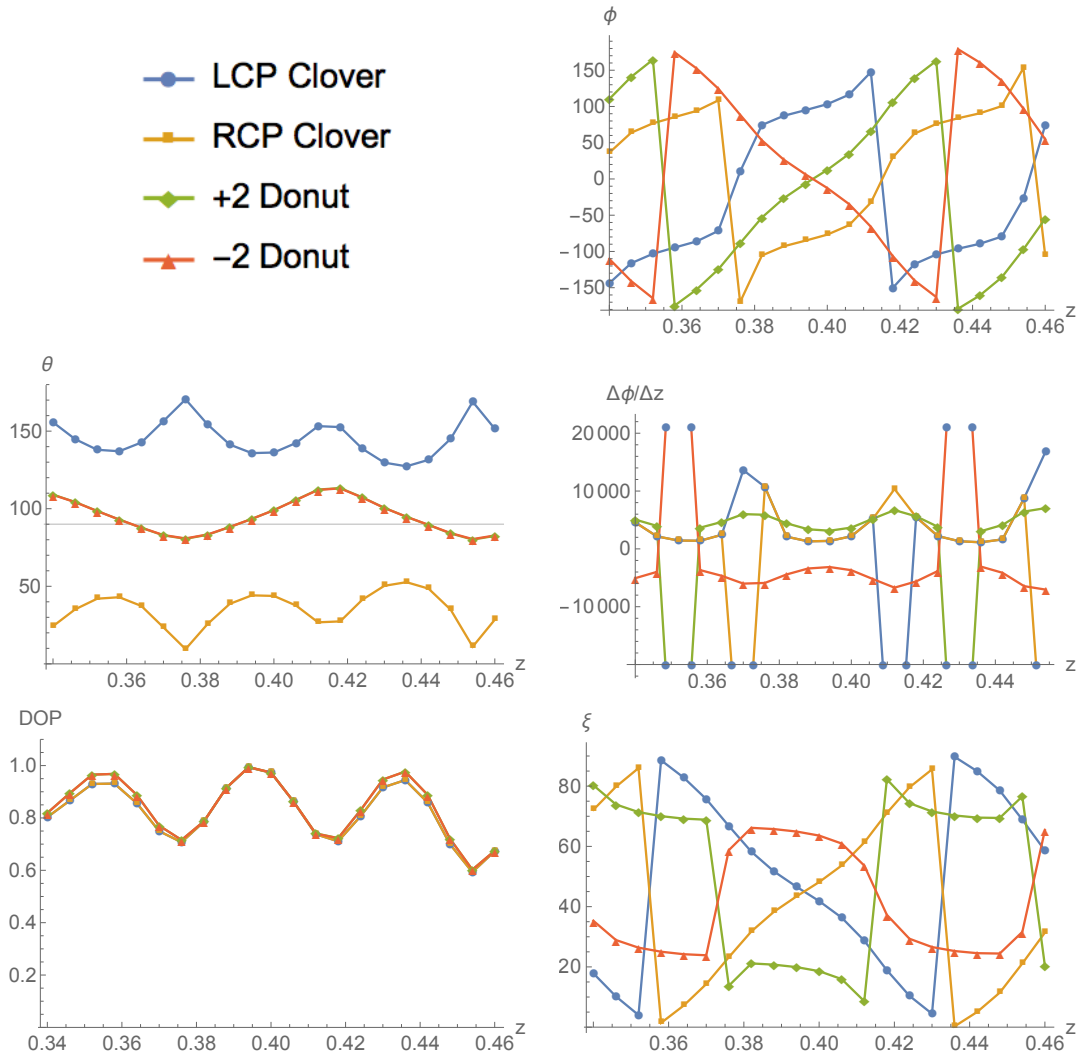
FIGURE 3.28. RunMC6: Roughly a good match to the θ and DOP behavior seen in our dual-rotation experimental run. Number of run points = 21. $\epsilon_p = 8$ rad/m. $\epsilon_p = 5$ rad/m. $\epsilon_c = 0$.

It's possible that the couplings ϵ_j could include phase shifts. The effects of adding phase shifts to the coupling parameters that approximately match dual-rotation experimental observations are summarized in Table 3.5, which accounts for the expected factor of $|\ell| = 2$ between the observed clover rotation rate and the splitting $\delta\beta$ (see Eq. 2.44) in spin-controlled orbital rotation. Best-fit slopes for data measured in that experiment are summarized in Table 5.3. Not all of the slopes in Table 3.5 fall within fit uncertainty range of the experimental measurements of the corresponding rotation. However, taking the mean average of the splittings and the worst-case error [51],[1] gives a splitting range of $\delta\beta = 22.1 \pm 0.7°$/cm, which contains all slopes in Table 3.5. While not a unique fit of the coupling constants, the behavior in RunMC6 is consistent with experimentally observed behaviors, including the magnitude of θ and DOP oscillation (see Fig. 5.17). This supports the hypothesis that mode coupling perturbations that give rise to the experimentally observed oscillations do not give rise to changes in best-fit slopes that exceed the uncertainty we deduce from experimental fits.

TABLE 3.5 Coupling parameters ϵ_j and linear best-fits for the splitting $\delta\beta$ as measured by the slope of 2ξ *vs.* z (corrected with the factor of $|\ell| = 2$) for clovers and polarization ϕ for donuts in configuration space °/cm. Clover is abbreviated 'C', donut is abbreviated 'D', and the $\pm$ sign in the heading denotes the sign of the control property. The slopes without all couplings set to zero is $\delta\beta = \pm 22.1°$/cm.

ϵ_p [rad/m]	ϵ_s [rad/m]	ϵ_c [rad/m]	C+ $\delta\beta$ [°/cm]	C- $\delta\beta$ [°/cm]	D+ $\delta\beta$ [°/cm]	D- $\delta\beta$ [°/cm]
8	5	0	22.7765	-22.7765	-22.2364	22.2364
8	$5\exp\left(\frac{i\pi}{2}\right)$	0	22.1663	-22.5554	-22.2364	22.7367
$8\exp\left(\frac{i\pi}{2}\right)$	5	0	21.8146	-21.8146	-21.5569	22.1305
8	5	1	22.2803	-22.2392	-22.7171	22.7218
8	5	$1\exp\left(\frac{i\pi}{2}\right)$	22.4815	-22.4815	-22.7579	22.7601

---

[1]Worst-case error for the mean splitting is the sum of the uncertainties for all four splittings divided by the number of splittings, $(0.5 + 0.5 + 0.9 + 0.7)/4 = 0.7$.

3.3 Summary

There are multiple beating effects present in a cutback experiment when undesired modes are excited in addition to desired modes. These beating effects can manifest in whole-beam polarization measurements, intensity profiles, and interferograms. Investigating the excitation of undesired modes at the input without mode coupling shows that excitation of all four IOAM=2 modes results in oscillations in the DOP, numerical derivative $\Delta\phi/\Delta z$, and spatial profile distribution. Oscillations in $\Delta\phi/\Delta z$ entail deviations from linear behavior in ϕ *vs. z*. Small imbalances in excitation of the CP modes constituting left- and right-circularly polarized clover combinations result in small oscillations in θ *vs. z*. Excitation of undesired IOAM=1 or IOAM=0 modes (in addition to desired IOAM=2 combinations) result in off-axis phase singularities (corresponding to intensity nulls) that rotate around the z-axis quickly with propagation. They also result in DOP and $\Delta\phi/\Delta z$ oscillation.

Including the consideration of constant unitary mode coupling, we find that coupling between modes with opposite signs of both IOAM and SAM will cause oscillation in the direction of rotation. Combinations of ϵ_s and ϵ_p coupling can cause this indirectly, while ϵ_c coupling causes it directly. Mode coupling of magnitudes similar to $\{\epsilon_p, \epsilon_s, \epsilon_c\} = \{8, 5, 0\}$ rad/m give rise to oscillation behavior similar to that observed in the dual-rotation experiment discussed in Section 5.6. These coupling magnitudes are are small compared to the splitting $\delta\beta = 38.5718$ rad/m, and the resulting oscillations do not change the associate best-fit linear fit slopes by more than the worst-case experimental error.

CHAPTER IV

MODE PREPARATION AND MEASUREMENT

4.1 SLM Holography

A spatial light modulator (SLM) is an array of pixels that serves as a computer-controlled mask that controls some combination of phase and amplitude. SLMs can operate as reflective or transmissive elements and are controlled in the same manner as a computer display. Dileep Reddy set up a system to split video output from a computer to both a standard monitor and the SLM, so we could see exactly what signal was being sent to the SLM and didn't have to bend over the table to look at the SLM display directly (where the displayed patten is visible by eye). We used an HEO1080P from HOLOEYE Photonics, graciously lent to us by Raghuveer Parthasarathy's lab. This model is a reflective SLM that directly alters phase and not amplitude, and has a filling fraction of 87%. The conversion efficiency into the first order was low, even with blazed holograms, but the hundreds of μW it produced were sufficient for our experiments. The pixel values fed to the SLM control a voltage with discretized settings that produces a phase delay. The phase delay as a function of voltage is not strictly linear, so the holograms used in our experiment utilize a restricted range of pixel values (0-245) instead of the full range of values (0-255).

4.1.1 Hologram Design

A simple description of hologram design for converting one transverse spatial distribution to another transverse spatial distribution is to create a superposition of

the input field and the desired field. Illumination of the hologram with the input field creates many diffraction orders on the output, similar to a diffraction grating.

While developing our holograms, I started with phase-only holograms and a short path length, but the profiles I got out in those configurations had many undesired radial features. I talked to Ben McMorran and Jordan Pierce about optimizing hologram design, and Ben passed along a Mathematica document form Sonja Franke-Arnold of the University of Glasgow who has worked on free-space communication using OAM modes [52]. I modified these holograms to tune the prism period (a linear phase ramp that generates an angular offset between the back-reflected zeroth order reflection and the desired first-order reflection in the desired spatial pattern) and added lensing (circularly symmetric phase ramp) to them. The holograms we used are shown in Fig. 4.1, and are designed for a lowest-order Gaussian input spatial profile. The code needed some modification for lensing and to create non-IOAM profiles, like clovers or coffee beans.

Holograms with a phase singularity impart IOAM to all but their zeroth-order outputs. An input beam with IOAM ℓ properly matched to the hologram with singularity charge ℓ' will have a nth-order output diffraction pattern with IOAM $\ell + n\ell'$. n can be any integer. The non-unity filling fraction of the HEO1080P creates a second grating with rectilinear symmetry, which has a broader angular distribution than our desired diffraction orders. We "blazed" our holograms to optimize power into the first-order beam.

Including the amplitude profile of the desired output profile improved the quality of the output spatial mode substantially, even though the HEO1080P is a phase-only SLM and does not directly control amplitude. When optimizing the conversion efficiency and spatial profile, I noticed that changing the hologram would create

74
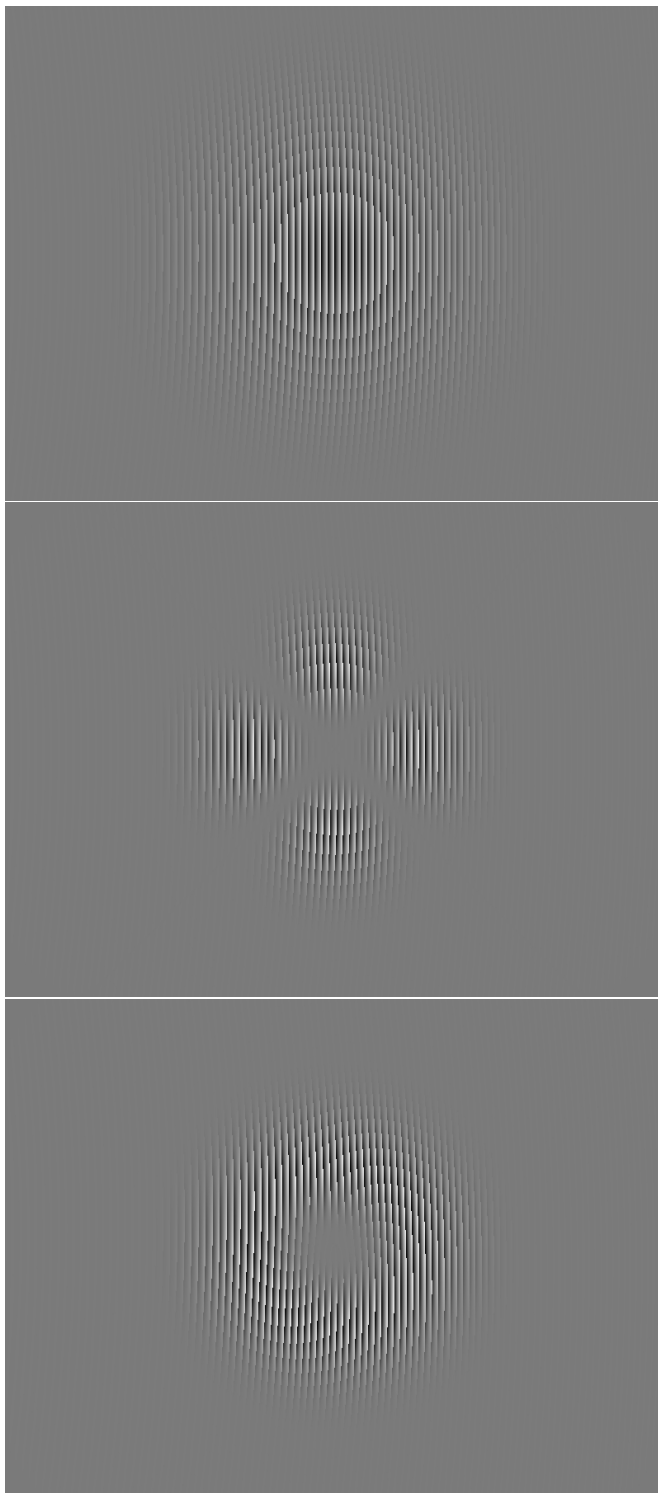
FIGURE 4.1. Holograms for exciting the fiber fundamental, clover combination, and donut (IOAM=2) combination.

deviation in the beam centroid at my fiber input if the input beam was not exactly at normal incidence. The prism period is limited by the physical pixel size, with smaller periods making steeper phase ramps. The angular separation of the first-order beam from the zeroth-order retroreflection is not large and my attempts to tilt the SLM to ease pick-off of the first order introduced this unwanted feature. Correction was simple, though working at normal incidence along with limitations on how large of an angular deviation could be imparted to the first-order output beam necessitated a long beam path for isolation the desired output. Long beam paths are an opportunity for "beam wander" or deviation in the beam centroid at the beam target, *e.g.* the fiber input.

4.1.2 IOAM Verification

We verified the IOAM interferometrically. Interfering the LG profile with a Gaussian beam with a flat phase profile gives a "fork" interferogram. Tuning the mismatch of the k-vectors of the beam from the SLM and reference beam changes the fringe spacing, and bigger fringes sometimes obscure details of the IOAM structure. Specifically, small fringe spacing can show that what looks to be an IOAM=2 singularity is two separated IOAM=1 singularities. Adjusting the collimation of the input beam onto the SLM effects this separation, so adjusting the telescope controlling the input beam collimation was an important tool for controlling the IOAM profile.

To verify the IOAM in a singularity, one must know the direction of the k-vector mismatch, labeled as $\Delta \vec{k}$ and the direction in which more fringes are located, $\vec{f}$, both illustrated in Fig. 4.2.

To identify the IOAM charge:

1. Draw a box around the singularity,
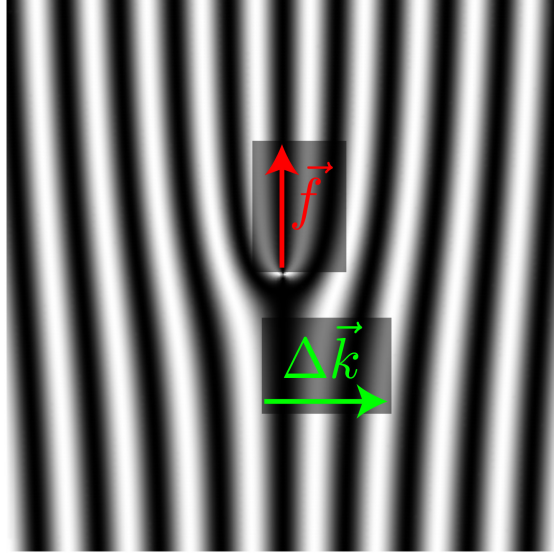
FIGURE 4.2. Reference illustration for identifying IOAM handedness from an IOAM singularity. This singularity has IOAM=+2, which we identify as left-handed, in agreement with our definition of circular polarization where $\sigma = +1$ corresponds to left-circular polarization. $\vec{f}$ points in the direction of more fringes. $\Delta\vec{k}$ points along the direction of the phase gradient, which is set by the k-vector mismatch between the IOAM beam and the reference beam.

2. Choose a starting location and then start traveling in a direction along the box.

3. Count the number of fringes as you travel in one direction as positive and the fringes you count as you travel in the other direction as negative.

4. The sum of the number of fringes is the enclosed IOAM.

While the sign of the sum of the fringes as detailed above can correctly distinguish between the two handednesses, an interferogram alone does not contain sufficient information to identify the handedness μ of the IOAM. The direction of propagation of the reference beam $\vec{k}_{\mathrm{ref}}$ and the IOAM beam $\vec{k}_{\mathrm{IOAM}}$ combined as

$$\Delta\vec{k} = \vec{k}_{\mathrm{ref}} - \vec{k}_{\mathrm{IOAM}}, \tag{4.1}$$

77

in addition to whether the $\vec{k}_{\text{IOAM}}$ directed into or out of the plane of the image, must also be known. Our convention is that if $\Delta\vec{k} \times \vec{f}$ is oriented along $\vec{k}_{\text{IOAM}}$, *i.e.* $\vec{k}_{\text{IOAM}} \cdot \left(\Delta\vec{k} \times \vec{f}\right) > 0$, then $\mu = +1$ (left-handed); $\vec{k}_{\text{IOAM}} \cdot \left(\Delta\vec{k} \times \vec{f}\right) < 0$ indicates $\mu = -1$ (right-handed). This definition of IOAM charge uses the same sense of handedness as we use for polarization.

4.2 Polarimeter

In order to measure polarization, I built a polarimeter from a Wollaston prism, achromatic HWP and QWPs, and a few power measuring devices, shown in Fig. 4.3. Experimental data were collected with two Thorlabs power meters using silicon heads which produce a current proportional to the integrated intensity over their active areas. Polarization measurements were taken with care to ensure that the active area contained the whole beam and averaging over power variation until the standard deviation of the power measurement stabilized. An iteration that gives maps of local polarization information in a beam is described in Section 4.2.1. The
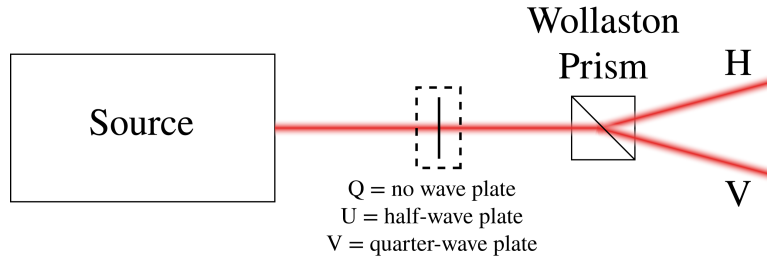
FIGURE 4.3. Polarimeter configuration. Waveplates are slid into and out of the beam to quickly and repeatably change basis.

Stokes parameters describing the polarization state of light are the total intensity and the difference of the intensity of light measured along two orthogonal axes in three

78

different bases,

$$I = \langle |E_H|^2 \rangle + \langle |E_V|^2 \rangle \tag{4.2}$$

$$Q = \langle |E_H|^2 \rangle - \langle |E_V|^2 \rangle \tag{4.3}$$

$$U = \langle |E_D|^2 \rangle - \langle |E_A|^2 \rangle \tag{4.4}$$

$$V = \langle |E_L|^2 \rangle - \langle |E_R|^2 \rangle, \tag{4.5}$$

where H/V indicate horizontal/vertical, D/A indicate diagonal/anti-diagonal, L/R indicate left-/right-circular polarization, and $\langle \rangle$ indicates a time average. These parameters can be calculated for individual locations in a beam's transverse spatial profile (as discussed in the next subsection), but I report values for the whole beam in the next chapter, which is to say the intensities above are integrated over the whole transverse beam distribution. Normalizing $Q, U,$ and V by I using $\tilde{Q} = Q/I$, $\tilde{U} = U/I$ and $\tilde{V} = V/I$, restricts the range of each to $[-1, 1]$, and the resulting parameters give coordinates for polarization within a unit sphere known as the Poincaré sphere, see Fig. 4.4. Position on this sphere can also be parameterized in spherical coordinates with

$$\text{DOP} = \sqrt{\tilde{Q}^2 + \tilde{U}^2 + \tilde{V}^2} \tag{4.6}$$

$$\theta = \tan^{-1}\left(\sqrt{\tilde{Q}^2 + \tilde{U}^2}/\tilde{V} \right) \tag{4.7}$$

$$\phi = \tan^{-1}(\tilde{U}/\tilde{Q}), \tag{4.8}$$

where θ indicates "how circular" the polarization is, while ϕ gives the orientation of the semi-major polarization axis, and the DOP is the length of the polarization vector, indicating the homogeneity of the polarization.
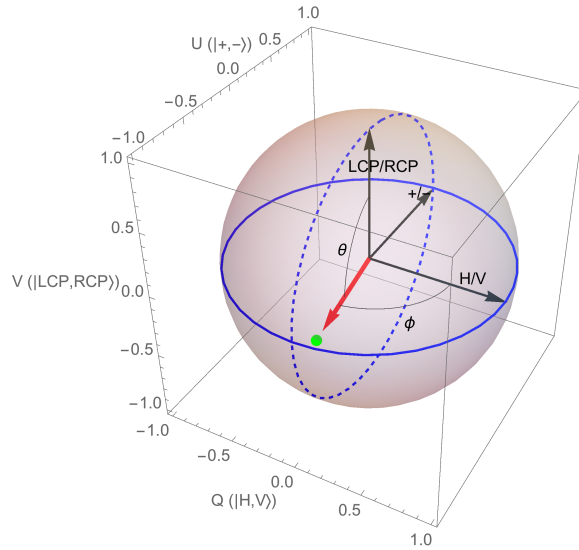
FIGURE 4.4. The polarization Poincaré sphere. A polarization state vector is shown as the red vector. The state with DOP=1 would intersect the sphere at the green point. $Q = +1$ corresponds to horizontal polarization while $Q = -1$ corresponds to vertical polarization, showing that ϕ is related to angles in configuration space by a factor of 2. Each axis is labeled with "A/B" where A is indicated by the axis arrow, and B is antipodal to A on the sphere. Some references use the other circular polarization convention, and LCP and RCP are swapped as a result.

It is unfortunate that there are two opposing historical conventions for circular polarization. I use the convention that circular polarization is represented by the Jones vector

$$\hat{e}_\sigma = \frac{1}{\sqrt{2}} \begin{bmatrix} 1 \\ \sigma i \end{bmatrix} \tag{4.9}$$

where $\sigma = +1$ is left-circular polarization and $\sigma = -1$ is right-circular polarization. This convention is also used by Les Allen [9] and Pedrotti [33]. Many optics textbooks use the other convention, which swaps the LCP and RCP poles, as seen in Born & Wolf [53] and Saleh & Teich [5] which show Poincaré spheres with RCP at the "north" pole where $\theta = 0$.

80

It is possible for the power to vary between measurements of Q, U, and V, but as long as the polarization state is stable in time, the normalized Stoke's parameters should be robust and unaffected.

4.2.1 Stokes Mapper

Using a beam profiler or CCD camera to catch the output beams from the Wollaston prism (see Fig. 4.3) and subtracting properly registered greyscale images gives Stokes parameters for each location in the beam, which I call a Stokes map. This stands in contrast to the whole-beam Stokes measurements described in Eqs. 4.2-4.5, where intensity is integrated over the whole beam before subtraction. Examples of Stokes maps taken as part of the wavelength tuning experiment of Sec. 5.4.2 are shown in Fig. 4.5, and indicate dominantly circular (V-basis) polarization, with some spatially nonuniform and low-intensity structure in the horizontal-vertical (Q) and diagonal/anti-diagonal (U) bases. Beams with spatial distributions of polarization that cover substantial portions of the Poincaré sphere have been a topic of recent interest [54, 55] and controllable excitation of such a beam would be necessary to excite a single fiber hybrid eigenmode (EH/HE).

4.3 Fiber Coupling

Efficient coupling of light into optical fiber relies on good overlap of the input field with the modes of the fiber. For an input mode $\vec{M}_{\text{in}}$ and a fiber eigenmode $\vec{M}_{\text{f}}$ in Cartesian coordinates, both normalized to $\int_{-\infty}^{\infty} \int_{-\infty}^{\infty} \mathrm{d}x \, \mathrm{d}y \, |\vec{M}_j(x,y)|^2 = 1$ with $j \in \{\text{f, in}\}$,

$$\text{overlap} = \int_{-\infty}^{\infty} \int_{-\infty}^{\infty} \mathrm{d}x \, \mathrm{d}y \, \vec{M}_{\text{in}}(x,y) \cdot \vec{M}_{\text{f}}^*(x,y) \tag{4.10}$$

Normalized and Thresholded Stokes Maps
Turn-Around Point Measurement 10/30/2012
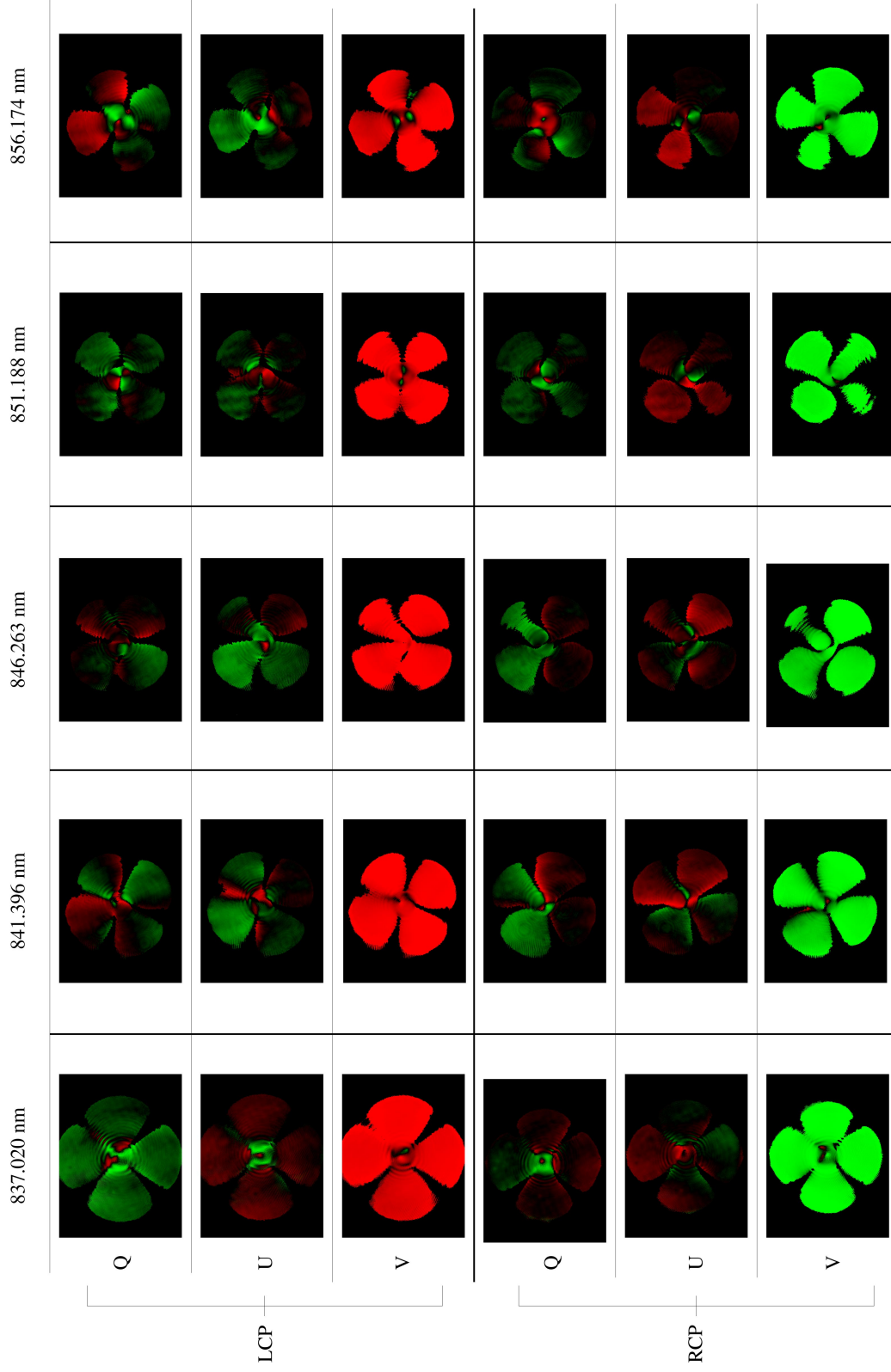
FIGURE 4.5. Stokes maps from turn-around point wavelength tuning measurement experiment. Red pixels indicate positive values and green pixels indicate negative values. Pixel saturation indicates the value of the Stokes parameter at that location. The output coupling objective had insufficient numerical aperture to pass the full output profile, leading to interference fringes. The pixel values have been normalized and the images thresholded (low pixel values are set to zero) to remove noise and improve edge contrast.

Placing the beam focus on the fiber input face creates a flat phase front that maximizes overlap. Fiber modes are not, strictly speaking, Gaussian in that their radial dependence is a Bessel function. Nevertheless, matching the input Gaussian beam waist (which is a radius-like quantity) to half the fiber mode field diameter is a good approximation when working with Hermite-Gauss or Laguerre-Gauss input beams.

Excitation of particular modes in a few-mode fiber is tricky, so we now discuss some practical techniques that are helpful in achieving selective excitation. The alignment is sensitive enough that backlash and coupling between knobs is important to keep track of, even at the levels present in high-quality optomechanics. Coupling light into the output end of the fiber and aligning the input beam with the backward propagating alignment beam is a process that we refer to as "back-coupling." The process I used to excite higher order spatial profiles starts, like so many optical alignment schemes, with a pair of irises; one near the fiber input face, and one far iris that is substantially prior to the near iris along the input beam trajectory. First, align the input beam to the alignment irises. Second, use back coupling and maximize the power going backwards through the fiber. Then, without the input coupler installed, shine the back-coupled light through the iris near the fiber input to center the fiber position, iterating to ensure that the fiber position is still central to the input beam and the tilt is set by the back-coupled light on the near iris. Third, install the input objective and adjust its position and tilt to maximize power in the forward-coupled fundamental. The secondary reflection off of the fiber input face can be very helpful for getting the objective in place and at the right distance from the input face. Similarly, matching the beam parameters of the back-propagating and forward-propagating light in the space between the irises through adjusting the input objective is helpful with

the caveat that it is important to check that the power propagating in each direction is similar, when matching by eye, or properly accounted for. Monitoring the secondary reflection during an experimental run provides a sometimes useful probe for changes in input alignment.

When close to well-coupled, the secondary reflection of the fiber input will show signs of interference, which occurs because some of the light coupled into the fiber is reflected off the output face, and exits the input face to interfere with the light reflected directly off the input face. We assessed this by looking at the interference pattern before and after adding a drop of index-matching fluid to the output end, which affected the interference pattern in the secondary reflection on the input side of the fiber. Furthermore, this interference from the input face is not a concern for the output spatial profiles, as the product of a small reflection coefficient $\mathscr{R}$ and a large transmission coefficient $\mathscr{T}$ for an additional round trip through the fiber goes like $\mathscr{R}^2 \mathscr{T}^2$ with $\mathscr{R}^2$ negligibly small.

Equipped with these tips and tricks, we next review their implementation as part of our experimental measurements of spin-IOAM interaction.

CHAPTER V

EXPERIMENTAL DESIGNS AND RESULTS

5.1 Overview

To observe spin-IOAM interaction in optical fiber, we excite combinations of parallel and anti-parallel modes at the fiber input, record the output profiles at the fiber output, and then reduce the fiber length with a cleaver. We refer to these experiments as "cutback" experiments, and they destroy the fiber segment under test. To avoid rotations due to geometric phase (spin-EOAM interaction) the fiber is made to follow a straight path from input to output, aligned with the trajectory of the input beam. The fiber is mounted on two mounts that are aligned to be straight with the laser. There are two versions of the rotation effect that we probe experimentally, one where the spatial mode stays the same and the linear polarization rotates, and another where the circular polarization stays the same and the clover mode rotates. We began our investigations with observation of the latter rotation, spin-controlled orbital rotation.

5.2 Dispersion-Tailored Fiber

Our first attempts at measuring spin-IOAM interaction took place in standard step-index fiber, but never yielded clean output modes. Designs for sorting the output using a series of parity sorters [56] were underway when Siddharth Ramachandran visited and provided a better way forward in idenfitying our problem as the tendency of modes with IOAM=0 and $m > 1$ to have having similar propagation constants to OAM modes in step-index fiber. Distance between modes in β space is a good

85

indicator of how strongly coupled modes will be by unavoidable random defects in the fiber (see Section 3.2 and [47]).

The Ramachandran lab provided us with two 20 m spools of dispersion-tailored fiber, whose index profile design is intended to isolate the OAM modes from nearby OAM=0 modes [57], guided by the perturbation integrals of Snyder and Love [41]. A scanning electron microscope image of the core structure is shown in Fig. 5.1. We were able to see clean modal excitation over ~ 20 m of this fiber and at our ~ 1 m cutback experiment lengths.

| HV | Mag | WD | Sig | HFW | Spot | Pressure | 5.0μm |
| 15.0 kV | 9198x | 13.9 mm | BSE | 16.22 μm | 4.0 | --- | |
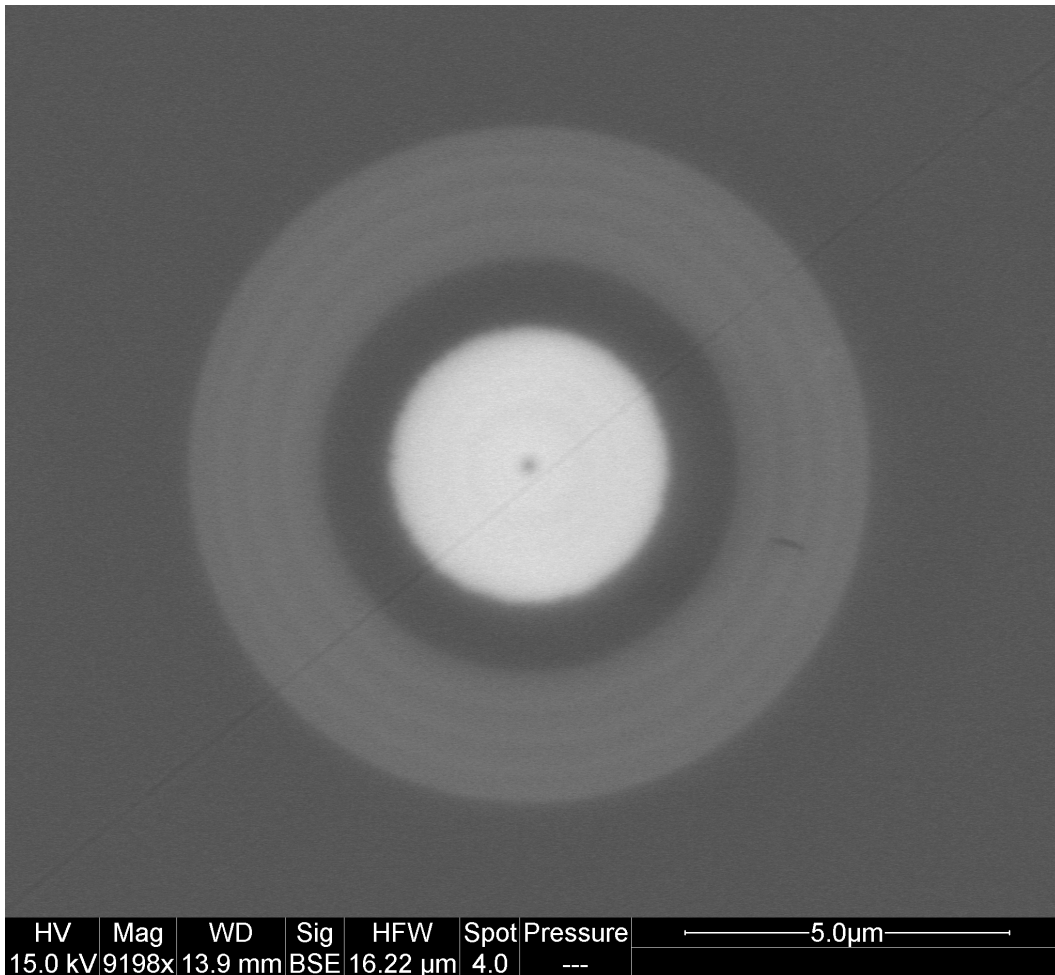
FIGURE 5.1. Scanning electron microscope image of the core structure of the dispersion-tailored fiber used in our experiments.

A complication arising from use of this fiber is that its modes are difficult to solve for. The Ramachandran group has computer code that simulates the exact modes using a finite-element approach to solving Maxwell's equations.

5.3 External Cavity HeNe Experiment

Initial spin-IOAM experiments were performed with an external cavity helium-neon (HeNe) laser, as shown in Fig. 5.2 [58]. Crossed wire, composed of tungsten lightbulb-filament, are placed in the cavity to suppress modes with intensity along the filament orientation. A zoom lens with transverse 2D translation mounts on an optical rail to control longitudinal translation adjusts the input modes to precisely match the fiber modes. Horizontally polarized light enters the QWP, and circularly polarized light that reflects off of the fiber input face becomes vertically polarized and is directed towards the screen by the PBS. This "poor-man's" optical isolator is helpful in precise alignment.
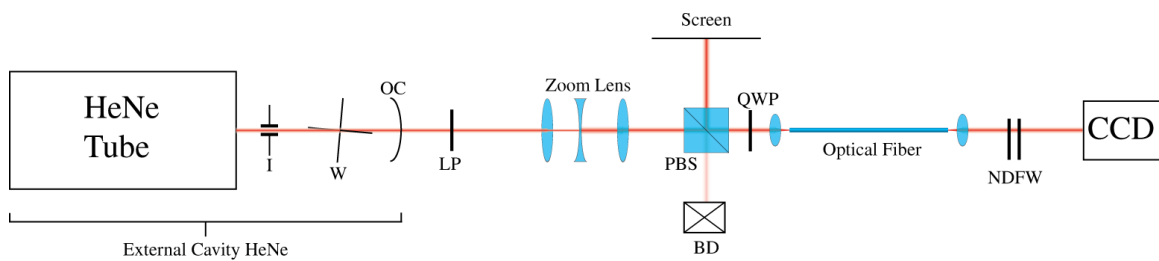
FIGURE 5.2. Diagram of experimental setup as viewed from above. OC = output coupler. W = crossed wires. I = adjustable iris. LP = linear polarizer. PBS = polarizing beam splitter. QWP = quarter-wave plate. NDFW = neutral density filter wheel. CCD = computer controlled CCD camera. The crossed wires and iris in the external cavity HeNE laser allow for selection of the transverse spatial mode of the beam. The linear polarizer is set to horizontal polarization (parallel to the plane of the table). The QWP is set to create left or right circularly polarized light. Figure from [58].

In addition to the cutback experiment, qualitative spin-EOAM coupling was investigated between experimental runs. Taking the output end of the fiber in hand and shining the output mode on an index card, and rotating the output end to about $\pm 90°$ from the original orientation produced no change in the output intensity pattern. Thus, small twists that may occur at the output end of the fiber during cutback and remounting do not affect the rotation of the output profile. In contrast, fixing the output end and changing the path that the fiber takes between the input and the output caused a clear rotation.

The optical fiber was suspended between two Newport 561-FH mounts with a 10" v-groove supporting the fiber in between, as shown in Fig. 5.3. These elements were all aligned straight with the laser path before the fiber was mounted. The v-groove has double-stick tape on the leftmost and rightmost sides, and the pre-stripped fiber is immersed in an optical couplant gel in the v-groove that is index matched to the fiber cladding, to provide a loss mechanism that prevents light from being guided by the air-cladding interface.
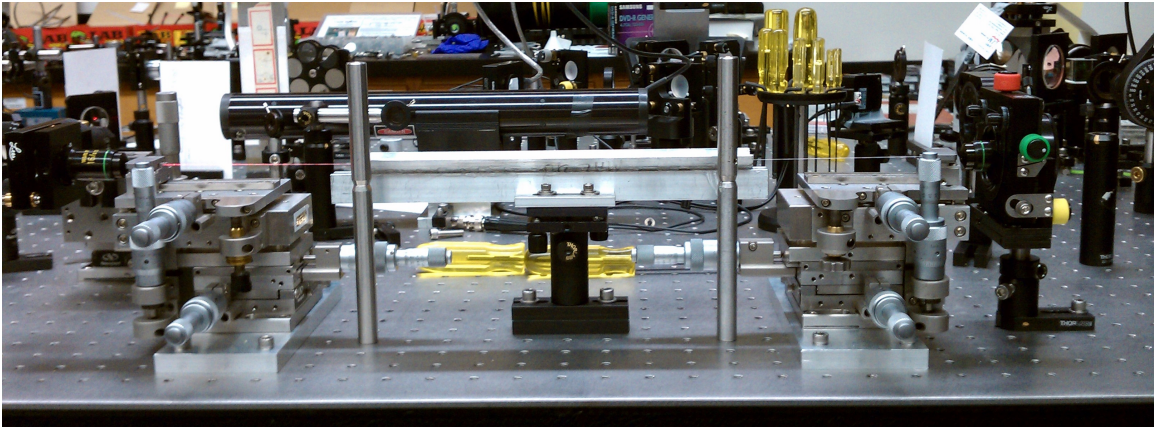
FIGURE 5.3. Photograph of an early version of the experiment using an internal cavity HeNe, showing the fiber input and output mounts, as well as the v-groove used to support the fiber.

The mode coupling was optimized by first translating the wires out of the cavity beam and shining a Gaussian into the fiber to excite the fundamental mode. Once that was cleanly achieved with a high percentage of laser power exiting the fiber, the wires were translated back into place and the input coupling tweaked to optimize coupling of the $HG_{1,1}$ into the fiber to excite the $LP_{2,1}$ mode combinations. The HeNe tube is not stabilized, so the polarization of the light output from the HeNe changes over time. The light incident on the fiber input has stable spatial mode and polarization, but the power transmitted by the linear polarizer varies. The power at the fiber input was measured to vary between $115 - 150$ μW while the power at the fiber output spanned $51 - 72$ μW. Thus, the ratio of the average powers is $\bar{P}_{out}/\bar{P}_{in} = 46\%$. To control for input coupling rotation effects, the alignment controls were not adjusted after their original calibration at the beginning of a data collection run. The only element prior to the fiber input to be adjusted during a run was the QWP, which was rotated to switch polarization handedness.

The fiber length was measured with a tape measure and was shortened on the output side with a Fujikura high-precision CT-30 fiber cleaver, designed to ensure that the cleaving process left flat optical surfaces at the fiber ends. The segments removed from the output were ~1.2 cm long, which is the minimum length for which the cleaver has a good hold on both sides of the cleave location. The segments were measured with a ruler to confirm the distance change, and kept on index cards with double-stick tape in case future characterization or length measurement checks were necessary.

The generated $HG_{1,1}$ input profile (shown in Fig. 5.4) has good overlap with the desired $LP_{2,1}$ fiber mode, though the presence of interference-fringe-containing lobes

in the output profiles in Table 5.1 indicates that the $LP_{2,2}$ mode had some excitation, and tracked the orientation of the central $LP_{2,1}$ lobes.

Output profile orientations ξ for all lengths are measured "by eye" in software by rotating a crosshair to coincide with the nodal lines of the output profile. In this run, I asked peers to replicate my measurements in order to assess the uncertainty of this method[1], and found the deviation to be $2°$. The average of these results are shown in Fig. 5.5. The angles in this run do not change by more than a full range of $90°$,[2] so there is no need for adding offsets before fitting. The linear best-fit model for LCP is

Order of Term	Coefficient	Standard Error
1	185.076	0.976433
x	-3.04636	0.0182138

with coefficient of determination $R^2 = 0.999357$, and for RCP it is

Order of Term	Coefficient	Standard Error
1	-172.191	1.49641
x	2.85093	0.0279132

with $R^2 = 0.998277$, supporting highly linear behavior.

The difference in rotation rates exceeds the fit errors, which do not include the uncertainties in L and ξ. As an estimate of the slope uncertainties, I perturbed each data point in software with a random offset in L normally distributed with a standard deviation of 2 mm, and a random offset in ξ normally distributed with a

---

[1]Thanks to Roger Smith, Kyle Klarup, Jeremy Thorn, Erin Mondloch, and Paul Martin for the replication.

[2]The full range of the spatial mode rotation is $180°$ because of the alternating phases on the lobes, but without a stable and known phase reference, the phase information in unavailable and the rotation is ambiguous after $90°$.
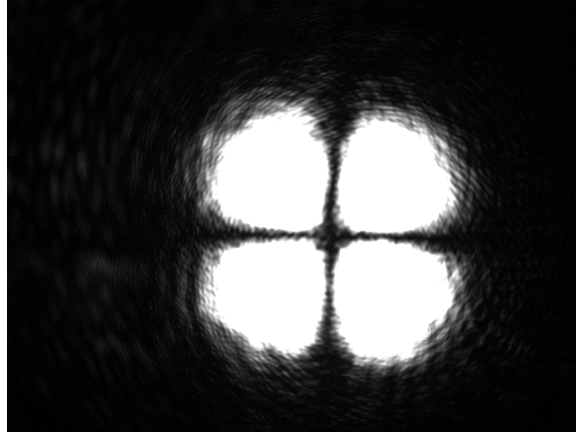
FIGURE 5.4. Input HG$_{1,1}$ profile for HeNe cutback experiment.

62.3 cm	57.5 cm	52.6 cm	47.8 cm	42.2 cm

RCP

LCP
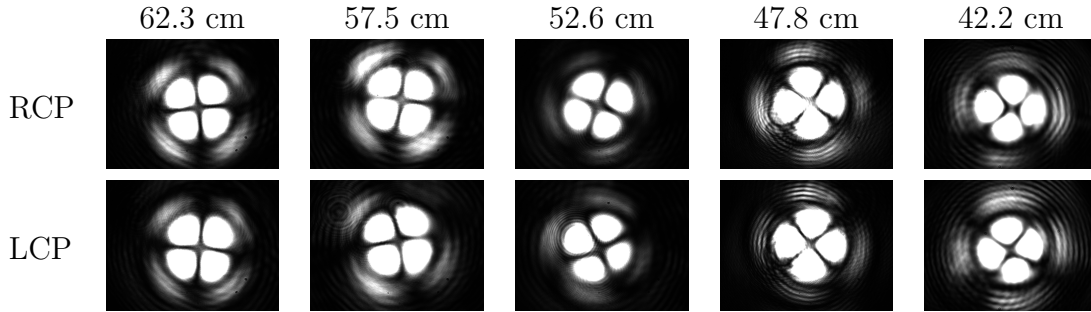
TABLE 5.1 Pictures of a representative subset of the recorded output modes illustrating the rotation. Error bars are present and comparable to the point size. Figure from [58].

standard deviation of 2°. Repeating this over 3000 trials, the standard deviation of the resulting slopes stabilized to $\sigma = 0.07°/\text{cm}$, which does not bridge the gap of between the means of the slopes of $0.15°/\text{cm}$. Thus, the slopes measured in this experiment are distinguishable by a small but statistically significant margin, which is consistent with a small amount of circular birefringence in this segment of fiber (from fabrication or systematically induced in its mounting).

Using these least-squares fits, the y-intercepts of the data from Fig. 5.5 can be used to find the number of 90° rotations consistent with constant rotation from the input orientation angle, $\xi_0 = 2.25°$ for both LCP and RCP input clover
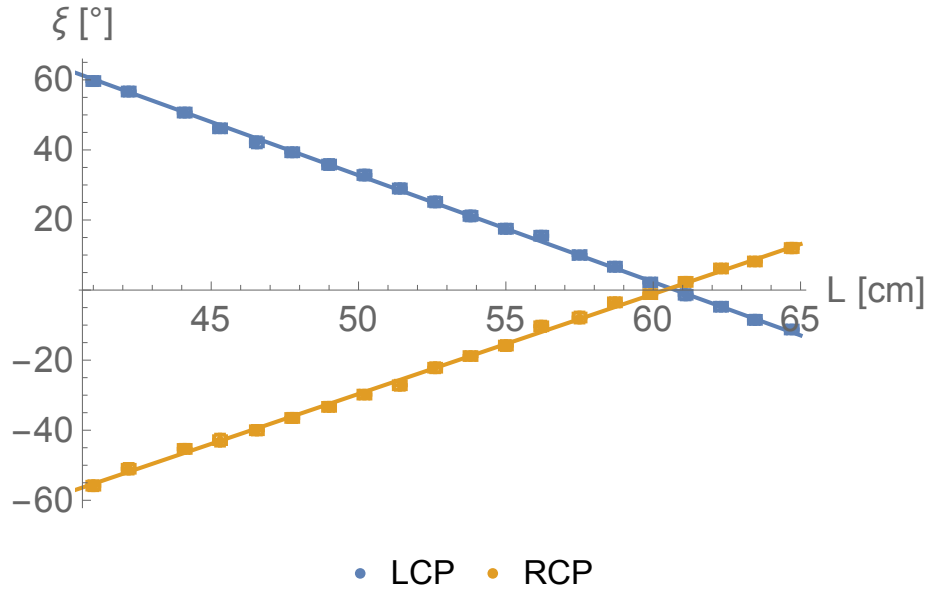
FIGURE 5.5. Raw angles for mode rotation in degrees vs. fiber length. The points are measured data and the lines are the best-fit lines for those data. Error bars a present, but too small to be clear.

profiles. Adding the input orientation and including the offsets, reconstruction of the orientation of the spatial profile through the fiber is shown in Fig. 5.6.

The linear best-fit coefficients from Mathematica for LCP are

Order of Term	Coefficient	Standard Error
1	2.11725	0.498983
x	-3.02757	0.00953758

with $R^2 = 0.999811$, and for RCP are

Order of Term	Coefficient	Standard Error
1	2.98196	0.742015
x	2.90454	0.0141829

with $R^2 = 0.999547$.
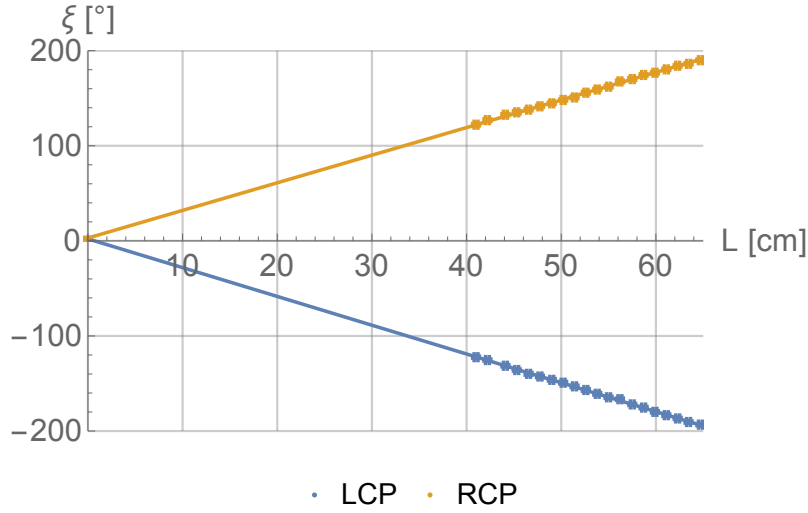
FIGURE 5.6. Mode rotation in degrees vs. fiber length. Best-fit reconstruction of rotation from input to output. The points are measured data and the lines are the best-fit lines for those data. Error bars are present, but too small to be seen.

At $\lambda = 632.8$ nm, $\delta\beta$ is small, which is consistent with the modal intensity being well isolated from the inner interface during propagation. However, the Ramachandran group's simulations at the time of the experiment expected a rotation rate of $340°$/cm. This large disagreement with theory motivated more experimental investigation to test the simulation results and verify that we had observed interaction between light's spin and the intrinsic orbital angular momentum.

5.4 Ti:sapphire Wavelength Tuning Experiment

In order to work closer to the design wavelength of the fiber (~ 830 nm) and explore the wavelength dependence of spin-IOAM interaction, crossed-wires were placed in a wavelength-tunable homebuilt Ti:sapphire laser running in a continuous-wave (CW) configuration to create higher order spatial modes over a broad wavelength range of about 750 - 850 nm. The experimental configuration is shown in Fig. 5.7.
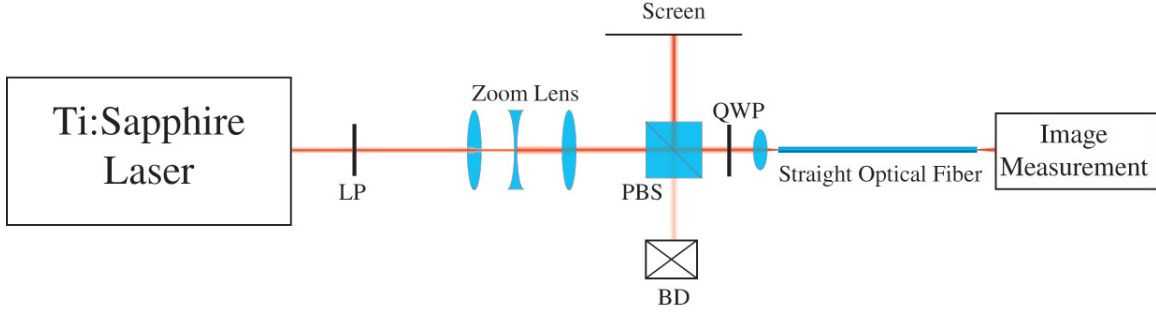
FIGURE 5.7. Experimental apparatus for wavelength-tunable crossed-wire Ti:sapphire Experiments. LP = linear polarizer. PBS = polarizing beamsplitter. BD = beam dump. Image measurement is performed with or without an output coupling objective, to observe far- and near-field images respectively.

To investigate the wavelength dependence of rotation effects, we coupled a clover profile into dispersion-tailored fiber and adjusted the birefringent filter in the laser cavity to tune the wavelength. Etalons in the cavity were necessary for frequency stability during cutback experiments, but were unnecessary and removed for the wavelength tuning runs.

While cutback experiments give information about the relative *phase velocity* of modes, measurements of changes in clover orientation *vs.* wavelength, in a fiber of constant length, give information about the relative *group velocities* of the modes. Group velocity can equivalently be described as a refractive index called the group index [59]

$$n_g = n - \lambda \frac{\mathrm{d}n}{\mathrm{d}\lambda}. \tag{5.1}$$

The change of orientation with wavelength tuning is

$$\frac{\mathrm{d}\xi}{\mathrm{d}\lambda} = \frac{z}{|\ell|} \frac{\mathrm{d}(\delta\beta)}{\mathrm{d}\lambda} = \frac{\pi z}{|\ell|} \frac{\mathrm{d}}{\mathrm{d}\lambda} \left(\frac{\Delta n_{\mathrm{eff}}}{\lambda} \right) = \frac{\pi z}{|\ell|} \left(\frac{1}{\lambda} \frac{\mathrm{d}\Delta n_{\mathrm{eff}}}{\mathrm{d}\lambda} - \frac{\Delta n_{\mathrm{eff}}}{\lambda^2} \right) \tag{5.2}$$

and applying Eq. 5.1 gives

$$\frac{\mathrm{d}\xi}{\mathrm{d}\lambda} = -\frac{\pi z}{\lambda^2 |\ell|} \Delta n_g.$$ (5.3)

5.4.1 Linear Rotation: 755-835 nm

The response of clover orientation to wavelength tuning is shown to be linear over the broad range of 755-835 nm in Fig. 5.8. A 112.2 cm segment of dispersion-tailored fiber was set straight in the v-groove and the birefringent filter was tuned to over a broad wavelength range. These data have been linearized by adding 90° where appropriate. Best-fit linear model coefficients, $\sum_{j=0}^{1} C_j x^j$, for LCP are

Order of Term	Coefficient	Standard Error
1	22647.1	116.477
x	-29.8913	0.148056

and for RCP are

Order of Term	Coefficient	Standard Error
1	$-21534.$	203.415
x	28.5773	0.258285

.

5.4.2 Turn-Around Point

There exist wavelengths where, as the wavelength is tuned in a single direction, the direction of the output clover "turns around" and starts rotating in the opposite direction. These wavelengths are called turn-around points (TAP) and occur where the group indices of modes cross. Clover profile orientation *vs.* λ is shown in Fig. 5.9. These data were taken with a fiber segment of length $L = 88.6$ cm. The fiber
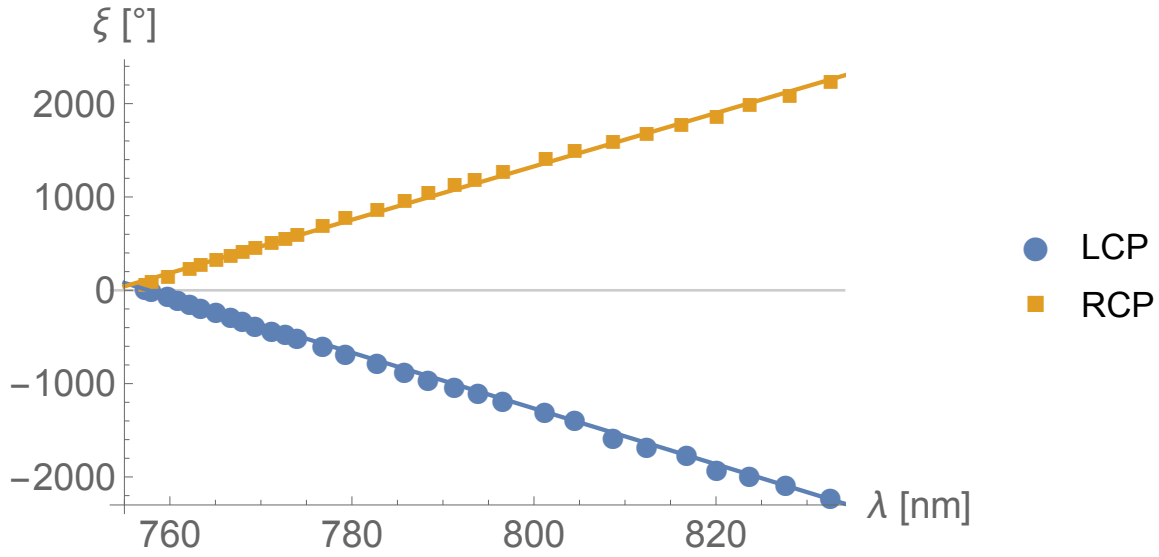
FIGURE 5.8. Orientation of clover nodal-line orientation ξ out of fiber *vs.* λ from 755-835 nm. Points are measured and lines are best-fit linear models.

segment was not the same as used in the previous section. The Stokes maps shown in Fig. 4.5 were taken during this run, and indicate dominantly circular polarization for the output profiles with some spatially non-uniform structure in the Q and U bases that slightly degrade the degree of polarization.

The best fits to a quadratic model $\sum_{j=0}^{2} C_j x^j$ from Mathematica have coefficients for LCP:

x^j	C_j Estimate	Standard Error
1	$-283223.$	7147.9
x	668.179	16.8858
x^2	-0.393965	0.00997214
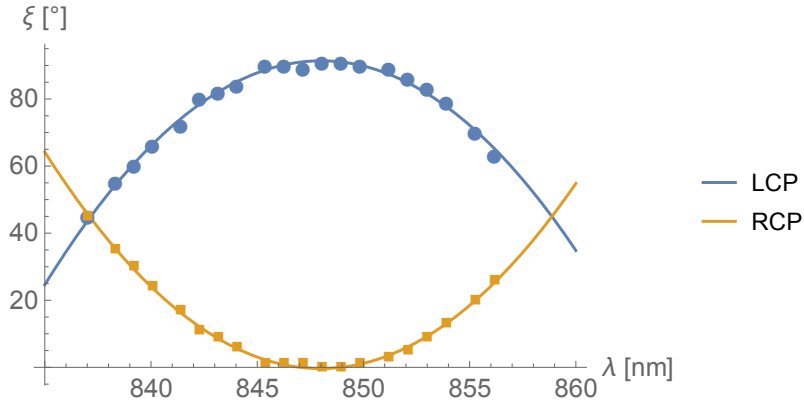
FIGURE 5.9. Measurement of clover nodal-line orientation ξ *vs.* λ to ascertain the turn-around-point for $|\ell| = 2$ modes. Points are measured data, and curves represent the quadratic best fits. The maxima of the LCP fit and the minima of the RCP fit both occur at 848 nm.

and for RCP

x^j	C_j Estimate	Standard Error
1	275110.	3815.12
x	-648.854	9.01262
x^2	0.382584	0.00532253

and those models both have turn-around points at 848.0 nm. The difference in group indices Δn_g calculated using the the best fits of the measured data and Eq. 5.3 are shown in Fig. 5.10.

These data were used in the exact mode simulation done by the Ramachandran group as a figure of merit for validating the simulation results. With this data and interferometric index profile measurements of a sample of our fiber, the simulation was improved and the disparity with the results reduced, as discussed in the next section.
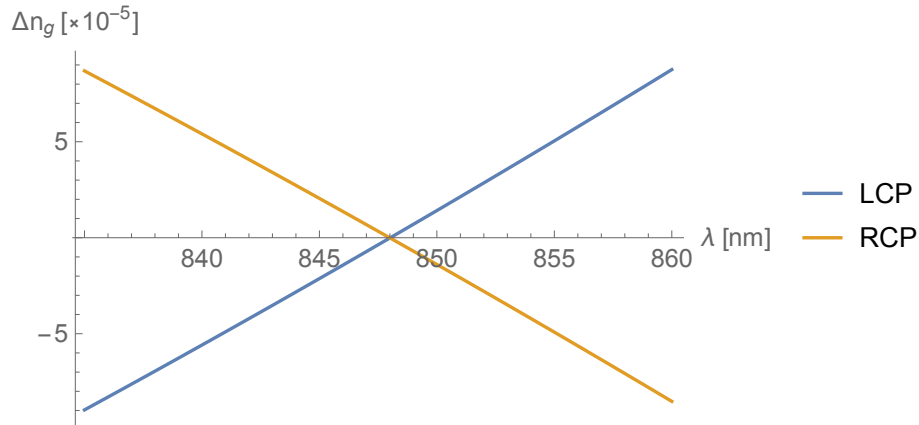
FIGURE 5.10. Best-fit model of group index differences Δn_g between modes coupled by LCP and RCP light. The group index is unitless, and its axis is rescaled by a factor of 10^{-5}. The group index differences go to zero at 848.0 nm.

5.5 Ti:sapphire Spatial Rotation Experiment

Cutback experiments near 800 nm show faster spin-controlled orbital rotation than observed with HeNe laser light.The experimental configuration is the same as for the wavelength tuning experiments, and is shown in Fig. 5.7. The experimental procedure is the same as used in the HeNe experiments. Results of a representative run at $\lambda = 800.5$ nm are shown in this section. A sample of output profiles are shown in Fig. 5.11. The same peers that assisted replicating angle fits with the HeNe data assisted again to fit the Ti:saph run, with similar deviation in angles. The angle measurements, each point the average of each peer's values, as before, are shown in Fig. 5.12. There was enough rotation to require "linearization" of the data by adding integer multiples of 90° to points to bring them into alignment for fitting.
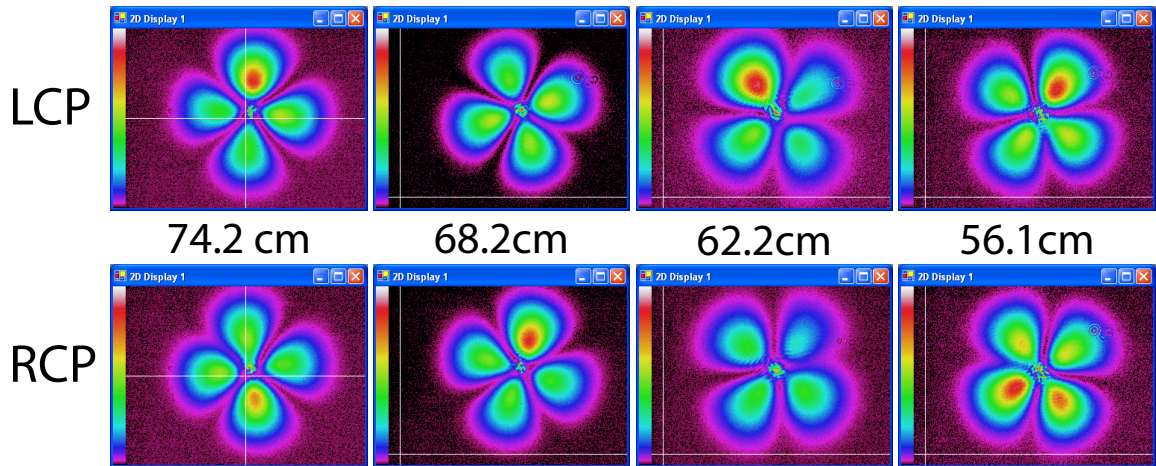
FIGURE 5.11. Representative near-field output clover modes from CW crossed-wire Ti:sapphire laser spin-controlled orbital rotation experiment, with etalons in the cavity for wavelength stability.

The best-fit linear model for the LCP clover rotation is

Order of Term	Coefficient	Standard Error
1	1120.81	9.8274
x	-18.1083	0.1432

with $R^2 = 0.998813$, and the best-fit RCP clover rotation is

Order of Term	Coefficient	Standard Error
1	-1135.13	10.6583
x	18.3377	0.155308

with $R^2 = 0.998639$, supporting highly linear rotation behavior. The rotation rates for the two circular polarizations have the same magnitude to within fit error, indicating no circular birefringence in this fiber segment and the same underlying $\delta\beta$ for both combinations of parallel and anti-parallel modes. The direction of rotation
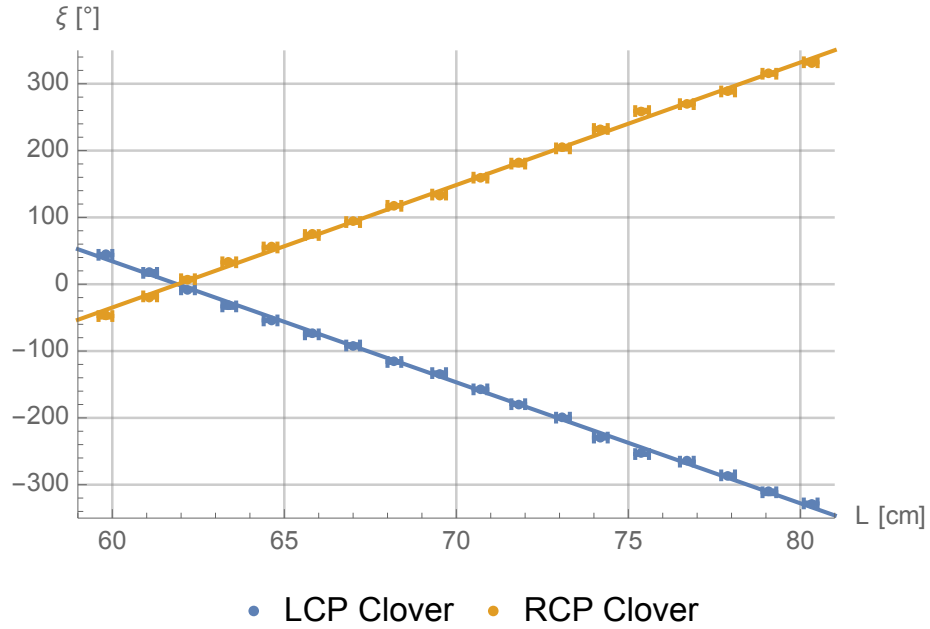
FIGURE 5.12. Angle measurements for CW crossed-wire Ti:sapphire laser spin-controlled orbital rotation experiment at $\lambda = 800.5$ nm.

is controlled by σ, as expected. Adding integer multiples of 90° offsets to the data to bring the best-fit y-intercept as close to the origin as possible, adding the input clover orientation, and refitting yields the orientation ξ *vs.* L data shown in Fig. 5.13.

With the input orientation included, the linear best fit for LCP is

Order of Term	Coefficient	Standard Error
1	7.82564	5.52267
x	-17.6305	0.0823676

with $R^2 = 0.999564$, and the linear best fit for RCP is

Order of Term	Coefficient	Standard Error
1	-10.5735	6.65242
x	17.6921	0.0992172

100
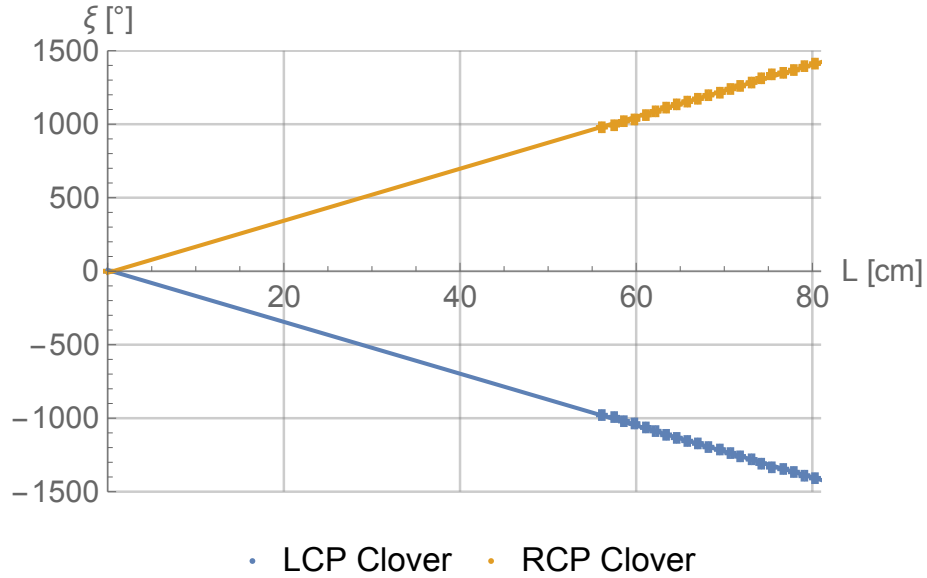
FIGURE 5.13. Best-fit reconstruction of rotation from input to output in CW crossed-wire Ti:sapphire laser spin-controlled orbital rotation experiment at $\lambda = 800.5$ nm.

with $R^2 = 0.999371$. This rotation rate indicates a spin-IOAM splitting of $\delta\beta = 35.4°$/cm, and replicates the expected behaviors both expected from theory and seen in HeNe laser experiments at a different wavelength. At Ti:saph wavelengths, the modes are less confined in the central core and the effect magnitude is larger, as compared to HeNe wavelengths.

The improvement in Ramachandran group's simulation brings the disagreement with observed rotation rates at $\lambda = 800.5$ nm to a factor of ~ 7. The simulation still predicts a rotation rate faster than is observed. This is a substantial improvement from the first simulation run, but we wanted further evidence to maximize our certainty that we have observation of spin-IOAM interaction.

5.6 Dual-Rotation Experiment

Acquisition of an SLM enabled many different spatial patterns to be coupled into the fiber in series without requiring laser cavity tweaks that tend to seriously affect alignment. Initial investigation used Stokes maps, but consistently good spatial uniformity indicated that this was unnecessary, so whole-beam polarization measurements were used. Segment lengths (distances between recorded fiber lengths) were measured with calipers in these runs, for more precise length measurements, but the overall length was measured with a meter stick.

Modes with $|\ell| = 3$ are cut off in this fiber at all wavelengths that we can access with the Ti:Saph (lower bound 750 nm), as predicted from modal simulations and verified experimentally by exciting modes with $|\ell| < 3$. Switching from the fundamental to a clover or $|\ell| = 2$ donut gave output that resembled the input (with expected rotations), but when $|\ell| = 3$ holograms were selected, the mode did not transmit through even a meter of fiber.

Cutback experiments including $|\ell| = 1$ modes were undertaken, and both spatial and polarization evolution were more complicated for $|\ell| = 1$ modes than for $|\ell| = 2$ modes. In addition, $|\ell| = 1$ modes had notably lower DOP at many lengths during these runs. However, these runs took place with a single-mode fiber acting to "clean up" the spatial mode between the laser cavity and the SLM, and the fiber was adding drift to the input light. This fiber was removed, and the drift problems vanished. Due to experimental time constraints, $|\ell| = 1$ mode data were not collected in the run presented in the next section.

5.6.1 Design

To observe both spin-controlled orbital rotation and orbit-controlled spin rotation, five experimental inputs comprise the input mode set, shown in Fig. 5.14. The five input profiles are clovers with left- and right-circular polarization, horizontally polarized $\ell = \pm 2$ modes, and a horizontally polarized Gausisan free-space beam which excites the fundamental fiber mode. The fundamental carries no IOAM and its polarization should propagate through the fiber unchanged to serve as a "control group".
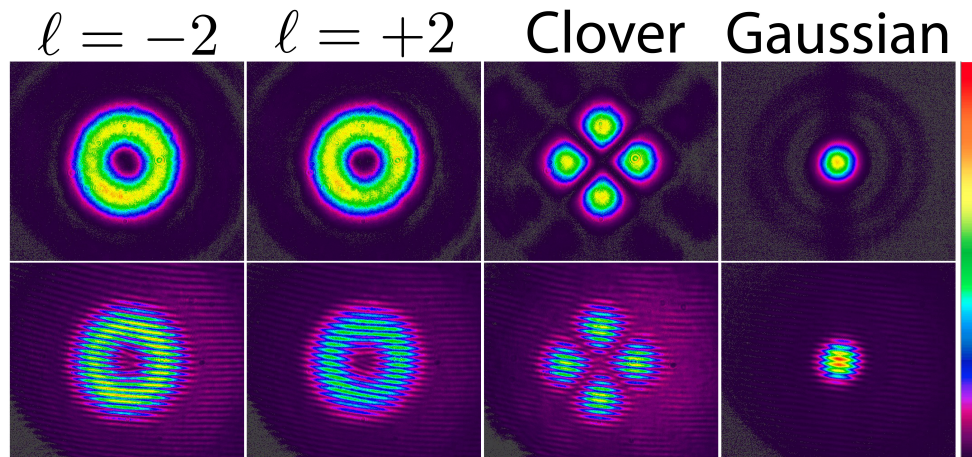
FIGURE 5.14. Input profiles and interferograms. The profiles are generated from holograms for Laguerre-Gauss modes, or linear combinations of them for the clover modes. The lowest order Laguerre-Gauss mode is a standard Gaussian.

The experimental apparatus is shown in Fig 5.15. The input mount has the fiber epoxied into place and the output mount has the fiber resting on double-stick tape. In the dual-rotation run, the fiber holder was closed, as that had no observable effect on the output light. Two tension relief platforms with double-stick tape on the top prevent disruption during cutback from changing the sensitive alignment. Experimental runs that lacked tension reliefs suffered misalignment of the input
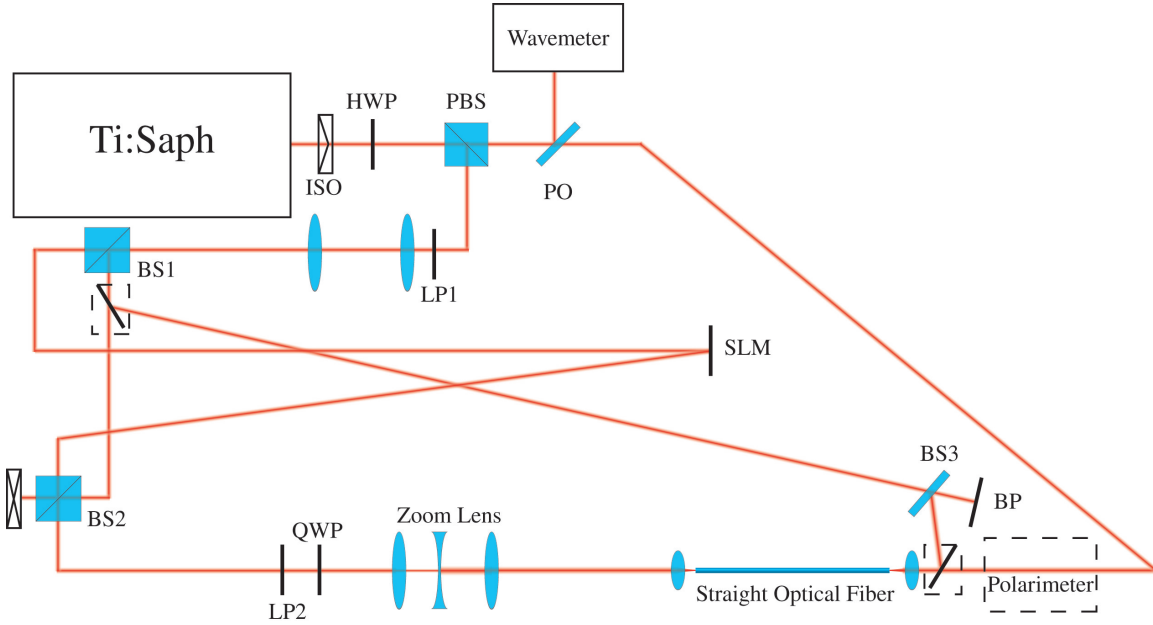
FIGURE 5.15. Diagram of setup used for cutback experiment. Dashed elements "flip" in and out of the beam path during measurements. PBS = polarizing beamsplitter. QWP = quarter-wave plate, which sets light to right- or left-circular polarization. Mirrors are implicit for beam direction changes. Light reflected from the fiber input face is directed to a screen (not shown) to assist with input coupling. The output profile is measured with a beam profiler. BS1 separates the reference beam used for interferometric measurements of the phase structure of the input and output profiles. The reference beam is blocked for non-interferometric measurements.

during cutback. The fiber is stripped of it's jacket before the experiment from the tension reliefs on.

The experiment consists of taking polarization and spatial mode measurements for all the five input beam settings in sequence, and then "cutting back" the fiber, from which these experiments earn the name "cutback experiments." A Fujikura high-precision CT-30 fiber cleaver is used to cut small segments of length ~1.2 cm off the output end of the fiber. The fiber is then pulled straight with as much force as is necessary to straighten the fiber, but not more, to avoid inducing strain. A meter stick positioned on the table to move the output mount along the straight fiber path.

5.6.2 Results

Representative power levels at the fiber input and output are given in Table 5.2. Wavelength is continuously monitored on a Burleigh WA-1500 wavemeter, has an initial value of $\lambda = 799.953$ nm and varies by up to 2 pm over the course of data collection, which is small and output light is observed to have stable polarization and spatial orientation.

TABLE 5.2 Representative input and output powers for each input spatial profile, recorded at the beginning of the experimental run.

Input Profile	Input Power [μW]	Output Power [μW]	Transmission [%]
Fundamental	110	52	47
Clover	54.1	19.3	36
Donut ($\ell = +2$)	162	52	32
Donut ($\ell = -2$)	163	53	33

Polarization properties of the output profiles of are shown in Fig. 5.17. The "by eye" fits of the nodal lines were not replicated by peers in this run, as the averages of peer measurements for previous runs have been consistent with measurements by me only. The output profiles are shown in Fig. 5.16. Mode coupling is evident from the modal profile distortion and the oscillation in θ. The toy model indicates that intermodal coupling is a better explanation for oscillation in θ than excitation of unintended modes at the input, as it better replicates the behavior observed as the length is changed. The DOP dips as low as 0.55 for the IOAM modes, while staying more consistent for the fundamental. Even so, the spatial, ξ, rotations (see Fig. 5.17c) and polarization, ϕ, rotations are linear with fiber length and the slopes (see Table 5.3) differ by the appropriate factor of $|\ell|$ and have sign controlled as expected by the control property. The slopes indicate a common splitting of $\delta\beta = (22.1 \pm 0.7)°/$cm

where the uncertainty is the worst-case of averaging the fit uncertainties together[3], and indicate that, to within error, the anti-parallel modes are degenerate in β and the parallel modes are degenerate in β.
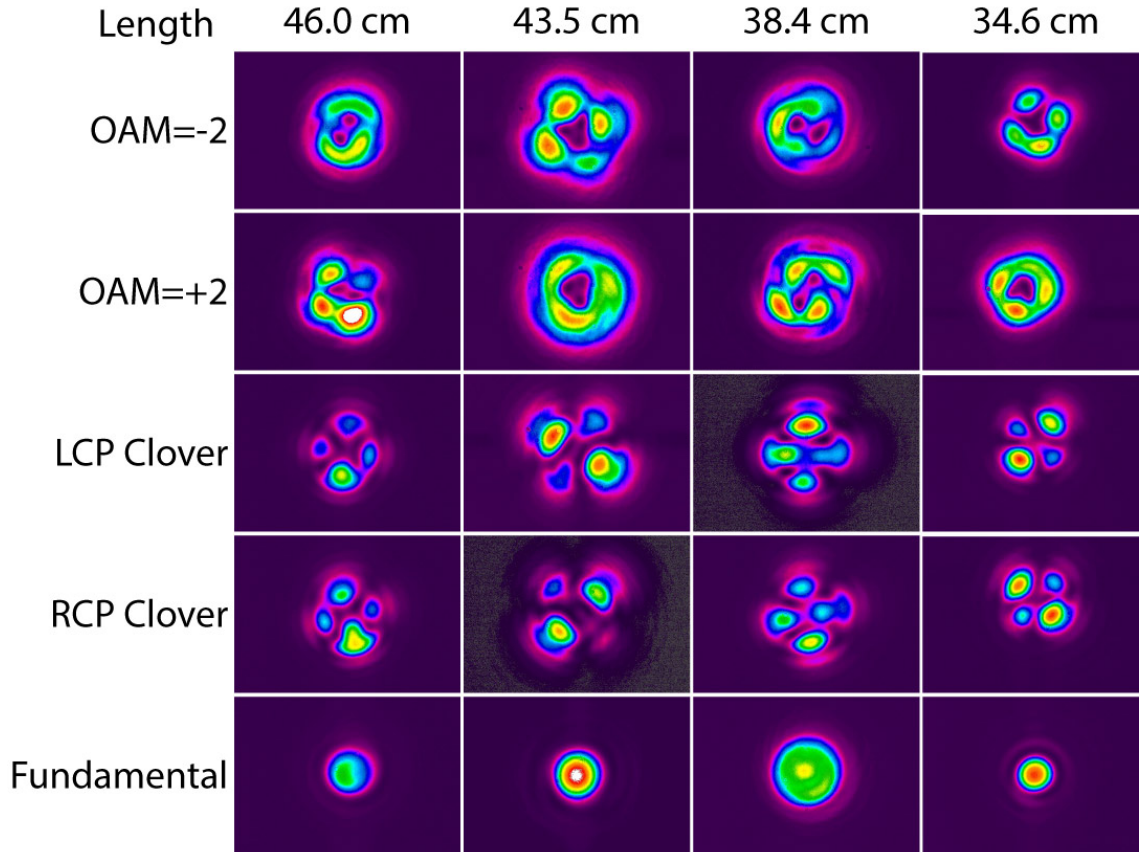
FIGURE 5.16. Output spatial profiles.

These data indicate some mode coupling is taking place, but toy models put the error expected due to mode coupling of the same order as the fit error we measure, as detailed in Section 3.2. Strong mode coupling would result in nonlinear behavior for ξ and ϕ, and no such behavior is observed. The consistency of the independent

---

[3]As opposed to adding the fit uncertainties in quadrature and then dividing by the number of uncertainty values ($N=4$), which gives an error of $0.3°/\mathrm{cm}$. The worst case is given in the main text as it is unclear whether the errors are correlated, which would make the addition in quadrature unsound.
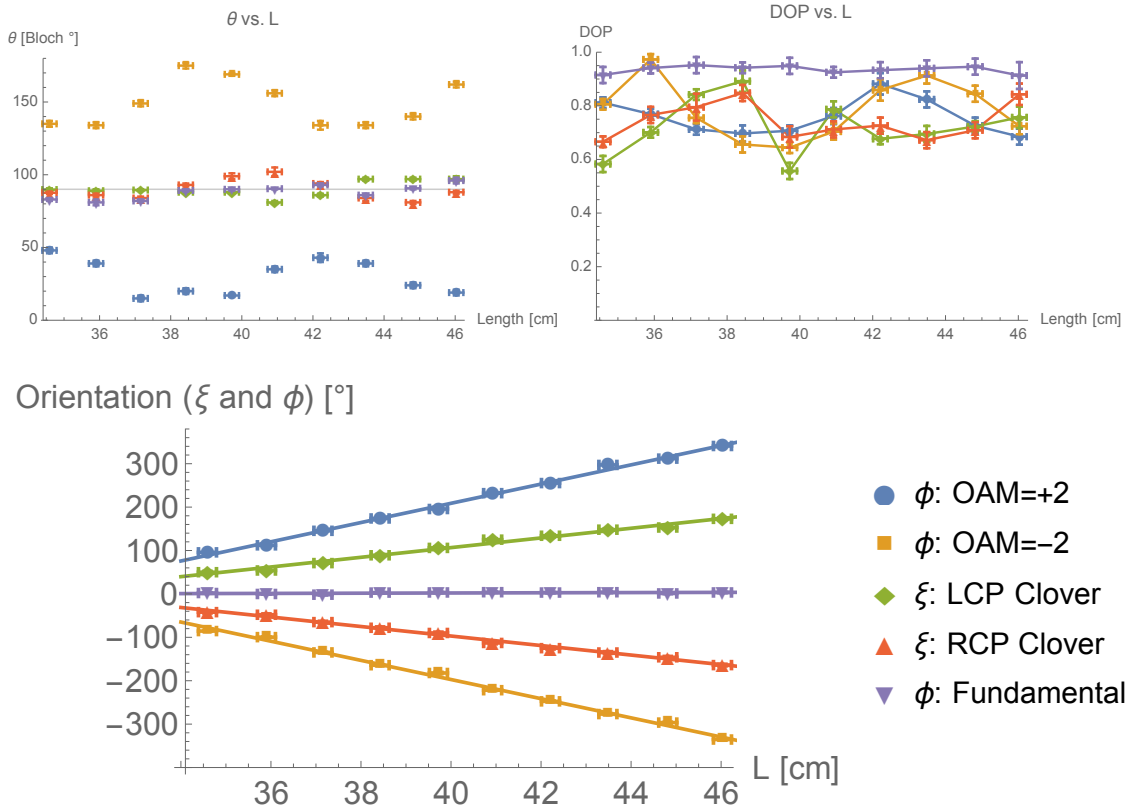
FIGURE 5.17. Measured output parameters for SLM dual-rotation experiment. (a) Polar angle of polarization for all 5 input profiles. Grey line at 90 Bloch ° is an eye-guide for linear polarization. (b) Degree of polarization *vs. L*. Colored lines serve as eye-guides. (c) Comparing the spatial orientation, ξ of the clover profiles to the linear polarization orientations, ϕ, of all other inputs. Best linear fits shown as colored lines. Legend applies to all plots.

TABLE 5.3 Best-fit slopes for the spatial rotation, R_s, and polarization rotation, R_p, shown in Fig. 5.17c. The first column is the sign of the control property, which is plus for LCP and $\ell = +2$; minus for RCP and $\ell = -2$.

	R_s [°/cm]	R_p [°/cm]
Plus	$+11.2 \pm 0.5$	$+22.2 \pm 0.5$
Minus	-11.0 ± 0.3	-22.1 ± 0.5

measurements of spin-IOAM interaction with spin-controlled orbital rotation and orbit-controlled spin rotation are strong evidence that we are observing spin-IOAM interaction. As such, we conclude that the exact simulation is off by about an order of magnitude.

In summary, observed experimental behavior is well described by our theoretical description of the interaction between spin and intrinsic orbital angular momentum. Inversion symmetry between the two control property settings is robust, indicating the absence of circular birefringence for IOAM and SAM, and that the magnitude of the splitting is the same for both combinations of parallel and anti-parallel modes. Some experimental data runs took place over multiple days, and reacquisition of higher-order mode coupling gave consistent output polarization and orientation from day to day. These runs also indicate variation between the segments used in different runs, and a good next step would be characterization of fiber uniformity, over length scales longer than used in these experiments, with spin-IOAM measurements validated against interferometric profiles of the fiber segments.

Characterization of spin-IOAM interaction effects lays the foundation for investigation of spin and both IOAM and EOAM. In fibers with modes well separated in β, and thus robust against intermodal coupling, inclusion of EOAM coupling could make models of output profile orientation, that include fiber path, and allow for

precision encoding of both quantum and classical information in spatial distribution without the extra computation required for MIMO methods. Furthermore, design of fibers with radial structure that produces $\delta\beta = 0$ could eliminate spin-IOAM rotation effects over some wavelength range.

CHAPTER VI

NONLINEAR PHASE EFFECTS IN PHOTON-PAIR GENERATION

6.1 Introduction

Nonlinear optics in optical fibers made from fused silica is dominated by the third-order Kerr nonlinearity $\chi^{(3)}$. $\chi^{(3)}$ processes are also referred to as four-wave mixing (FWM) for the straightforward reason that the interactions occur between four fields. In a quantum picture, the sum of the number of photons created in FWM plus the number annihilated is four. The probability of a particular nonlinear process occurring with a given set of frequencies is determined by the magnitude of the relevant $\chi^{(3)}$ value, energy conservation, and momentum conservation (referred to as phase matching). The energy and phase mismatches are

$$\Delta\omega = \sum_j \omega_j^{\text{out}} - \sum_i \omega_i^{\text{in}} \tag{6.1}$$

$$\Delta\vec{k} = \sum_j \vec{k}_j^{\text{out}} - \sum_i \vec{k}_i^{\text{in}}. \tag{6.2}$$

where i and j index the input and output fields, respectively. Processes with $\Delta\omega = 0$ conserve energy, and processes with $\Delta\vec{k} = 0$ conserve momentum and processes that meet both of these conditions occur with optimal efficiency. Processes that are not perfectly matched exchange energy or momentum with the medium.

In the $\chi^{(3)}$ process of modulation instability, two photons are annihilated from a strong "pump" field and two photons are created in sidebands, historically referred to as the signal (for the higher frequency field) and the idler (for the lower frequency

110

field).[1] The signal and idler share the energy of the two annihilated pump photons. Depending on the properties of the pump field, and both fiber dispersion and length, the pairs of photons produced by modulation instability can share this energy such that their frequencies are entangled, or they can be separable.

If the signal and idler fields contain few photons, modulation instability is a spontaneous process that occurs stochastically. Since the signal and idler photons are correlated in creation time and are always created in pairs, a technique called heralding can be employed where the arrival of one photon signals the system to expect the arrival of the other, and only detections in both the signal and the idler channels in time windows with the expected separation are considered. This technique is effective for isolating single pair-creation events from detections due to noise, and filtering on the heralding photon can be used to conditionally prepare the state of the other [60]. In these experiments, it is common for one of the signal or the idler to be referred to as the "herald" instead. We take the idler to serve as the herald in the following brief description.

The quantum state created by a source that produces photons in pairs can be described in the frequency domain by

$$|\psi\rangle = v|vac\rangle + \epsilon \int \int d\omega_s d\omega_r \psi(\omega_s, \omega_r) a_s^\dagger(\omega_s) a_r^\dagger(\omega_r)|vac\rangle + \epsilon^2 (HOTS). \qquad (6.3)$$

$v = \sqrt{1 - \epsilon^2 - \epsilon^4 - ...} \approx 1$ is the output vacuum amplitude, $\psi(\omega_s, \omega_r)$ is the joint spectral amplitude (also called the wave function) and $a_j^\dagger$ with $j \in \{s, r\}$ is a creation operator. Operating in the regime where ϵ^2 is negligible, the source outputs "biphotons" described by their joint statistics. If the source is configured such that

---

[1]Though these names are often used in the literature without adhering to the frequency ordering convention.

the product photons are separable, then the wave function can be factored into the product of two wave functions

$$\psi(\omega_s, \omega_r) = \psi_s(\omega_s)\psi_r(\omega_r). \tag{6.4}$$

Heralding is commonly performed without resolving frequency information. This traces out the herald photon $\hat{\rho}_s = \text{Tr}_r \left(|\psi\rangle_{s,r} \langle\psi| \right)$. If the wave function is entangled in frequency, this leaves the signal photon in a mixed state, which is undesirable for quantum information processing. If the wave function is separable in frequency, then the signal-state purity is preserved, so it is desirable to design separable sources for use with heralding schemes.

The separability of $\psi(\omega_s, \omega_r)$ can be tailored by design of the group velocities of the pump, signal, and herald fields, as well as the length of the optical fiber. Separability can be achieved by matching the group velocity of the pump field to be the same as the group velocity of exactly one of the signal or herald fields, in a condition called asymmetric group-velocity matching (AGVM). Approximate separability can be achieved when the group velocities of the signal and herald fields are the same, a condition referred to as symmetric group-velocity matching (SGVM), by choosing a combination of the length of the medium and the duration of the pump pulse to balance the value of the signal and herald group velocities, as described in more detail in Sec. 6.3.1. Choosing different ratios of these values under SGVM makes for a source that generates spectrally entangled output photon-pairs.

The same $\chi^{(3)}$ nonlinearity that annihilates two photons from a strong pump mode and produces photon pairs in signal and idler modes through modulation instability gives rise to self-phase modulation (SPM) and cross-phase modulation (XPM), considered together as nonlinear phase modulation (NPM), which will

be present in any real photon-pair source based on four-wave mixing. In our characterization of the photon sources birefringent fiber sources [30, 61], we became interested in the effects of NPM on the output state of our source. Previous work has investigated the effects of nonlinear phase modulation on photon-pair sources, but did not take the temporal structure into account (assume a flat temporal structure) [62]. These effects are often neglected when designing quantum light sources, and, in collaboration with Colin McKinstrie [63–65], we developed a theory that includes them. We find that NPM can increase entanglement for a photon-pair state and change the temporal structure of the process Schmidt modes.

6.2 Theory

Consider pump A_p, signal A_s, and idler A_r fields propagating through an optical fiber with coordinate z denoting position and coordinate t denoting time. t is measured in the rest frame of the pump pulse, which travels at group velocity ν_g^p. The coupled mode equations describing the evolution of the fields along the length of the fiber are [66]

$$\partial_z A_p = i\gamma \left| A_p \right|^2 A_p \tag{6.5}$$

$$(\partial_z + \beta_r' \partial_t) A_r = i2\gamma \left| A_p \right|^2 A_r + i\gamma A_p^2 A_s^* \tag{6.6}$$

$$(\partial_z + \beta_s' \partial_t) A_s = i2\gamma \left| A_p \right|^2 A_s + i\gamma A_p^2 A_r^*, \tag{6.7}$$

where γ is the nonlinear parameter with units $1/(\text{W m})$, and all fields have, in general, temporal and spatial dependence. We use the index i to denote the signal (s) or idler (r) fields only, but the index μ represents all fields, *i.e.* includes the pump. $\beta_i' = \frac{\partial k_z^i}{\partial \omega} - \frac{\partial k_z^p}{\partial \omega} = \frac{1}{\nu_g^i} - \frac{1}{\nu_g^p}$ is the group slowness in $\hat{z}$, the direction of propagation, and

is measured in the rest frame of the pump where $\beta'_p = 0$. A_μ is the (complex-valued) electric field, in units of $\sqrt{W}$. We do not include group-velocity dispersion (*i.e.* are working in the narrow pulse-bandwidth limit). The term on the right-hand side of Eq. 6.5 describes SPM, while the first term on the right-hand sides of Eqs. 6.6-6.7 represent XPM, the effects of which are neglected on the pump as the signal and idler fields are weak.

Pump evolution is given by the solution to Eq. 6.5,

$$A_p(z,t) = \left|A_p(z,t)\right| \exp[i\phi_p(z,t)], \tag{6.8}$$

where

$$\phi_p(z,t) = \phi_p(0,t) + \gamma\left|A_p(z,t)\right|^2 z \tag{6.9}$$

is the pump phase function where the first term is the input temporal phase profile and the second term accounts for self-phase modulation (SPM).
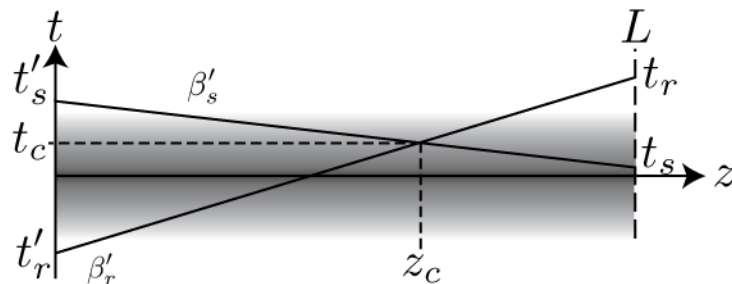
FIGURE 6.1. Ray diagram in the pump rest frame. The gradient is representative of the envelope of the pump, characteristic rays only are shown for the signal and idler, and they intersect at the collision point (z_c, t_c). The slope of the rays is given by the group slownesses, β'_i.

We use the time-domain collision method [64] for determining the Green's functions which are then used to construct the biphoton output state. The Green's functions can be separated into four processes with transfer functions G_{ij} where

114

$j \in \{s, r\}$ indexes the input mode and $i \in \{s, r\}$ indexes the output mode. To find G_{ss} and G_{rr}, consider an input signal impulse $\delta(t')$, in the pump rest frame with the pump pulse maximum at zero, (*e.g.* either the signal ray or idler ray in Fig. 6.1). The phase accumulated by a field propagating under XPM only (from the first term on the right-hand sides of Eqs. 6.6-6.7 is

$$\phi_j(z, t) = 2\gamma \int_{t-\beta'_j L}^{t} \frac{|A_p(s)|^2}{\beta'_j} ds \tag{6.10}$$

for a fiber of length L. The time it takes a pulse to traverse the fiber is $\beta'_i L$, so at the fiber output, $(t = t_{out}, z = L)$

$$G_{ss}(L, t_{out}, t') = \delta(t_{out} - \beta'_s L - t') \exp(i\phi_s(L, t_{out})) \tag{6.11}$$

$$G_{rr}(L, t_{out}, t') = \delta(t_{out} - \beta'_r L - t') \exp(i\phi_r(L, t_{out})) \tag{6.12}$$

The G_{rs} and G_{sr} Green's functions describe the effect of one of the weak fields on the other, and arise from the rightmost terms in Eqs. 6.6-6.7. Consider a ray that describes the path of an impulse idler, $\delta(t_r - \beta'_r L)$, that starts at $(0, t_r - \beta'_r L)$ and ends at (L, t_r). See Fig. 6.1. Define $\beta'_{rs} \equiv \beta'_r - \beta'_s$. The idler ray intersects the signal ray at the collision point, (z_c, t_c), where

$$z_c = (t'_r - (t_r - \beta'_r L)) / \beta'_{rs}, \ t_c = (\beta'_r t'_r - \beta'_s (t_r - \beta'_r L)) / \beta'_{rs}. \tag{6.13}$$

Integrating the modulation instability term in Eqs. 6.6 - 6.7 from the input to the collision point yields $G_{rs}^{+}(z_c, t_c) = i\gamma |A_p(z_c, t_c)|^2 \exp[i(2\phi_p(z_c, t_c) - \phi_s(z_c, t_c))]/\beta'_{rs}$. After the collision, the idler field propagates to the output under XPM (expressed as $\phi_i^{c \to L}(z_c, L, t_i)$), which is the same phase term given in Eq. 6.10 with the limits

115

changed to integrate from the collision point to the fiber output), so the Green's

functions are (for $\beta'_{rs} > 0$)

$$G_{rs}(L,t,t') = \frac{i\gamma}{\beta'_{rs}} \left| A_p(z_c^{rs}, t_c^{rs}) \right|^2 H(t' - t + \beta'_r L) H(t - \beta'_s L - t')$$

$$\cdot \exp\left[i \left(2\phi_p(z_c^{rs}, t_c^{rs}) - \phi_s(z_c^{rs}, t_c^{rs}) + \phi_r^{c\rightarrow L}(z_c^{rs}, L, t) \right) \right] \tag{6.14}$$

$$z_c^{rs} = \frac{1}{\beta'_{rs}} (t' - (t - \beta'_r L)) \tag{6.15}$$

$$t_c^{rs} = \frac{1}{\beta'_{rs}} \left(\beta'_r t' - \beta'_s(t - \beta'_r L) \right) \tag{6.16}$$

and

$$G_{sr}(L,t,t') = \frac{i\gamma}{\beta'_{rs}} \left| A_p(z_c^{sr}, t_c^{sr}) \right|^2 H(t' - t + \beta'_r L) H(t - \beta'_s L - t')$$

$$\cdot \exp\left[i \left(2\phi_p \left(z_c^{sr}, t_c^{sr} \right) - \phi_r \left(z_c^{sr}, t_c^{sr} \right) + \phi_s^{c\rightarrow L}(z_c^{sr}, L, t) \right) \right] \tag{6.17}$$

$$z_c^{sr} = \frac{1}{\beta'_{rs}} ((t - \beta'_s L) - t') \tag{6.18}$$

$$t_c^{sr} = \frac{1}{\beta'_{rs}} \left(\beta'_r (t - \beta'_s L) - \beta'_s t' \right). \tag{6.19}$$

The output state of the signal and idler biphoton can be described with the

Green's functions. Let the output times for the signal and idler fields be t_s and t_r.

The collision coordinates coordinates above in Eqs. 6.18-6.15 are not common in

that t and t' are the input and output time for different fields, with different group

velocities, in each equation. The common collision coordinates and temporal window

function are

	$\beta'_{rs} > 0$	$\beta'_{rs} < 0$
t_c	$(\beta'_r t_s - \beta'_s t_r)/\beta'_{rs}$	$(\beta'_s t_r - \beta'_r t_s)/\beta'_{sr}$
z_c	$L + (t_s - t_r)/\beta'_{rs}$	$L + (t_r - t_s)/\beta'_{sr}$
W_c	$H(t_r - t_s)H(t_s - t_r + \beta'_{rs}L)$	$H(t_s - t_r)H(t_r - t_s + \beta'_{sr}L)$

(6.20)

where H is a Heaviside step function. Modulation instability with a vacuum state for the signal and idler fields at the input, denoted with the a subscript, and produces pairs of photons which exit the fiber at the output, denoted with the subscript b, described in the time domain by the state

$$|\psi\rangle = |vac\rangle_a = v|vac\rangle_b + \epsilon \int\int dt_s dt_r \psi(t_s, t_r) b_s^\dagger(t_s) b_r^\dagger(t_r)|vac\rangle_b + \epsilon^2(HOTS). \quad (6.21)$$

where $v = \sqrt{1 - \epsilon^2 - \epsilon^4 - ...} \approx 1$ is the output vacuum amplitude, and we work in the Heisenberg picture where time evolution does not change the state, but causes the state to be represented in a different basis. In the low-gain regime, $\epsilon^2 \ll \epsilon$, we can neglect the higher-order terms ($HOTS$). The input and output ladder operators are related to each other through the backward Green's functions, denoted h_{ij} with $i, j \in \{s, r\}$,

$$a_s(t) = \int dt' \, h_{ss}(t, t') b_s(t') + \int dt' \, h_{sr}(t, t') b_r^\dagger(t') \quad (6.22)$$

$$a_r(t) = \int dt' \, h_{rr}(t, t') b_r(t') + \int dt' \, h_{rs}(t, t') b_s^\dagger(t'), \quad (6.23)$$

and the reciprocity equations

$$h_{ss}(t, t') = g_{ss}^*(t', t) = G_{ss}^*(L, t', t) \qquad h_{rs}(t, t') = -g_{sr}(t', t) = -G_{sr}(L, t', t)$$

$$(6.24)$$

$$h_{rr}(t, t') = -g_{rr}^*(t', t) = -G_{rr}^*(L, t', t) \qquad h_{sr}(t, t') = g_{rs}(t', t) = G_{rs}(L, t', t) \quad (6.25)$$

relate the backward Green's functions to the forward Green's functions. Using the fact that G_{ss} and G_{rr} are proportional to delta functions, it follows that the joint temporal amplitude is

$$\psi(t_s, t_r) = -G_{rs}(L, t_r, t_s - \beta_s' L) \exp(i\phi_s(L, t_s)) \qquad (6.26)$$

$$= -G_{sr}(L, t_s, t_r - \beta_r' L) \exp(i\phi_r(L, t_r)) \qquad (6.27)$$

$$= \frac{-i\gamma}{|\beta_{rs}'|} |A_p(z_c, t_c)|^2 W_c(t_s, t_r) \exp\left[i\left[2\phi_p(z_c, t_c) + \phi_r^{c \to L}(z_c, L, t_r) + \phi_s^{c \to L}(z_c, L, t_s)\right]\right],$$

$$(6.28)$$

where $\phi_i^{c \to L}$ indicates the phase accumulated by a field due to XPM from the collision point through exiting the fiber. This phase structure has a straightforward interpretation: the pump pulse enters the fiber and undergoes SPM until a photon-pair is produced, and then the signal and idler fields propagate under XPM until they exit the fiber. The pair creation process can happen anywhere along the length of the fiber, and the state describes the probability amplitude distribution for detecting both an idler photon at t_r and a signal photon at t_s.

6.2.1 Gaussian Pulse Shapes

To proceed from here, we will assume a Gaussian temporal profile for the pump pulse, with a flat temporal phase profile at the fiber input, $\phi_p(0,t) = 0$. The functions that describe the state are then

$$\left|A_p(z_c, t_c)\right|^2 = \frac{P_P}{\sqrt{\pi}} \exp\left(\frac{-t_c^2}{\sigma_p^2}\right) \tag{6.29}$$

$$\phi_p(z_c, t_c) = \gamma \left|A_p(z_c, t_c)\right|^2 z_c \tag{6.30}$$

$$\phi_i^{c \to L}(z_c, L, t_i) = \frac{P_P \gamma \sigma_p}{\beta_i'} \left(\operatorname{erf}\left(\frac{t_i - \beta_i' z_c}{\sigma_p}\right) - \operatorname{erf}\left(\frac{t_i - \beta_i' L}{\sigma_p}\right)\right), \tag{6.31}$$

where $i \in \{s, r\}$, $z_c = L + (t_r - t_s)/\beta_{sr}'$, $t_c = (\beta_s' t_r - \beta_r' t_s)/\beta_{sr}'$, and erf is an error function. From here on out, we'll work with $\beta_{rs}' < 0$ variables from Table 6.20.

6.2.2 Perturbation Theory Limits

To check the bounds of the perturbation theory, we interpret ϵ^2 as the probability of one photon-pair being measured at the output. Using the appropriate term from Eq. 6.21,

$$\langle 1_{t_s}, 1_{t_r} | 1_{t_s}, 1_{t_r} \rangle = \epsilon^2 \int_{-\infty}^{\infty} \int_{-\infty}^{\infty} |\psi(t_s, t_r)|^2 dt_s \, dt_r, \tag{6.32}$$

we can absorb all the probability into ϵ^2, which is to say that if we renormalize ψ such that $1 = \int_{-\infty}^{\infty} \int_{-\infty}^{\infty} |\psi(t_s, t_r)|^2 dt_s \, dt_r$ then

$$\epsilon^2 = \gamma^2 P_P^2 \frac{\sigma_p L}{|\beta_{sr}'|} \sqrt{\frac{\pi}{2}} = \phi_{max}^2 \frac{\sigma_p}{|\beta_{sr}'| L} \sqrt{\frac{\pi}{2}}, \tag{6.33}$$

where $\phi_{max} = \gamma P_P L$ is the maximum phase accumulated over the length of the fiber due to SPM.

For Gaussian pulses and symmetric group-velocity matching, simulation indicates that the maximum purity occurs when $\sigma_p/(\beta'_{sr}L) \approx 1/4$. Assuming this condition, Eq. 6.33 becomes

$$\epsilon^2 = \phi_{max}^2 \sqrt{\frac{\pi}{32}}. \tag{6.34}$$

We neglected terms of ϵ^2 in our derivation of ψ by assuming $\epsilon \ll 1$, so the maximum phase accumulated, ϕ_{max}, must also be small for separable states under symmetric group-velocity matching. For cases other than symmetric group-velocity matching, ϵ can be kept small, while ϕ_{max} is not small, by adjusting the aspect ratio $\frac{\sigma_p}{|\beta'_{sr}|L}$, within bounds set by neglecting dispersion, avoiding stimulated Brillouin scattering, and ensuring that the walkoff of the products allows for coincident detection to exclusively come from pairs generated by the same pump pulse.

6.3 Numerical Simulation

Code for calculating the state, performing Schmidt decompositions and state purity are implemented in Mathematica.

6.3.1 Phase Structure and Effects

The structure of the wave function, ψ, also called a joint temporal amplitude (JTA) in the time domain, is shown in is shown in Fig. 6.2). The amplitude is a Gaussian traveling in (t_r, t_s) space an angle defined by $\theta = \arctan[\beta'_r/\beta'_s]$, truncated by the window function W_c. The phase structure due to SPM in the pump is oriented along θ, and the ratio between σ_p and the window width, $\beta'_{sr}L$ determine the separability of the state. Entangled light is produced when $\theta = \pm 45°$, and the aspect ratio, $\sigma_p/(\beta'_{sr}L)$, is either large or close to zero.

Separable states, where $\psi(t_s, t_r) = f(t_s)g(t_r)$ for some functions f and g, can be created through asymmetric group-velocity matching (AGVM), where $\beta'_i = \beta'_p$ for exactly one of the signal or the idler fields, and approximately separable states can be made with symmetric group-velocity matching (SGVM), where $\beta'_s = \pm\beta'_r \therefore \theta = \pm 45$ and the aspect ratio, $\sigma_p/(\beta'_{sr}L) \approx 1/4$ for Gaussian pump profiles. The plots in Fig. 6.2 were generated with $\gamma = 0.01, \sigma_p = 1, L = 4$, and β'_s, β'_r in the range $\{-1, 1\}$ chosen for the desired $\theta = \arctan(\beta'_r/\beta'_s)$ with the constraint that $\beta'_{sr} = 1$. That is to say that I chose a separable SGVM condition and then varied θ. Highly entangled states with a small aspect ratio are optimally oriented to gain entanglement from SPM (and are investigated in Section 6.3.2.2), while those with an aspect ratio much greater than 4 can not simultaneously accrue appreciable ϕ_{max} while ϵ remains small.

The JTA gives the probability amplitude of detecting the idler at t_r and the signal at t_s, at the fiber output, where the times are referenced to the pump peak exiting the fiber at time zero. A biphoton created at the fiber exit and detected at $t_s = t_r = 0$ will have a phase imprint from SPM with no contribution from XPM, as is seen at the origin of the SPM phase plots of Fig. 6.2. Biphotons created at the fiber input have no SPM phase contribution, but travel with different group velocities under XPM, creating the two phase lobes shown in the XPM plots of Fig. 6.2. The steepness of the phase lobes is set by σ_p, and β'_r and β'_s control the slope of the XPM phase lobes independently.

How different is the state coming out of a fiber versus what you think it would be if you neglect the nonlinear phase effects? One way to gauge this is by taking the overlap integral of the state without nonlinear phase effects and the state with

121

nonlinear phase effects included:

$$\mathscr{O} = \langle \psi_{on} | \psi_{off} \rangle. \tag{6.35}$$

Fig. 6.3b shows the effects of increasing the power on $\mathscr{O}$ using the same group velocities used to make the JTAs displayed in Fig. 6.2.

It is common for one photon from a biphoton source, for example the idler, to act as a herald, and if the properties of the herald are not resolved, then the signal is in a mixed state after detection of the idler. Mixed states are undesirable for quantum information processing (*e.g.* interference at gates). Here, we use purity,

$$\mathscr{P} = \mathrm{Tr}(\rho_s^2), \tag{6.36}$$

where ρ_s is the reduced density matrix with the idler traced out, to refer to the purity of the reduced system of the signal only. This assumes that the idler is detected, but its time of arrival is not resolved. We perform the numerical calculation by taking the sum of the Schmidt coefficients to the fourth power (which is equivalent to Eq. 6.36). Fig. 6.3a shows the change in purities due to changing power for states with the same group velocities used in Fig. 6.2. The purity degradation *vs.* ϵ^2 due to NPM is a straight line (in this regime), so to investigate which θ degrades purity the most, we measure the degradation as the purity at $\epsilon^2 = 0.005$ minus the purity at $\epsilon^2 = 0.48$, (see Fig. 6.4).

Under SGVM with a separable aspect ratio, the phase structure entangles signal and idler photons, but the effect on purity is small, as is necessitated in our perturbation regime by the constraint of Eq. 6.34. The maximum purity achievable under SGVM, neglecting nonlinear phase, is 0.82 [67]. Using the same parameters,

Fig. 6.4 shows that the purity degrades the most at around $(-45 \pm 26.6)°$, which is $-71.6°$ or $-18.4°$. Under AGVM, the phase structure is exactly separable and the purity is not dependent on pump power.

6.3.2 Realistic Cases

We use birefringent fiber sources after Smith *et al.* [30] and report realistic values for a Fibercore HB750 fiber, and the very similar HB800 fiber. We use the parameter values: $\gamma = \frac{\omega_0 n_2}{c A_{\text{eff}}}$ and $c = 299792458$ m/s. Following Agrawal [66], $n_2 = 7.7 \times 10^{-21}$ m^2/W (the recommended 2.3×10^{-20} m^2/W, divided by 3 because we assume a cross polarized process). The effective area was calculated using HB800 parameters[2] to be $A_{\text{eff}} = 13\,\mu$m^2 at $\lambda_p = 802$ nm, and $A_{\text{eff}} = 22\,\mu$m^2 at $\lambda_p = 1089$ nm, and $A_{\text{eff}} = 22\,\mu$m^2 at 1089 nm. Pulses were assumed to have Gaussian temporal profiles, which means their peak power $P_P = P_{ave}/(R\sigma_p\sqrt{\pi})$ where R is the repetition rate, which we take to be 76 MHz.

6.3.2.1 SGVM - separable

For separable SGVM the effects of NPM do not change the state much within the domain of validity the perturbation theory, as we expect from condition 6.34. That is to say, as long as the source is run in the regime where the probability of more than one photon-pair creation event within the detection time window is negligible, the effects from NPM on the state are also small. Perfect SGVM is not experimentally achievable in the HB750 due to its dispersion structure, and we work around $\theta = -42°$, so we use our parameters from Section 6.3.2 and $L = 3.3$ m as a typical case. Degradation

---

[2]The effective areas of the fundamental modes of the HB750 and HB800 are similar enough to be used interchangeably.

of the overlap and purity is shown in Fig. 6.5. The Schmidt modes as a function of ϵ^2 are shown after the references in Table 6.1. Though the effect is small, we include the Schmidt modes for the wave function in table 6.1. Neglecting NPM is a good approximation in the low-gain regime for separable SGVM.

6.3.2.2 SGVM - entangled

Now we examine sources designed to produce entangled photon-pairs. Using a length of $L = 100$ m for our fiber, the state has an aspect ratio of 0.0082, and is shown in Fig. 6.6. The degradation of the purity and overlap is shown in Fig. 6.7. At $\epsilon^2 = 0.105$, $\mathscr{O} = 0.38$ and the Schmidt number $\mathscr{K} = 1/\mathscr{P}$ increases from 17 with NPM off to $\mathscr{K} = 24$ with NPM on. Schmidt number is an entanglement monotone [68], which means that the amount of entanglement resource cannot decrease as $\mathscr{K}$ increases.[3] Thus, increased Schmidt number suggests that NPM increases the amount of entanglement resource in the output state, but utilization of that entanglement would require a phase-sensitive detection method, such as temporal mode interferometry [69]. The Schmidt modes are shown in Table 6.2.

6.3.2.3 AGVM - short pulses

The NPM phase structure has the largest effect on purity and overlap when ϕ_{max} is maximized, which can be accomplished while staying in the $\epsilon^2 \ll 1$ regime, (see Eq. 6.33), by minimizing $\sigma_p/(|\beta'_{sr}|L)$. The two extreme regimes are short pulse duration, which is limited in our model by the negligence of group velocity dispersion, and long pulse duration, limited by stimulated Brilloun scattering and walkoff.

---

[3]Strictly speaking, the amount of entanglement resource could, pathologically, stay the same.
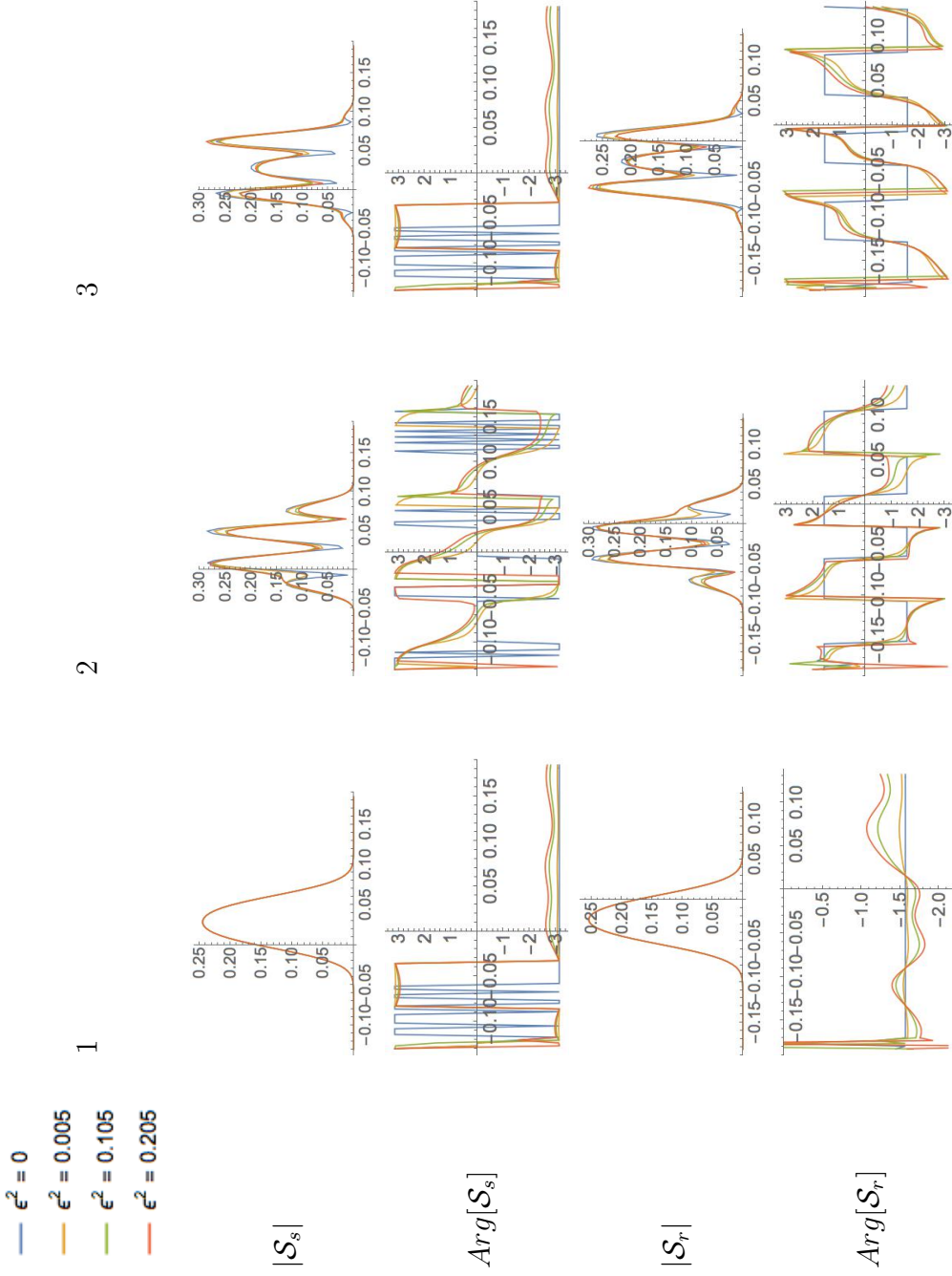
TABLE 6.1 First 3 Schmidt modes for SGVM with $\theta = -42°$. The fast phase jumps are numerical artifacts of the Arg() function. The signal and idler modes have their amplitudes shifted in opposite directions, and those directions flip with even and odd mode number. The x-axis is in ns while the y-axis is in AU.

125

TABLE 6.2 First 3 Schmidt modes for entangled SGVM with $\theta = -42°$. The fast phase jumps are numerical artifacts of the Arg() function. The signal and idler modes have their amplitudes shifted in opposite directions, and those directions flip with even and odd mode number. The x-axis is in ns while the y-axis is in AU.
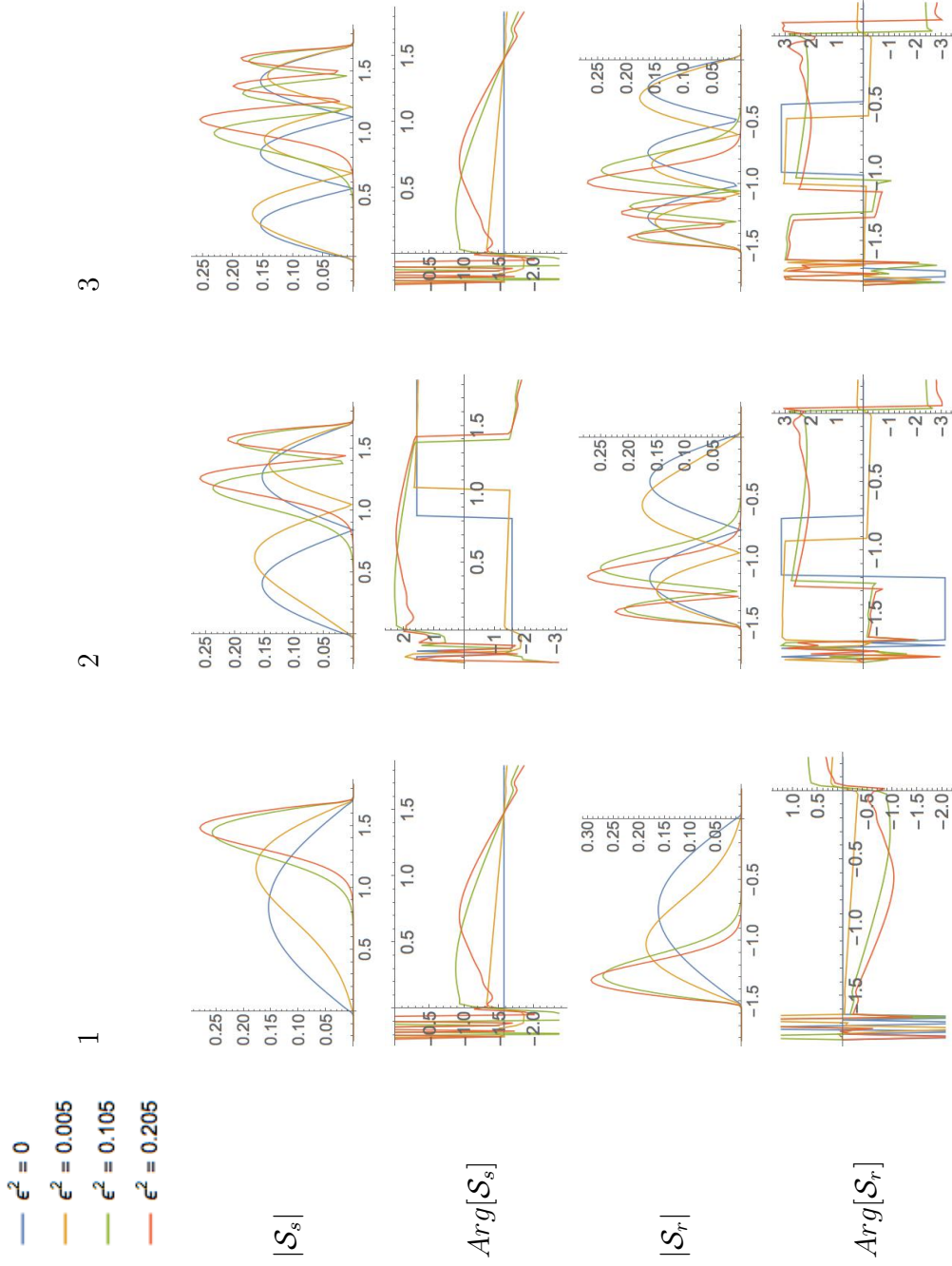
Agrawal's dispersion length $L_D = \sigma_p^2/|\beta_2'|$ where β_2' is the GVD parameter, and neglecting dispersion is a good approximation when $L \ll L_D$. Keeping $L = 3.3$ m, we set pulse duration to $\sigma_p = 1$ ps, which is in the range $L_D/L \approx 20$. AGVM is achieved in the HB750 fiber at $\lambda_p = 1089\,\mu$m, $\lambda_s = 825.1\,$nm, $\lambda_r = 1602\,$nm, which gives $\theta = 0.01 \approx 0$. Under AGVM, the purity is unaffected by increasing ϵ^2, *i.e.* peak power, but the nonlinear phase contribution to the state is substantial, reducing the overlap, as shown in Fig. 6.8. At $\epsilon^2 = 0.105$, which corresponds to $P_P = 285$ W, the overlap is 0.83. The Schmidt modes for the process are changed by NPM, as shown in Table 6.3. The phase structure is simple in the flat AGVM case.

What if the pump is tuned a little to change the central wavelengths of the photon pairs? This seems a likely case for neglect of NPM resulting in a smaller actual purity than expected. Small changes from perfect AGVM can result in purity degradation, as shown for a 1.75 nm detuning to $\lambda_p = 1091$ nm, $\lambda_s = 825.1$ nm, $\lambda_r = 1610$ nm, which corresponds to $\theta = 0.9°$. This reduces the purity by creating a non-separable amplitude, but NPM further reduces the purity as P_P increases. The resulting ϵ^2 dependence is shown in Fig. 6.9. The Schmidt modes for this wave function, $\mathcal{S}_i$ where $i \in \{s, r\}$, are shown in Table 6.4. The purity is decreased from about 0.88 to 0.74, a degradation of about 0.14.

6.3.2.4 AGVM - long fibers

Theoretically, the regime where perturbation theory works and ϕ_{max} is largest is with large pulse durations and long fiber lengths. This follows from combining the $L_D = 20L$ heuristic with the ratio $\sigma_p/(|\beta_{sr}'|L)$. Practically, long fibers and long pulse durations make for a cumbersome, low-brightness photon-pair source.
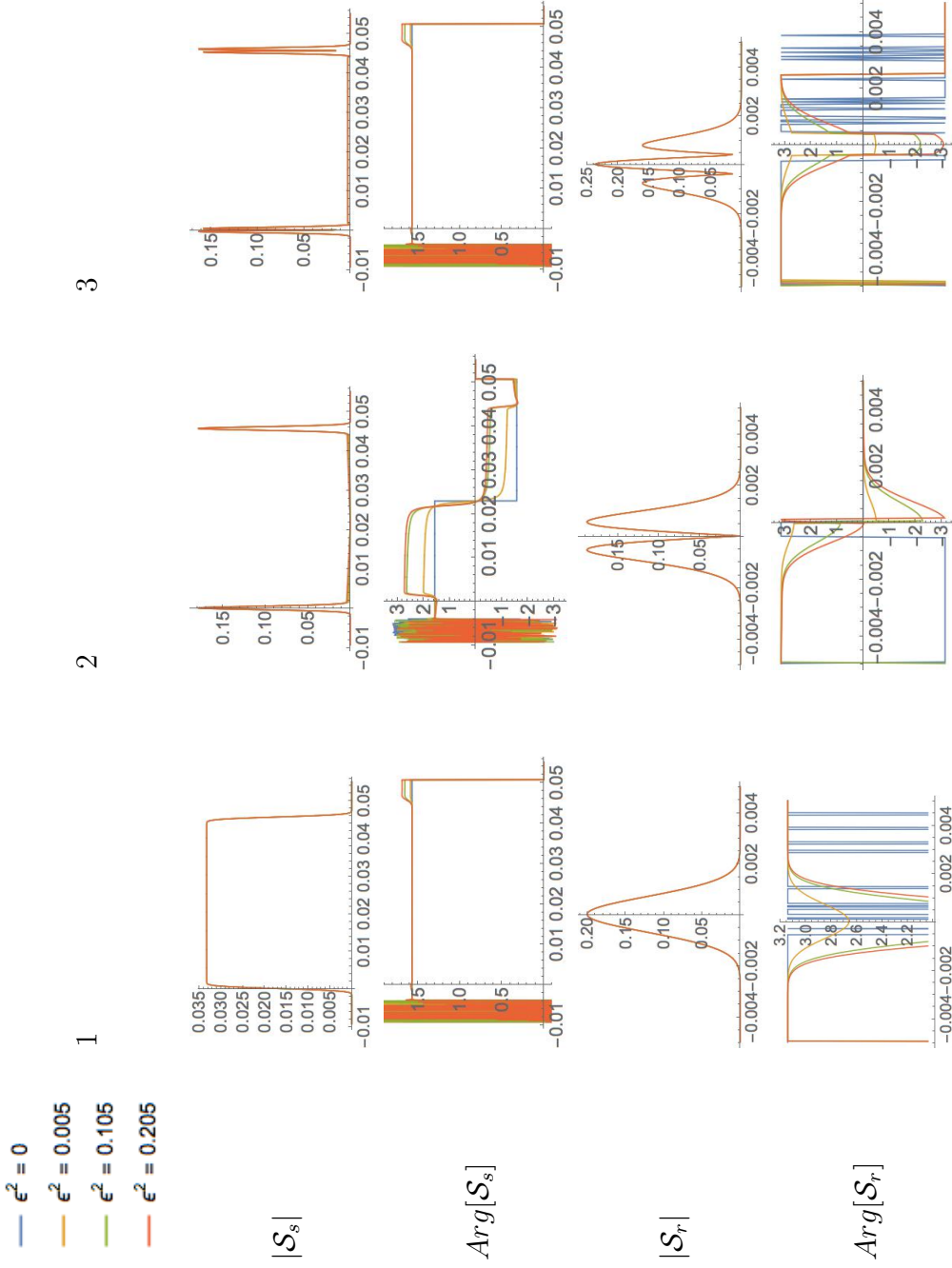
TABLE 6.3 First 3 Schmidt modes for AGVM with $\theta = 0°$. The fast oscillations are numerical artifacts of the Arg() function. With no tilt, the amplitude structure does not change with increased ϵ, *i.e.* P_P. P_P. The x-axis is in ns while the y-axis is in AU.
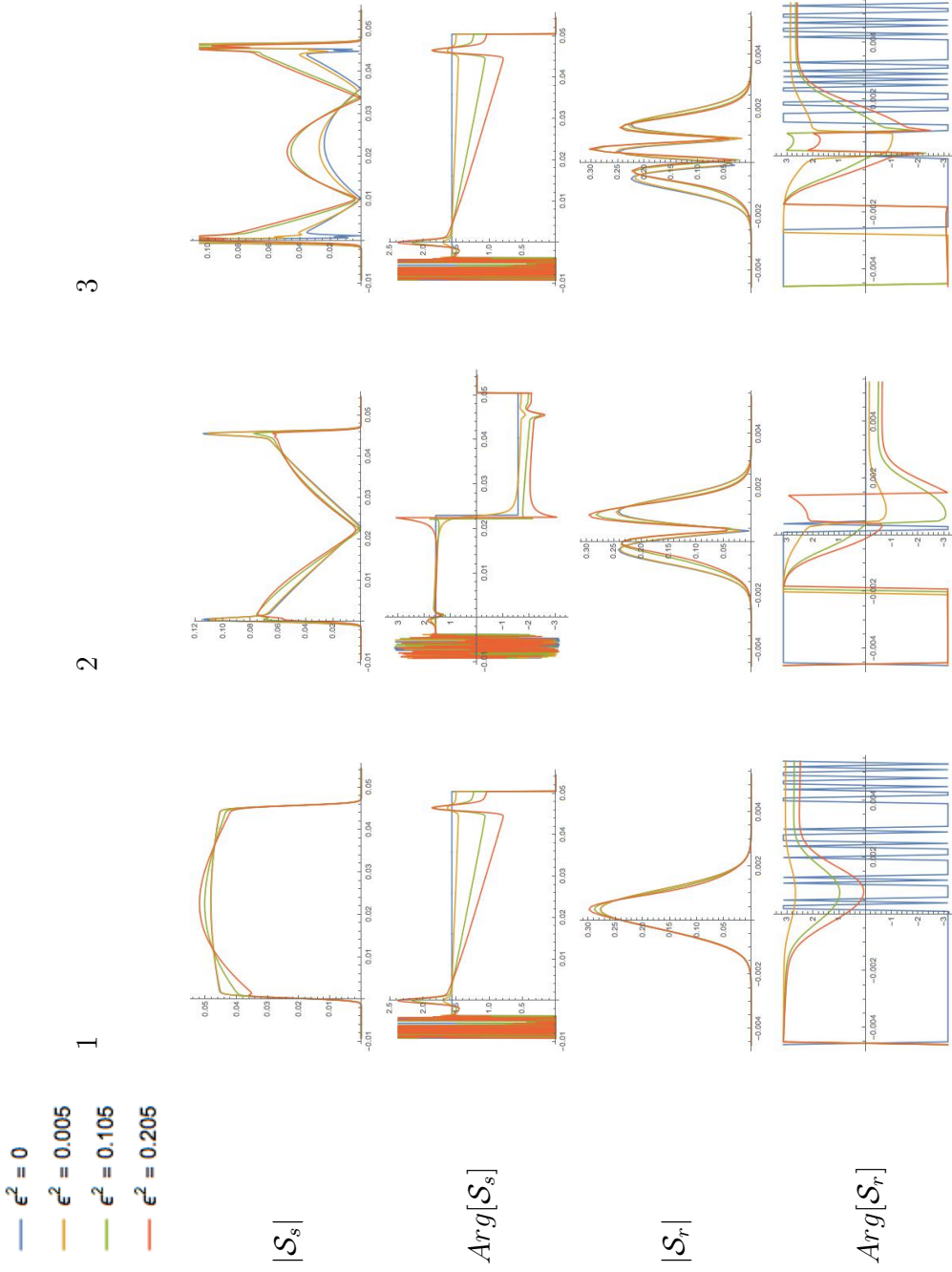
TABLE 6.4 First 3 Schmidt modes for AGVM with $\theta = 0.9°$. The fast oscillations are numerical artifacts of the Arg() function. With no tilt, the amplitude structure does not change with increased ϵ, *i.e.* P_P. The x-axis is in ns while the y-axis is in AU.

129

Long fibers can make for large walkoff times between signal and idler fields, and this time must be kept small enough to be sure that coincident detections are coming from a single photon-pair creation event. Allowing products generated by one pump pulse to overlap with those created by a temporally adjacent pump pulse would increase false coincidences. Defining the pump pulse train period $T_p \equiv 1/R$, and the coincidence window Δt, I propose the guideline

$$T_p > 3\sigma_p + \beta'_{sr}L + \Delta t \tag{6.37}$$

to ensure that coincidences are not attributable to MI products from adjacent pump pulses.

To avoid Brilloun scattering, I chose $\sigma_p = 0.5$ ns on rough guidance from Agrawal's text [66], and chose $L = 500$ m to stay on the good side of condition 6.37 by ~ 2 ns. At $\lambda_p = 1091$ nm, $\lambda_s = 825.1$ nm, $\lambda_r = 1610$ nm, where $\theta = 0.9°$, the purity and overlap degradation is shown in Fig. 6.10.

In search of the worst case, lowering the repetition rate of the laser allows for use of much longer fibers while remaining in the perturbative regime. Using $\sigma_p = 0.5$ ns, L = 10 km (which is inside the limit of order one hundred km, set by fiber loss, for the transmission of quantum information [70]), $R = 5$ kHz, and $\lambda_p = 1089.8$ nm, λ_s = 825.1 nm, $\lambda_r = 1604$ nm, give $\theta = 0.27°$, which is a large enough angular mismatch to give large degradation over the long length, as shown in Fig. 6.11.

6.4 Discussion

Self- and cross-phase modulation modify the phase structure of biphotons out of a fiber source utilizing modulation instability, which can decrease purity if neglected

when designing a separable source. In the low-gain regime, the effects of NPM on sources designed with separable symmetric group-velocity matching are small. For entangled sources designed with symmetric group velocities, the state can be appreciably affected, causing changes to the Schmidt modes. The increased Schmidt number in this case suggests entanglement resource generation is improved, and could be accessed with phase-sensitive Schmidt mode detection. Separable sources utilizing short pulses and perfect asymmetric group-velocity matching show appreciable change in state structure but no change in purity, under NPM. If such a source is detuned to slightly imperfect asymmetric group-velocity matching, then purity will decrease due to NPM. Long fibers with long pump pulse durations are the most effected by NPM, and show substantial state change and purity degradation.
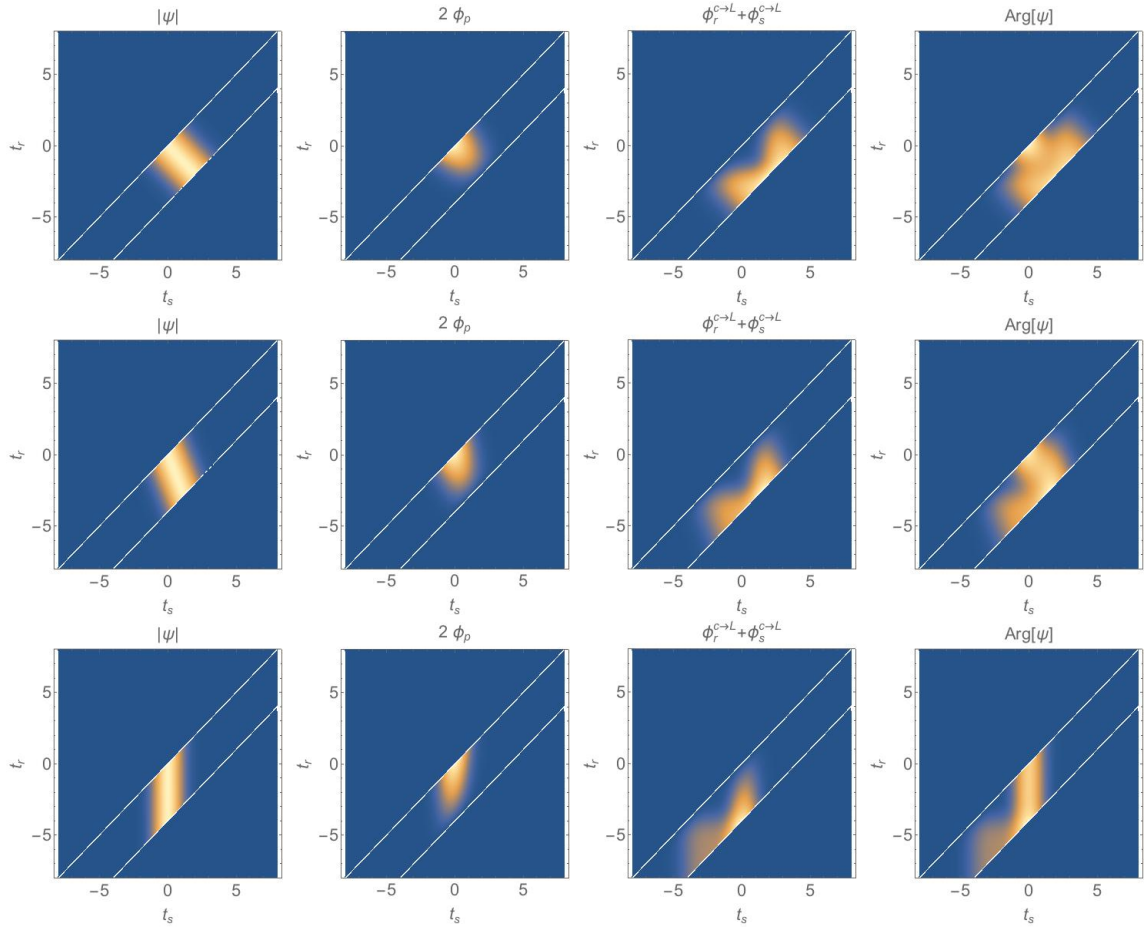
FIGURE 6.2. Amplitude and phase of ψ. Top row: $\theta = -45°$, middle row: $-67.5°$, and bottom row: $\theta = -90°$. The purpose of these plots is to show the structure of ψ; the input parameters are arbitrary. The columns from left to right show: amplitude, SPM phase contribution, XPM phase contribution, and total nonlinear phase contributions.
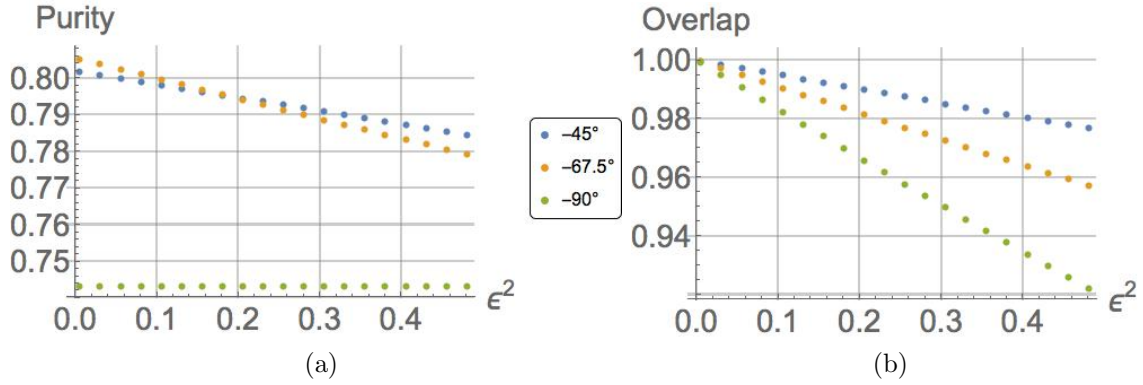
FIGURE 6.3. Purities and Overlaps *vs.* ϵ^2 for different group-velocity matching conditions, labeled by θ in the legend.
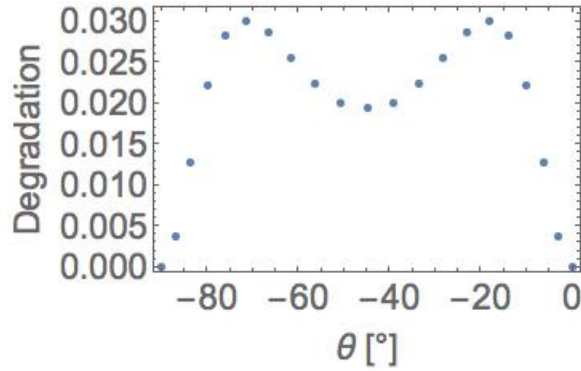
FIGURE 6.4. Degradation *vs.* θ with constant aspect ratio, $\sigma_p/(|\beta'_{sr}|L)$.
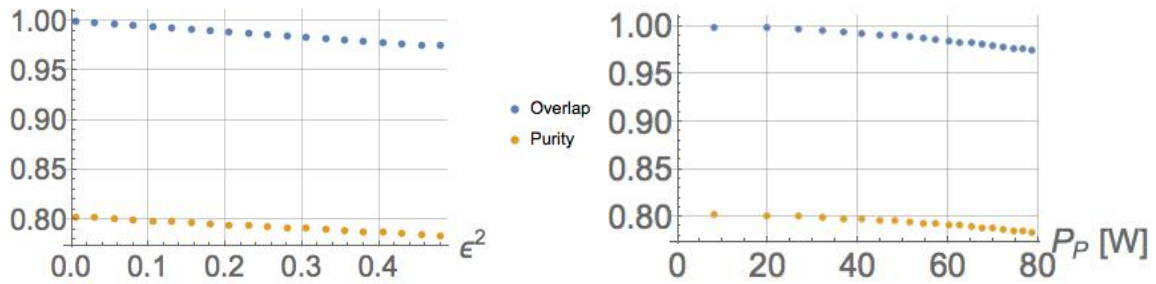
FIGURE 6.5. $\theta = -42°$: Degradation for the HB750 fiber under separable SGVM.
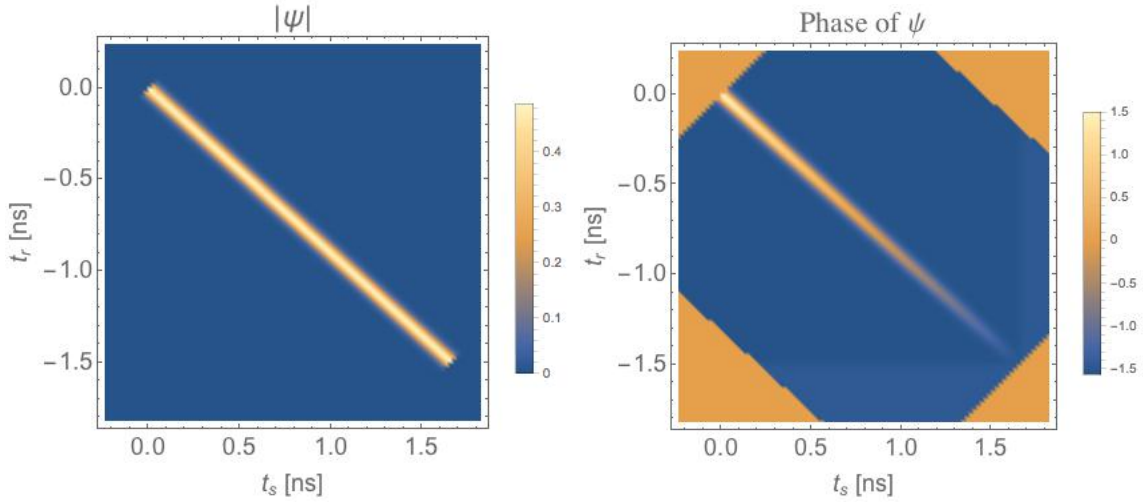
FIGURE 6.6. $\theta = -42°$: Absolute value and phase of $\psi(t_s, t_r)$. The yellow regions of zero phase corresponding to $|\psi| = 0$ are not meaningful.
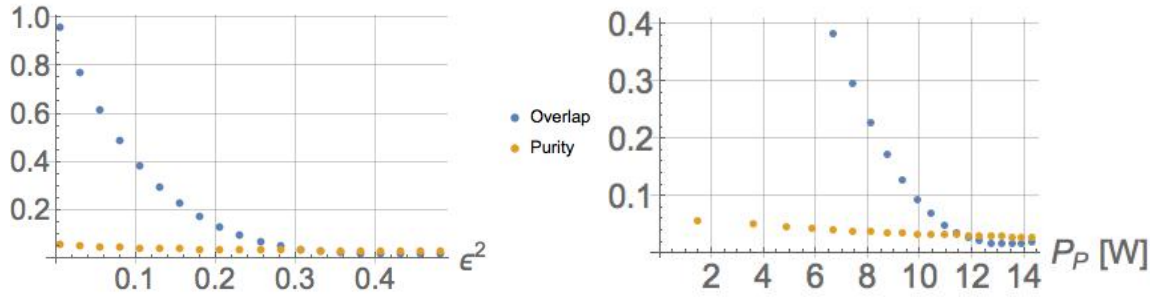
FIGURE 6.7. $\theta = -42°$: Degradation for HB750 fiber under entangled SGVM. The plot on the right is zoomed to show purity degradation.
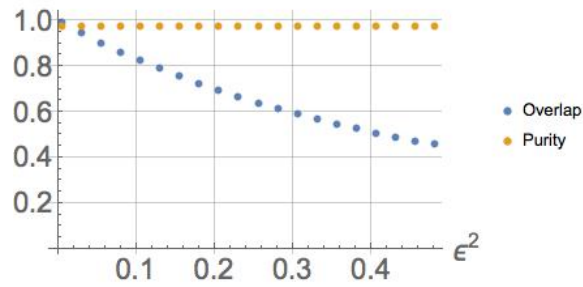
FIGURE 6.8. Overlap and purity for short pulses and AGVM parameters.
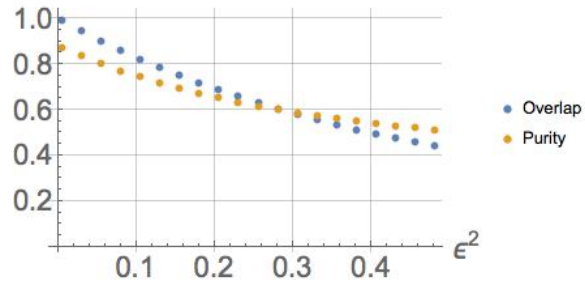
FIGURE 6.9. Purity and overlap *vs.* ϵ^2 with short pulses close to AGVM, with $\theta = 0.9°$.
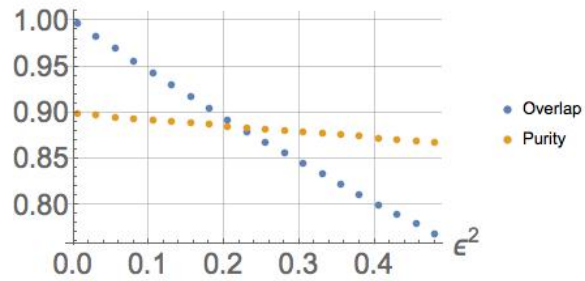
FIGURE 6.10. $\theta = 0.9°$, L $= 500$ m, $\sigma_p = 0.5$ ns: long fiber degradation.
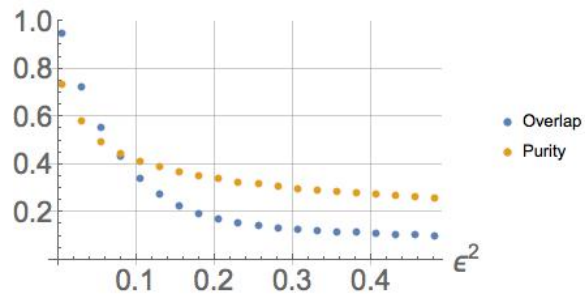
FIGURE 6.11. $\theta = 0.27°$, L $= 10$ km, $\sigma_p = 0.5$ ns: long fiber degradation with low repetition rate $R = 5$ kHz.

135

CHAPTER VII

CONCLUSIONS

In this dissertation, we investigate interaction between properties of light as it propagates through a medium. We begin in Chapter II with a brief overview of spatial modes in free space and in optical fiber, and describe how coupling between the intrinsic spin of light and its intrinsic orbital angular momentum (IOAM) gives rise to fine structure of the longitudinal propagation constants of bound fiber modes. We discuss how excitation of parallel and anti-parallel combinations of fiber modes exhibit the rotational beating effects of spin-controlled orbital rotation and orbit-controlled spin rotation, and how their measurement reveals the splitting due to spin-IOAM interaction. In Chapter III, we use a toy model to garner insight into the effects of the excitation of undesired modes, along with the desired ones, both at the input of the fiber, and due to defect-driven constant unitary coupling with propagation.

Experimental methods for preparing, coupling, and measuring our desired spatial and polarization states after propagation through a few-mode fiber are detailed in Chapter IV. Chapter V explores experimental observations of spin-IOAM interaction and wavelength tuning experiments used as figures of merit for improvement of simulations of the exact modes of our experimental fiber. Our theoretical predictions from Chapter II describe observed behavior well, even in the presence of weak mode coupling. Future research into the simultaneous coupling of extrinsic as well as intrinsic orbital angular momentum to spin could allow for precise encoding of classical or quantum information in the spatial distribution of light sent through optical fibers.

Chapter VI presents theoretical investigation of the effects of self- and cross-phase modulation on photon sources operating with a single spatial profile. After discussion

136

of desired behavior for quantum light sources, we describe a model predicting how both nonlinear phase modulation effects change the biphoton state output from a fiber source and use a numerical simulation to explore regimes in which the effects can be safely neglected and when neglecting them will produce errors in the complex-valued temporal structure of the wave function and the purity of the state describing signal photons upon heralding. We find that effects of NPM are small on separable sources utilizing symmetric group velocity matching, but appreciably change the state of entangled sources with the same group velocity matching scheme. We also find suggestion that nonlinear phase modulation could provide more entanglement resource from fiber photon sources for quantum information applications if phase-sensitive detection methods, such as temporal mode interferometry, are used. We find that NPM has the largest effect on state structure and photon purity after heralding for long pump pulses in long fibers with low repetition rates.

APPENDIX

SPIN-ORBIT INTERACTION WITH EXACT MODES

Recall that beams carrying single-valued IOAM have a phase profile $\exp[i\ell\phi]$ with $\ell = \mu|\ell|$ and beams with circular polarization have polarization vector $\hat{e}_\sigma$. Two exact modes with propagation constants β_1 and β_2 will exhibit beating effects dependent upon $\Delta\beta = \beta_2 - \beta_1$, if excited together. Let the central propagation constant be $\bar{\beta} = (\beta_2 + \beta_1)/2$ and half the difference be $\delta\beta' = \Delta\beta/2 = (\beta_2 - \beta_1)/2$. The beating between a parallel and an anti-parallel mode with the same underlying quantum numbers, $|\ell|$ and m (radial index), is driven by the linearized azimuthal polarization correction to the propagation constant $\delta\beta_2$ from Eq. 2.41, which is the same as $\delta\beta'$ in a cylindrically symmetric waveguide in the low contrast (weak guidance) limit with $\delta\beta' \ll \bar{\beta}$, which we assume in this chapter. The exact central propagation constant $\bar{\beta}$ corresponds to the scalar mode propagation constant $\tilde{\beta}$ plus the linearized radial polarization correction as $\bar{\beta} = \tilde{\beta} + \delta\beta_1$.

The scalar approximate modes referred to as "linearly polarized" or LP modes have the form:

$$\vec{\mathrm{LP}}_{\ell,m}(\rho,\phi,z) = \psi_{|\ell|,m}(\rho)g_\ell(\phi)e^{i(\tilde{\beta}z-\omega t)}\hat{e} \tag{A.1}$$

where $\psi_{|\ell|,m}(\rho)$ is the radial mode function and $g_\ell(\phi) = \cos(\ell\phi)$ for even parity modes and $g_\ell(\phi) = \sin(\ell\phi)$ for odd modes, and $\hat{e}$ is a linear polarization vector, *e.g.* $\hat{x}$ or $\hat{y}$. In the low contrast (weak guidance) limit, the exact modes transverse spatial distribution and polarization (*sans* traveling wave phase factors) take the simple form

of combinations of LP modes [48]

$$\vec{\mathrm{HE}}^{e}_{|\ell|+1,m} = \psi_{|\ell|,m}(\rho)(\hat{x}\cos(|\ell|\phi) - \hat{y}\sin(|\ell|\phi)) \tag{A.2}$$

$$\vec{\mathrm{EH}}^{e}_{|\ell|-1,m} = \psi_{|\ell|,m}(\rho)(\hat{x}\cos(|\ell|\phi) + \hat{y}\sin(|\ell|\phi)) \tag{A.3}$$

$$\vec{\mathrm{HE}}^{o}_{|\ell|+1,m} = \psi_{|\ell|,m}(\rho)(\hat{x}\sin(|\ell|\phi) + \hat{y}\cos(|\ell|\phi)) \tag{A.4}$$

$$\vec{\mathrm{EH}}^{o}_{|\ell|-1,m} = \psi_{|\ell|,m}(\rho)(\hat{x}\sin(|\ell|\phi) - \hat{y}\cos(|\ell|\phi)). \tag{A.5}$$

In a single-step-index fiber, $\psi_{|\ell|,m}(\rho)$ takes the form

$$\psi_{|\ell|,m}(\rho) \propto \begin{cases} \frac{J_{|\ell|}(U\rho/a)}{J_{|\ell|}(U)} : \rho \leq a \\ \frac{K_{|\ell|}(W\rho/a)}{K_{|\ell|}(W)} : \rho > a \end{cases} \tag{A.6}$$

where a is the core radius, U and W are modal constants for the core and cladding respectively, J is a Bessel function of the first kind, and K is a modified Bessel function of the second kind.

Including the traveling wave phase factors, the combination of exact fiber modes that is analogous to the combinations of LP modes that make CP modes is

$$M(\sigma,\mu|\ell) \equiv \frac{e^{i(\bar{\beta}z-\omega t)}}{2}\left\{e^{-i|\delta\beta'|z}\vec{\mathrm{HE}}^{e}_{|\ell|+1,m}(1+\sigma\mu) + e^{i|\delta\beta'|z}\vec{\mathrm{EH}}^{e}_{|\ell|-1,m}(1-\sigma\mu)\right.$$
$$\left. + i[e^{-i|\delta\beta'|z}\vec{\mathrm{HE}}^{o}_{|\ell|+1,m}(\mu+\sigma) + e^{i|\delta\beta'|z}\vec{\mathrm{EH}}^{o}_{|\ell|-1,m}(\mu-\sigma)]\right\} \tag{A.7}$$

where superscripts e and o refer to even and odd parity of the mode under a 1D parity flip around the x-axis. After setting $\sigma = \pm 1$ and $\mu = \pm 1$, which leaves combinations of EH modes only or HE modes only, it is easy to show by substituting Eqs. A.2-A.5 into Eq. A.7 that these combinations take the form $M(\sigma,\ell) \propto e^{i\ell\phi}\hat{e}_{\sigma}$ and are

eigenmodes of IOAM and SAM. For example,

$$M(+1, +|\ell|) = \left(\overrightarrow{\mathrm{HE}}^{e}_{|\ell|+1,m} + i\,\overrightarrow{\mathrm{HE}}^{o}_{|\ell|+1,m}\right) e^{i\left[\left(\bar{\beta}-|\delta\beta'|\right)z-\omega t\right]}$$

$$= \left(\psi_{|\ell|,m}(\rho)\left[(\cos(|\ell|\phi) + i\sin|\ell|\phi)\hat{x} + (-\sin(|\ell|\phi) + i\cos(|\ell|\phi))\hat{y}\right]\right) e^{i\left[\left(\bar{\beta}-|\delta\beta'|\right)z-\omega t\right]}$$

$$\text{(A.8)}$$

$$= \psi_{|\ell|,m}(\rho)e^{i\ell\phi}(\hat{x} + i\hat{y})e^{i\left[\left(\bar{\beta}-|\delta\beta'|\right)z-\omega t\right]}$$

$$= \psi_{|\ell|,m}(\rho)e^{i\ell\phi}\hat{e}_{+}e^{i\left[\left(\bar{\beta}-|\delta\beta'|\right)z-\omega t\right]} \qquad\qquad\text{(A.9)}$$

where line A.8 shows explicitly that a combination of two exact modes is a combination of all four LP modes with particular phase relationships to construct a (polarization corrected) CP mode on line A.9. If cylindrical symmetry is broken, modes of different parity within the same mode family *e.g.* HE^o and HE^e, have different propagation constants, and OAM combinations of modes are unstable [71].

A.1 Spin-Controlled Orbital Rotation

Unnormalized combinations of exact modes with the same SAM but opposite IOAM are:

$$M(\sigma, +|\ell|) + M(\sigma, -|\ell|)$$

$$= \frac{e^{i(\bar{\beta}z-\omega t)}}{2}\Bigg\{ e^{-i|\delta\beta'|z}\overrightarrow{\mathrm{HE}}^{e}_{|\ell|+1,m}(1+\sigma) + e^{i|\delta\beta'|z}\overrightarrow{\mathrm{EH}}^{e}_{|\ell|-1,m}(1-\sigma)$$

$$+ i\Big[e^{-i|\delta\beta'|z}\overrightarrow{\mathrm{HE}}^{o}_{|\ell|+1,m}(1+\sigma) + e^{i|\delta\beta'|z}\overrightarrow{\mathrm{EH}}^{o}_{|\ell|-1,m}(1-\sigma)\Big]$$

$$+ e^{-i|\delta\beta'|z}\overrightarrow{\mathrm{HE}}^{e}_{|\ell|+1,m}(1-\sigma) + e^{i|\delta\beta'|z}\overrightarrow{\mathrm{EH}}^{e}_{|\ell|-1,m}(1+\sigma)$$

$$+ i\Big[e^{-i|\delta\beta'|z}\overrightarrow{\mathrm{HE}}^{o}_{|\ell|+1,m}(-1+\sigma) + e^{i|\delta\beta'|z}\overrightarrow{\mathrm{EH}}^{o}_{|\ell|-1,m}(-1-\sigma)\Big]\Bigg\}. \qquad\text{(A.10)}$$

Factoring HE and EH modes separately,

$$e^{-i|\delta\beta'|z}\vec{\mathrm{HE}}_{|\ell|+1,m}^{\,e}(1+\sigma) + e^{-i|\delta\beta'|z}\vec{\mathrm{HE}}_{|\ell|+1,m}^{\,e}(1-\sigma)$$

$$= 2\,\vec{\mathrm{HE}}_{|\ell|+1,m}^{\,e}e^{-i|\delta\beta'|z} \tag{A.11}$$

$$e^{i|\delta\beta'|z}\vec{\mathrm{EH}}_{|\ell|-1,m}^{\,e}(1-\sigma) + e^{i|\delta\beta'|z}\vec{\mathrm{EH}}_{|\ell|-1,m}^{\,e}(1+\sigma)$$

$$= 2\,\mathrm{EH}_{|\ell|-1,m}^{e}e^{i|\delta\beta'|z} \tag{A.12}$$

$$ie^{-i|\delta\beta'|z}\vec{\mathrm{HE}}_{|\ell|+1,m}^{\,o}(1+\sigma) + ie^{-i|\delta\beta'|z}\vec{\mathrm{HE}}_{|\ell|+1,m}^{\,o}(-1+\sigma)$$

$$= 2\,i\,\sigma\,\vec{\mathrm{HE}}_{|\ell|+1,m}^{\,o}e^{-i|\delta\beta'|z} \tag{A.13}$$

$$ie^{i|\delta\beta'|z}\vec{\mathrm{EH}}_{|\ell|-1,m}^{\,o}(1-\sigma) + ie^{i|\delta\beta'|z}\vec{\mathrm{EH}}_{|\ell|-1,m}^{\,o}(-1-\sigma)$$

$$= -\,2\,i\,\sigma\vec{\mathrm{EH}}_{|\ell|-1,m}^{\,o}e^{i|\delta\beta'|z}. \tag{A.14}$$

Thus, Eq. A.10 becomes

$$M(\sigma,+|\ell|) + M(\sigma,-|\ell|)$$
$$= \left(\vec{\mathrm{HE}}_{|\ell|+1,m}^{\,e} + i\,\sigma\vec{\mathrm{HE}}_{|\ell|+1,m}^{\,o}\right)e^{-i\,|\delta\beta'|z} + \left(\vec{\mathrm{EH}}_{|\ell|-1,m}^{\,e} - i\,\sigma\vec{\mathrm{EH}}_{|\ell|-1,m}^{\,o}\right)e^{i\,|\delta\beta'|z}. \tag{A.15}$$

Substituting the low contrast expressions for the exact modes A.2-A.5 into A.15 yields

$$
\psi_{|\ell|,m}(\rho)\left[e^{-i|\delta\beta'|z}\Big((\hat{x}\cos(|\ell|\phi)-\hat{y}\sin(|\ell|\phi))+i\,\sigma(\hat{x}\sin(|\ell|\phi)+\hat{y}\cos(|\ell|\phi))\Big)\right.
$$
$$
\left.+e^{i|\delta\beta'|z}\Big((\hat{x}\cos(|\ell|\phi)+\hat{y}\sin(|\ell|\phi))-i\,\sigma(\hat{x}\sin(|\ell|\phi)-\hat{y}\cos(|\ell|\phi))\Big)\right]
$$
$$
=\psi_{|\ell|,m}(\rho)\left[e^{-i|\delta\beta'|z}\Big(\cos(|\ell|\phi)(\hat{x}+i\sigma\hat{y})+\sin(|\ell|\phi)(i\sigma\hat{x}-\hat{y})\Big)\right.
$$
$$
\left.+e^{i|\delta\beta'|z}\Big(\cos(|\ell|\phi)(\hat{x}+i\sigma\hat{y})-\sin(|\ell|\phi)(i\sigma\hat{x}-\hat{y})\Big)\right] \tag{A.16}
$$

Using $\hat{e}_\sigma \equiv \hat{x}+i\sigma\hat{y}$ and $(i\sigma\hat{x}-\hat{y})=i\sigma(\hat{x}+i\sigma\hat{y})$, Eq. A.16 becomes

$$
\psi_{|\ell|,m}(\rho)\,\hat{e}_\sigma\left[e^{-i|\delta\beta'|z}\big(\cos(|\ell|\phi)+i\sigma\sin(|\ell|\phi)\big)+e^{i|\delta\beta'|z}\big(\cos(|\ell|\phi)-i\sigma\sin(|\ell|\phi)\big)\right]
$$
$$
=\psi_{|\ell|,m}(\rho)\,\hat{e}_\sigma\left[e^{-i(|\delta\beta'|z-\sigma|\ell|\phi)}+e^{i(|\delta\beta'|z-\sigma|\ell|\phi)}\right]
$$
$$
=2\psi_{|\ell|,m}(\rho)\,\hat{e}_\sigma\cos(|\ell|\phi-\sigma|\delta\beta'|z). \tag{A.17}
$$

The direction of the rotation is controlled by σ and $\delta\beta$ controls the rotation rate. Letting $\xi \equiv |\ell|\phi-\sigma|\delta\beta'|z$ be the phase of this rotating profile, a surface of constant phase is identified by setting $\xi = K$, where K is an arbitrary constant so

$$
K = |\ell|\phi_{ep}-\sigma|\delta\beta'|z \tag{A.18}
$$
$$
\therefore \phi_{ep} = \sigma\frac{|\delta\beta'|z}{|\ell|}, \tag{A.19}
$$

where ϕ_{ep} is the azimuthal coordinate of the surface equal phase. The rotation rate R_s of the mode is

$$
R_s \equiv \frac{d\phi_{ep}}{dz} = \sigma\frac{|\delta\beta'|}{|\ell|}. \tag{A.20}
$$

This agrees with the results of the perturbative approach in Eq. 2.44.

A.2 Orbit-Controlled Spin Rotation

Orbit-controlled spin rotation consists of combinations of common OAM, but opposite circular polarizations combining to make linear polarization,

$$M(+1,\mu|\ell|) + M(-1,\mu|\ell|)$$

$$= \frac{1}{2}\Big[e^{-i|\delta\beta'|z}\overrightarrow{\mathrm{HE}}^{e}_{|\ell|+1,m}(1+\mu) + e^{i|\delta\beta'|z}\overrightarrow{\mathrm{EH}}^{e}_{|\ell|-1,m}(1-\mu)$$

$$+i[e^{-i|\delta\beta'|z}\overrightarrow{\mathrm{HE}}^{o}_{|\ell|+1,m}(\mu+1) + e^{i|\delta\beta'|z}\overrightarrow{\mathrm{EH}}^{o}_{|\ell|-1,m}(\mu-1)]$$

$$+e^{-i|\delta\beta'|z}\overrightarrow{\mathrm{HE}}^{e}_{|\ell|+1,m}(1-\mu) + e^{i|\delta\beta'|z}\overrightarrow{\mathrm{EH}}^{e}_{|\ell|-1,m}(1+\mu)$$

$$+i[e^{-i|\delta\beta'|z}\overrightarrow{\mathrm{HE}}^{o}_{|\ell|+1,m}(\mu-1) + e^{i|\delta\beta'|z}\overrightarrow{\mathrm{EH}}^{o}_{|\ell|-1,m}(\mu+1)]\Big\}. \qquad (\mathrm{A}.21)$$

Factoring EH and HE modes separately,

$$e^{-i|\delta\beta'|z}\overrightarrow{\mathrm{HE}}^{e}_{|\ell|+1,m}(1+\mu) + e^{-i|\delta\beta'|z}\overrightarrow{\mathrm{HE}}^{e}_{|\ell|+1,m}(1-\mu)$$

$$= 2\,\overrightarrow{\mathrm{HE}}^{e}_{|\ell|+1,m}e^{-i|\delta\beta'|z} \qquad (\mathrm{A}.22)$$

$$e^{i|\delta\beta'|z}\overrightarrow{\mathrm{EH}}^{e}_{|\ell|-1,m}(1-\mu) + e^{i|\delta\beta'|z}\overrightarrow{\mathrm{EH}}^{e}_{|\ell|-1,m}(1+\mu)$$

$$= 2\,\mathrm{EH}^{e}_{|\ell|-1,m}e^{i|\delta\beta'|z} \qquad (\mathrm{A}.23)$$

$$ie^{-i|\delta\beta'|z}\overrightarrow{\mathrm{HE}}^{o}_{|\ell|+1,m}(\mu+1) + ie^{-i|\delta\beta'|z}\overrightarrow{\mathrm{HE}}^{o}_{|\ell|+1,m}(\mu-1)$$

$$= 2\,i\,\mu\,\overrightarrow{\mathrm{HE}}^{o}_{|\ell|+1,m}e^{-i|\delta\beta'|z} \qquad (\mathrm{A}.24)$$

$$ie^{i|\delta\beta'|z}\overrightarrow{\mathrm{EH}}^{o}_{|\ell|-1,m}(\mu-1) + ie^{i|\delta\beta'|z}\overrightarrow{\mathrm{EH}}^{o}_{|\ell|-1,m}(\mu+1)$$

$$= 2\,i\,\mu\overrightarrow{\mathrm{EH}}^{o}_{|\ell|-1,m}e^{i|\delta\beta'|z}. \qquad (\mathrm{A}.25)$$

Thus, Eq. A.21 becomes

$$M(+1, \mu|\ell|) + M(-1, \mu|\ell|)$$
$$= \left(\vec{\text{HE}}^{\,e}_{|\ell|+1,m} + i\,\mu \vec{\text{HE}}^{\,o}_{|\ell|+1,m} \right) e^{-i\,|\delta\beta'|z} + \left(\vec{\text{EH}}^{\,e}_{|\ell|-1,m} + i\,\mu \vec{\text{EH}}^{\,o}_{|\ell|-1,m} \right) e^{i\,|\delta\beta'|z}. \quad \text{(A.26)}$$

Substituting the low contrast expressions for the exact modes A.2-A.5 into A.26 yields

$$M(+1, \mu|\ell|) + M(-1, \mu|\ell|)$$
$$= \psi_{|\ell|,m}(\rho) \Big\{ \Big[\big(\hat{x} \cos(|\ell|\phi) - \hat{y} \sin(|\ell|\phi) \big) + i\mu \big(\hat{x} \sin(|\ell|\phi) + \hat{y} \cos(|\ell|\phi) \big) \Big] e^{-i\,|\delta\beta'|z}$$
$$+ \Big[\big(\hat{x} \cos(|\ell|\phi) + \hat{y} \sin(|\ell|\phi) \big) + i\mu \big(\hat{x} \sin(|\ell|\phi) - \hat{y} \cos(|\ell|\phi) \big) \Big] e^{i\,|\delta\beta'|z} \Big\}. \quad \text{(A.27)}$$

Noting that $\cos(|\ell|\phi) = \cos(\mu|\ell|\phi)$ because cos is even, and grouping $\cos(|\ell|\phi) + i\mu \sin(|\ell|\phi) = e^{i\ell\phi}$ gives an overall IOAM phase factor common to all terms

$$M(+1, \mu|\ell|) + M(-1, \mu|\ell|)$$
$$= \psi_{|\ell|,m}(\rho) e^{i\ell\phi} \Big[(\hat{x} + i\mu\hat{y}) e^{-i\,|\delta\beta'|z} + (\hat{x} - i\mu\hat{y}) e^{i\,|\delta\beta'|z} \Big]$$
$$= 2\psi_{|\ell|,m}(\rho) e^{i\ell\phi} \Big[\cos(|\delta\beta'|z)\hat{x} + \mu\sin(|\delta\beta'|z)\hat{y} \Big] \quad \text{(A.28)}$$

which is linear polarization with orientation on the Poincaré sphere (which we'll call $\tilde{\phi}$ here to avoid confusion with the azimuthal coordinate in configuration space)

$$\tilde{\phi} = \mu|\delta\beta'|z \quad \text{(A.29)}$$

and rotation rate R_p

$$R_p \equiv \frac{\mathrm{d}\tilde{\phi}}{\mathrm{d}z} = \mu|\delta\beta'|. \quad \text{(A.30)}$$

144

This agrees with the results of the perturbative approach in Eq. 2.46.

REFERENCES CITED

[1] A. M. Fedotov, N. B. Narozhny, G. Mourou, and G. Korn, "Limitations on the attainable intensity of high power lasers," Phys. Rev. Lett. **105**, 1–4 (2010), arXiv:1004.5398 .

[2] Michael A Nielsen and Isaac L Chuang, *Quantum Computation and Quantum Information* (Cambridge University Press, Cambridge, 2000).

[3] Scott Aaronson and Alex Arkhipov, "The computational complexity of linear optics," in *Proceedings of the Forty-third Annual ACM Symposium on Theory of Computing*, STOC '11 (ACM, New York, NY, USA, 2011) pp. 333–342.

[4] Robert W. Boyd, *Nonlinear Optics*, 1st ed. (Academic Press, San Diego, CA, 1992).

[5] Bahaa E A Saleh and Malvin Carl Teich, *Fundamentals of Photonics*, 2nd ed. (Wiley-Interscience, Hoboken, NJ, 2007).

[6] David J. Griffiths, *Introduction to Quantum Mechanics* (Pearson, Upper Saddle River, NJ, 2005).

[7] Alison M. Yao and Miles J. Padgett, "Orbital angular momentum: origins, behavior and applications," Adv. Opt. Photon. **3**, 161–204 (2011).

[8] Richard A. Beth, "Mechanical detection and measurement of the angular momentum of light," Phys. Rev. **50**, 115–125 (1936).

[9] L. Allen, M. W. Beijersbergen, R. J. C. Spreeuw, and J. P. Woerdman, "Orbital angular momentum of light and the transformation of laguerre-gaussian laser modes," Phys. Rev. A **45**, 8185–8189 (1992).

[10] L Allen, "Introduction to the atoms and angular momentum of light special issue," Journal of Optics B: Quantum and Semiclassical Optics **4**, S1 (2002).

[11] A. T. O'Neil, I. MacVicar, L. Allen, and M. J. Padgett, "Intrinsic and extrinsic nature of the orbital angular momentum of a light beam," Phys. Rev. Lett. **88**, 053601 (2002).

[12] Konstantin Yu. Bliokh, "Geometrical optics of beams with vortices: Berry phase and orbital angular momentum hall effect," Phys. Rev. Lett. **97**, 043901 (2006).

[13] N. S. Kapany and J. J. Burke, *Optical Waveguides*, edited by Yoh-Han Pao (Academic Press, New York, 1972).

[14] C. C. Leary, M. G. Raymer, and S. J. van Enk, "Spin and orbital rotation of electrons and photons via spin-orbit interaction," Phys. Rev. A **80**, 061804 (2009).

[15] Akira Tomita and Raymond Y. Chiao, "Observation of berry's topological phase by use of an optical fiber," Phys. Rev. Lett. **57**, 937–940 (1986).

[16] A. V. Dooghin, N. D. Kundikova, V. S. Liberman, and B. Ya. Zel'dovich, "Optical magnus effect," Phys. Rev. A **45**, 8204–8208 (1992).

[17] Harsh Mathur, "Thomas precession, spin-orbit interaction, and berry's phase," Phys. Rev. Lett. **67**, 3325–3327 (1991).

[18] Alain Bérard and Hervé Mohrbach, "Spin hall effect and berry phase of spinning particles," Physics Letters A **352**, 190–195 (2006).

[19] K. Yu. Bliokh and Yu. P. Bliokh, "Modified geometrical optics of a smoothly inhomogeneous isotropic medium: The anisotropy, berry phase, and the optical magnus effect," Phys. Rev. E **70**, 026605 (2004).

[20] K.Y. Y Bliokh, F.J. Rodríguez-Fortuño, F. Nori, and A.V. V Zayats, "Spin-orbit interactions of light," Nat. Photonics **9**, 1505.02864 (2015), arXiv:1505.02864 .

[21] Onur Hosten and Paul Kwiat, "Observation of the spin hall effect of light via weak measurements," Science **319**, 787–790 (2008), http://science.sciencemag.org/content/319/5864/787.full.pdf .

[22] Konstantin Y Bliokh, Avi Niv, Vladimir Kleiner, and Erez Hasman, "Geometrodynamics of spinning light," Nat Phot. **2**, 748–753 (2008).

[23] V. S. Liberman and B. Ya. Zel'dovich, "Spin-orbit interaction of a photon in an inhomogeneous medium," Phys. Rev. A **46**, 5199–5207 (1992).

[24] Sarkew Abdulkareem and Nataliya Kundikova, "Joint effect of polarization and the propagation path of a light beam on its intrinsic structure," Opt. Express **24**, 19157–19166 (2016).

[25] V. V. Butkovskaya, A. V. Volyar, and T. A. Fadeeva, "Vortex optical magnus effect in multimode fibers," Technical Physics Letters **23**, 649–650 (1997).

[26] L. Wang, P. Vaity, B. Ung, Y. Messaddeq, L. A. Rusch, and S. LaRochelle, "Characterization of oam fibers using fiber bragg gratings," Opt. Express **22**, 15653–15661 (2014).

[27] Paul G. Kwiat, Klaus Mattle, Harald Weinfurter, Anton Zeilinger, Alexander V. Sergienko, and Yanhua Shih, "New high-intensity source of polarization-entangled photon pairs," Phys. Rev. Lett. **75**, 4337–4341 (1995).

[28] H. J. McGuinness, M. G. Raymer, C. J. McKinstrie, and S. Radic, "Quantum frequency translation of single-photon states in a photonic crystal fiber," Phys. Rev. Lett. **105**, 093604 (2010).

[29] M. Fiorentino, P. L. Voss, J. E. Sharping, and P. Kumar, "All-fiber photon-pair source for quantum communications," IEEE Photonics Technology Letters **14**, 983–985 (2002).

[30] Brian J. Smith, P. Mahou, Offir Cohen, J. S. Lundeen, and I. A. Walmsley, "Photon pair generation in birefringent optical fibers," Opt. Express **17**, 23589–23602 (2009).

[31] Cody Collin Leary, *Measurement and Control of Transverse Photonic Degrees of Freedom via Parity Sorting and Spin-Orbit Interaction*, Ph.D. thesis, University of Oregon (2010).

[32] C. C. Leary and Karl H. Smith, "Unified dynamics of electrons and photons via *Zitterbewegung* and spin-orbit interaction," Phys. Rev. A **89**, 023831 (2014).

[33] Frank L Pedrotti and Leno S Pedrotti, *Introduction to Optics*, 2nd ed. (Prentice Hall, Englewood Cliffs, NJ, 1993).

[34] John David Jackson, *Classical Electrodynamics*, 3rd ed. (Wiley, New York, NY, 1999).

[35] A. E. Siegman, *Lasers* (University Science Books, Sausalito, CA, 1986).

[36] M.W. Beijersbergen, L. Allen, H.E.L.O. van der Veen, and J.P. Woerdman, "Astigmatic laser mode converters and transfer of orbital angular momentum," Optics Communications **96**, 123 – 132 (1993).

[37] Michael V. Berry, "Paraxial beams of spinning light," in *Proc. SPIE*, Vol. 3487 (1998) pp. 6–11.

[38] D. Gloge, "Propagation effects in optical fibers," IEEE Transactions on Microwave Theory and Techniques **23**, 106–120 (1975).

[39] E. Snitzer, "Cylindrical dielectric waveguide modes," J. Opt. Soc. Am. **51**, 491–498 (1961).

[40] E. Snitzer and H. Osterberg, "Observed dielectric waveguide modes in the visible spectrum," J. Opt. Soc. Am. **51**, 499–505 (1961).

[41] Allan W. Snyder and John D. Love, *Optical Waveguide Theory* (Chapman and Hall, New York, 1983).

[42] S. Berdagué and P. Facq, "Mode division multiplexing in optical fibers," Appl. Opt. **21**, 1950–1955 (1982).

[43] Hao Huang, Giovanni Milione, Martin P J Lavery, Guodong Xie, Yongxiong Ren, Yinwen Cao, Nisar Ahmed, Thien An Nguyen, Daniel A Nolan, Ming-Jun Li, Moshe Tur, Robert R Alfano, and Alan E Willner, "Mode division multiplexing using an orbital angular momentum mode sorter and MIMO-DSP over a graded-index few-mode optical fibre," Sci. Rep. **5**, 14931 (2015).

[44] Yan Yan, Yang Yue, Hao Huang, Jeng-Yuan Yang, Mohammad R. Chitgarha, Nisar Ahmed, Moshe Tur, Samuel. J. Dolinar, and Alan E. Willner, "Efficient generation and multiplexing of optical orbital angular momentum modes in a ring fiber by using multiple coherent inputs," Opt. Lett. **37**, 3645–3647 (2012).

[45] Lian-Wee Luo, Noam Ophir, Christine P Chen, Lucas H Gabrielli, Carl B Poitras, Keren Bergmen, and Michal Lipson, "WDM-compatible mode-division multiplexing on a silicon chip," Nat. Commun. **5** (2014).

[46] Nenad Bozinovic, Yang Yue, Yongxiong Ren, Moshe Tur, Poul Kristensen, Hao Huang, Alan E. Willner, and Siddharth Ramachandran, "Terabit-scale orbital angular momentum mode division multiplexing in fibers," Science **340**, 1545–1548 (2013).

[47] P. Gregg, P. Kristensen, and S. Ramachandran, "Conservation of orbital angular momentum in air-core optical fibers," Optica **2**, 267–270 (2015).

[48] Jaques Bures, *Guided Optics* (Wiley-VCH, Weinheim, 2009).

[49] Giovanni Milione, Ezra Ip, Ming-Jun Li, Jefferey Stone, Gaozhu Peng, and Ting Wang, "Mode crosstalk matrix measurement of a 1 km elliptical core few-mode optical fiber," Opt. Lett. **41**, 2755–2758 (2016).

[50] A. Bjarklev, "Microdeformation losses of single-mode fibers with step-index profiles," Journal of Lightwave Technology **4**, 341–346 (1986).

[51] John R. Taylor, *An Introduction to Error Analysis*, 2nd ed. (University Science Books, Sausalito, CA, 1982).

[52] Graham Gibson, Johannes Courtial, Miles J. Padgett, Mikhail Vasnetsov, Valeriy Pas'ko, Stephen M. Barnett, and Sonja Franke-Arnold, "Free-space information transfer using light beams carrying orbital angular momentum," Opt. Express **12**, 5448–5456 (2004).

[53] Max Born and Emil Wolf, *Principles of Optics: Electromagnetic Theory of Propagation, Interference and Diffraction of Light*, 6th ed. (Cambridge University Press, 1980).

[54] Amber M. Beckley, Thomas G. Brown, and Miguel A. Alonso, "Full poincaré beams," Opt. Express **18**, 10777–10785 (2010).

149

[55] Amber M. Beckley, Thomas G. Brown, and Miguel A. Alonso, "Full Poincaré beams II: partial polarization," Opt. Express **20**, 9357–9362 (2012).

[56] C.C. Leary, L.A. Baumgardner, and M.G. Raymer, "Stable mode sorting by two-dimensional parity of photonic transverse spatial states," Opt. Express **17**, 2435–2452 (2009).

[57] S. Ramachandran, "Dispersion-tailored few-mode fibers: a versatile platform for in-fiber photonic devices," Journal of Lightwave Technology **23**, 3426–3443 (2005).

[58] Dashiell L. Vitullo, M. G. Raymer, Cody C. Leary, and Siddharth Ramachandran, "Photonic spin-orbit interaction in few-mode optical fiber," in *Frontiers in Optics 2011/Laser Science XXVII* (Optical Society of America, 2011) p. LWI4.

[59] A. K. Ghatak and K. Thyagarajan, *An Introduction to Fiber Optics* (Cambridge University Press, Cambridge, 1998).

[60] Yoonshik Kang, Kiyoung Cho, Jaewoo Noh, Dashiell L. P. Vitullo, Cody Leary, and M. G. Raymer, "Remote preparation of complex spatial states of single photons and verification by two-photon coincidence experiment," Opt. Express **18**, 1217–1233 (2010).

[61] Roger A. Smith, Dileep V. Reddy, Dashiell L.P. Vitullo, and M. G. Raymer, "Double-heralded generation of two-photon-states by spontaneous four-wave-mixing in the presence of noise," Opt. Express **24**, 5809–5821 (2016).

[62] Jun Chen, Xiaoying Li, and Prem Kumar, "Two-photon-state generation via four-wave mixing in optical fibers," Phys. Rev. A **72**, 033801 (2005).

[63] L. Mejling, D. S. Cargill, C. J. McKinstrie, K. Rottwitt, and R. O. Moore, "Effects of nonlinear phase modulation on bragg scattering in the low-conversion regime," Opt. Express **20**, 27454–27475 (2012).

[64] L. Mejling, C. J. McKinstrie, M. G. Raymer, and K. Rottwitt, "Quantum frequency translation by four-wave mixing in a fiber: low-conversion regime," Opt. Express **20**, 8367–8396 (2012).

[65] Jesper B. Christensen, C. J. McKinstrie, and K. Rottwitt, "Temporally uncorrelated photon-pair generation by dual-pump four-wave mixing," Phys. Rev. A **94**, 013819 (2016).

[66] Govind P Agrawal, *Nonlinear Fiber Optics*, 3rd ed. (Academic press, 2001).

[67] Liang Cui, Xiaoying Li, and Ningbo Zhao, "Spectral properties of photon pairs generated by spontaneous four-wave mixing in inhomogeneous photonic crystal fibers," Phys. Rev. A **85**, 023825 (2012).

[68] Barbara M. Terhal and Paweł Horodecki, "Schmidt number for density matrices," Phys. Rev. A **61**, 040301 (2000).

[69] D. V. Reddy, M. G. Raymer, C. J. McKinstrie, L. Mejling, and K. Rottwitt, "Temporal mode selectivity by frequency conversion in second-order nonlinear optical waveguides," Opt. Express **21**, 13840–13863 (2013).

[70] Nicolas Sangouard, Christoph Simon, Hugues de Riedmatten, and Nicolas Gisin, "Quantum repeaters based on atomic ensembles and linear optics," Rev. Mod. Phys. **83**, 33–80 (2011).

[71] C.N. Alexeyev, M. S. Soskin, and A. V. Volyar, "Spin-orbit interaction in a generic vortex field transmitted through an elliptic fiber," Semicond. Physics, Quantum Electron. Optoelectron. **3**, 501–513 (2000).